

# Fibre-optic nonlinear optical microscopy and endoscopy

*A thesis submitted for the degree of  
Doctor of Philosophy*

by

**Ling Fu**



*Centre for Micro-Photonics  
Faculty of Engineering and Industrial Sciences  
Swinburne University of Technology  
Melbourne, Australia*

*For my beloved family.*

*“All theory is gray, but the golden tree of life springs ever green. . . . .”*

*— Johann Wolfgang von Goethe*

*The search for truth is more precious than its possession.*

*— Albert Einstein*

# Declaration

I, Ling Fu, declare that this thesis entitled:

*“Fibre-optic nonlinear microscopy and endoscopy”*

is my own work and has not been submitted previously, in whole or in part, in respect of any other academic award.

Ling Fu

Centre for Micro-Photonics  
Faculty of Engineering and Industrial Sciences  
Swinburne University of Technology  
Australia

Dated this day, April 27, 2007

# Abstract

Cancer is a major health problem in the world today. Almost all cancers have a significantly better chance for therapy and recovery if detected at their early stage. The capability to perform disease diagnosis at an early stage requires high-resolution imaging that can visualise the physiological and morphological changes at a cellular level. However, resolving powers of current medical imaging systems are limited to sub-millimeter sizes. Furthermore, the majority of cancers are associated with morphological and functional alterations of cells in epithelial tissue, currently assessed by invasive and time-consuming biopsy. Optical imaging enables visualisations of tissue microstructures at the level of histology in non-invasive means. Optical imaging is suitable for detecting neoplastic changes with sub-cellular resolution *in vivo* without the need for biopsy.

Nonlinear optical microscopy based on multi-photon absorption and higher harmonic generation has provided spectacular sights into visualisation of cellular events within live tissue due to advantages of an inherent sectioning ability, the relatively deep optical penetration, and the direct visualisation of intrinsic indicators. Two-photon excited fluorescence (TPEF) from intrinsic cell components and second harmonic from asymmetric supermolecular structures can provide complementary information regarding functionalities and morphologies in tissue environments, thus enabling premalignant diagnosis by detecting the very earliest changes in cellular structures.

During the past sixteen years, nonlinear optical microscopy has evolved from a photonic novelty to a well-established laboratory tool. At present, *in vivo* imaging and

long-term bedside studies by use of nonlinear optical microscopy have been limited due to the fact that the lack of the compact nonlinear optical instrument/imaging technique forces the performance of nonlinear optical microscopy with bulk optics on the bench top. Rapid developments of fibre-optics components in terms of growing functionalities and decreasing sizes provide enormous opportunities for innovation in nonlinear optical microscopy. Fibre-based nonlinear optical endoscopy will be the soul instrumentation to permit the cellular imaging within hollow tissue tracts or solid organs that are inaccessible with a conventional optical microscope.

Lots of efforts have been made for development of miniaturised nonlinear optical microscopy. However, there are major challenges remaining to create a nonlinear optical endoscope applicable within internal cavities of a body. First, an excitation laser beam with an ultrashort pulse width should be delivered efficiently to a remote place where efficient collection of faint nonlinear optical signals from biological samples is required. Second, laser-scanning mechanisms adopted in such a miniaturised instrumentation should permit size reduction to a millimeter scale and enable fast scanning rates for monitoring biological processes. Finally, the design of a nonlinear optical endoscope based on micro-optics must maintain great flexibility and compact size to be incorporated into endoscopes to image internal organs.

Although there are obvious difficulties, development of fibre-optic nonlinear optical microscopy/endoscopy would be indispensable to innovate conventional nonlinear optical microscopy, and therefore make a significant impact on medical diagnosis. The work conducted in this thesis demonstrates the new capability of nonlinear optical endoscopy based on a single-mode fibre (SMF) coupler or a double-clad photonic crystal fibre (PCF), a microelectromechanical system (MEMS) mirror, and a gradient-index (GRIN) lens. The feasibility of all-fibre nonlinear optical endoscopy is also demonstrated by the further integration of a double-clad PCF coupler. The thesis concentrates on the following key areas in order to exploit and understand the new imaging modality.

It has been known from the previous studies that an SMF coupler is suitable for two-

photon excitation by transmitting near infrared illumination and collecting fluorescence at visible wavelength as well. Although second harmonic generation (SHG) wavelength is farther away from the designed wavelength of the fibre coupler than that of normal TPEF, it is demonstrated in this thesis that both SHG and TPEF signals can be collected simultaneously and efficiently through an SMF coupler with axial resolution of  $1.8 \mu m$  and  $2.1 \mu m$ , respectively. The fibre coupler shows a unique feature of linear polarisation preservation along the birefringent axis over the near infrared and the visible wavelength regions. Therefore, SHG polarisation anisotropy can be potentially extracted for probing the orientation of structural proteins in tissue. Furthermore, this thesis shows the characterisation of nonlinear optical microscopy based on the separation distance of an SMF coupler and a GRIN lens. Consequently, the collection of nonlinear signals has been optimised after the investigation of the intrinsic trade-off between signal level and axial resolution.

These phenomena have been theoretically explored in this thesis through formalisation and numerical analysis of the three-dimensional (3D) coherent transfer function for a SHG microscope based on an SMF coupler. It has been discovered that a fibre-optic SHG microscope exhibits the same spatial frequency passband as that of a fibre-optic reflection-mode non-fluorescence microscope. When the numerical aperture of the fibre is much larger than the convergent angle of the illumination on the fibre aperture, the performance of fibre-optic SHG microscopy behaves as confocal SHG microscopy. Furthermore, it has been shown in both analysis and experiments that axial resolution in fibre-optic SHG microscopy is dependent on the normalised fibre spot size parameters. For a given illumination wavelength, axial resolution has an improvement of approximately 7% compared with TPEF microscopy using an SMF coupler.

Although an SMF enables the delivery of a high quality laser beam and an enhanced sectioning capability, the low numerical aperture and the finite core size of an SMF give rise to a restricted sensitivity of a nonlinear optical microscope system. The key innovation demonstrated in this thesis is a significant signal enhancement of a

nonlinear optical endoscope by use of a double-clad PCF. This thesis has characterised properties of our custom-designed double-clad PCF in order to construct a 3D nonlinear optical microscope. It has been shown that both the TPEF and SHG signal levels in a PCF-based system that has an optical sectioning property for 3D imaging can be significantly improved by two orders of magnitude in comparison with those in an SMF-based microscope. Furthermore, in contrast with the system using an SMF, simultaneous optimisations of axial resolution and signal level can be obtained by use of double-clad PCFs. More importantly, using a MEMS mirror as the scanning unit and a GRIN lens to produce a fast scanning focal spot, the concept of nonlinear optical endoscopy based on a double-clad PCF, a MEMS mirror and a GRIN lens has been experimentally demonstrated. The ability of the nonlinear optical endoscope to perform high-resolution 3D imaging in deep tissue has also been shown.

A novel three-port double-clad PCF coupler has been developed in this thesis to achieve self-alignment and further replace bulk optics for an all-fibre endoscopic system. The double-clad PCF coupler exhibits the property of splitting the laser power as well as the separation of a near infrared single-mode beam from a visible multimode beam, showing advantages for compact nonlinear optical microscopy that cannot be achieved from an SMF coupler. A compact nonlinear optical microscope based on the double-clad PCF coupler has been constructed in conjunction with a GRIN lens, demonstrating high-resolution 3D TPEF and SHG images with the axial resolution of approximately  $10\ \mu\text{m}$ . Such a PCF coupler can be useful not only for a fibre-optic nonlinear optical probe but also for double-clad fibre lasers and amplifiers.

The work presented in this thesis has led to the possibility of a new imaging device to complement current non-invasive imaging techniques and optical biopsy for cancer detection if an ultrashort-pulsed fibre laser is integrated and the commercialisation of the system is achieved. This technology will enable *in vivo* visualisations of functional and morphological changes of tissue at the microscopic level rather than direct observations with a traditional instrument at the macroscopic level. One can anticipate the progress in fibre-optic nonlinear optical imaging that will propel imaging



applications that require both miniaturisation and great functionality.

# Acknowledgements

In April 2002, when I was going to finish my Master project, Prof. Min Gu gave me this remarkable opportunity to undertake a PhD research degree with him. Prof. Min Gu has supported the PhD project from the day I decided that this was what I wanted to do. So first and foremost, I would like to thank him here, and express my sincerest gratitude for him. His tireless help, advices and guidance make the completion of my research work possible. From a student's point of view, he could win the best supervisor award if there is one in the world. His impressive characters and vision for science are something to draw inspiration from in my future work.

My sincerest gratitude goes to my cosupervisor Dr. Xiaosong Gan who passed on valuable experience that he had to do research, the useful discussion, and experimental suggestions. I would like to thank Dr. Damian Bird for his remarkable research foundation on this topic. In particular, I would like to thank Dr. Charles Cranfield, Prof. Sarah Russell, and Dr. Linda Chen for their thought and generous help on handling various biological samples. To the external people involved in this project, Prof. Huikai Xie, Dr. Ankur Jain and Mr. Lei Wu in University of Florida, thank all for their excellent collaboration work in the application of MEMS mirrors. Their relentless help and discussion for the project are greatly appreciated. I also would like to thank Mr. Yang in Fovice and Prof. Lee (Gwangju Institute of Science and Technology, Korea) for their help on the photonic crystal fibre coupler fabrication.

I am very grateful for Swinburne University of Technology and the Centre for Micro-Photonics (CMP) for their financial support throughout the PhD candidature, which made the work so much easier. To the CMP administrative assistants Mrs. Anna Buzescu, Mrs. Benita Hutchinson-Reade, and Ms. Katie Cage, thank all for their help with paperwork and general office tasks. Many thanks go to Mr. Mark Kivinen for

making custom optical mounts for my experimental setup.

My particular thanks go to Dr. Baohua Jia for her various help since my first day came to Australia. Thank you Dr. Dru Morrish for helping me with the laboratory equipment and convincing me to use  $\text{\LaTeX} 2_{\epsilon}$  for my thesis. Dr. Daniel Day, I thank him for his constructive advices on the daily laboratory life and the help with my Labview program. I thank Dr. James Chon very much for his help on the delivery of the fibre coupler. I would also like to thank Mr. Michael Vanner for the assistance of the programming to drive the MEMS mirror. To Mrs. Smitha Kuriakose and Ms. Jing Wu, I acknowledge many light-hearted moment with them.

To the other members of the CMP, Dr. Zeev Bomzon, Dr. Guangyong Zhou, Dr. Shuhui Wu, Dr. Craig Bullen, Dr. Djenan Ganic, Dr. Kyongsik Choi, Mr. Michael Ventura, Mr. Jiafang Li, Mr. Xiangping Li, Mr. Peter Zijlstra, Mr. Brendan Chick, Ms. Olga Papageorgiou, thank them for their help and discussion during the meetings and day to day business.

Finally, I would like to acknowledge my family to whom this thesis is dedicated. I am forever indebted to my parents. Without their support the preservation of my physical and mental health in completion of this thesis would not have been possible. To my husband, Qian, thank him deeply for his great patience and understanding. Although the time this PhD took away from us can never be regained, I am sure it will be great benefit to our whole life.

Ling Fu

Melbourne, Australia

April 27, 2007

# Contents

**Declaration**

**Abstract** **i**

**Acknowledgements** **vi**

**Contents** **viii**

**List of Figures** **xiii**

**List of Tables** **xxiv**

**1 Introduction** **1**

1.1 Introduction to nonlinear optical endoscopy . . . . . 2

1.1.1 Nonlinear optical microscopy . . . . . 2

1.1.2 Challenges in nonlinear optical endoscopy . . . . . 5

1.2 Thesis objectives . . . . . 7

1.3 Preview of the thesis . . . . . 9

**2 Review of fibre-optic nonlinear optical microscopy** **12**

2.1 Introduction . . . . . 12

2.2 Nonlinear optical microscopy . . . . . 13

2.2.1 Multi-photon fluorescence microscopy . . . . . 14

2.2.2 Harmonic generation microscopy . . . . . 17

2.2.3 Coherent anti-Stokes Raman scattering microscopy . . . . . 19

2.3	Fibre-optic nonlinear microscopy using single-mode fibres . . . . .	20
2.3.1	Single-mode fibres and ultrashort pulse delivery . . . . .	21
2.3.2	Scanning mechanisms . . . . .	25
2.3.3	Compact objective lens . . . . .	27
2.4	PCFs in nonlinear optical microscopy . . . . .	30
2.4.1	Large-mode-area PCFs . . . . .	32
2.4.2	Hollow-core photonic bandgap fibres . . . . .	33
2.4.3	Double-clad PCFs . . . . .	35
2.4.4	Highly nonlinear PCFs . . . . .	37
2.5	Geometries of fibre-optic nonlinear optical microscopy . . . . .	39
2.6	Chapter summary . . . . .	42
<b>3</b>	<b>Nonlinear optical microscopy using a single-mode fibre coupler</b>	<b>44</b>
3.1	Introduction . . . . .	44
3.2	Polarisation characteristics of a single-mode fibre coupler . . . . .	46
3.2.1	Experimental arrangement . . . . .	46
3.2.2	Coupling efficiency and splitting ratio . . . . .	48
3.2.3	Degree of polarisation . . . . .	50
3.3	A SHG microscope based on a single-mode fibre coupler . . . . .	53
3.3.1	Experimental arrangement . . . . .	53
3.3.2	Nonlinear optical spectra . . . . .	54
3.3.3	Nonlinear optical axial response . . . . .	57
3.3.4	SHG and TPEF imaging . . . . .	60
3.3.5	SHG polarisation anisotropy . . . . .	62
3.4	Characterisation of the GRIN lens-fibre spacing . . . . .	65
3.4.1	Experimental arrangement . . . . .	66
3.4.2	Determination of the effective numerical aperture . . . . .	67
3.4.3	Optimisation of the nonlinear optical signal . . . . .	69

3.4.4	Two-photon fluorescence imaging . . . . .	72
3.5	Chapter conclusions . . . . .	73
<b>4</b>	<b>Three-dimensional image formation in fibre-optic second harmonic generation microscopy</b>	<b>75</b>
4.1	Introduction . . . . .	75
4.2	Three-dimensional image formation . . . . .	77
4.3	Three-dimensional coherent transfer function . . . . .	79
4.4	Numerical and experimental results . . . . .	83
4.4.1	Coherent transfer function . . . . .	83
4.4.2	Axial resolution . . . . .	85
4.4.3	Signal level . . . . .	88
4.5	Chapter conclusions . . . . .	90
<b>5</b>	<b>Nonlinear optical endoscopy using a double-clad photonic crystal fibre</b>	<b>91</b>
5.1	Introduction . . . . .	91
5.2	Characterisation of double-clad PCFs . . . . .	93
5.2.1	Coupling efficiency . . . . .	93
5.2.2	Degree of polarisation . . . . .	96
5.3	A nonlinear optical microscope based on double-clad PCFs . . . . .	97
5.3.1	Experimental arrangement . . . . .	97
5.3.2	Axial resolution . . . . .	98
5.3.3	Improvement of signal level . . . . .	101
5.3.4	Nonlinear optical imaging . . . . .	103
5.3.5	SHG polarisation anisotropy . . . . .	104
5.4	A nonlinear optical endoscope based on a double-clad PCF and a MEMS mirror . . . . .	105

5.4.1	Endoscope design . . . . .	105
5.4.2	Axial resolution and signal level . . . . .	107
5.4.3	Effect of a GRIN lens . . . . .	109
5.4.4	Feasibility of a MEMS mirror . . . . .	111
5.4.5	2D Endoscopic imaging . . . . .	113
5.5	3D Tissue imaging . . . . .	116
5.5.1	Imaging with rat tail tendon . . . . .	116
5.5.2	Imaging with gastrointestinal tract tissue . . . . .	117
5.5.3	Imaging with oral cavity tissue . . . . .	120
5.5.4	Imaging with cancer tissue . . . . .	122
5.6	Chapter conclusions . . . . .	125
<b>6</b>	<b>Nonlinear optical microscopy using a double-clad photonic crystal fibre coupler</b>	<b>127</b>
6.1	Introduction . . . . .	127
6.2	A double-clad PCF coupler . . . . .	129
6.2.1	Fabrication process . . . . .	129
6.2.2	Propagation property . . . . .	130
6.2.3	Splitting ratio optimisation . . . . .	132
6.3	Experimental arrangement . . . . .	134
6.4	System performance . . . . .	135
6.4.1	Axial resolution . . . . .	135
6.4.2	Nonlinear optical imaging . . . . .	136
6.5	Chapter conclusions . . . . .	137

<b>7 Conclusion</b>	<b>139</b>
7.1 Thesis conclusions . . . . .	139
7.2 Future work . . . . .	143
7.2.1 Engineering of a double-clad PCF . . . . .	144
7.2.2 <i>In vivo</i> tissue imaging . . . . .	145
<b>Bibliography</b>	<b>146</b>
<b>Publications of the Author</b>	<b>163</b>



# List of Figures

1.1	Schematic diagram of a nonlinear optical microscope. (a) Ultrashort pulses from a Ti:Sapphire laser having a repetition rate of 80 MHz and a pulsewidth of approximately 100 fs. (b) Pulses have a bandwidth of approximately 10 nm. (c) Fluorescence is isotropically emitted, whereas optical harmonic is mainly forward-directed. . . . .	4
2.1	Schematic diagram of a conventional fibre consisting of two bulk materials. . . . .	22
2.2	Scanning mechanisms in miniaturised microscopy. (a) Proximal scanning of a fibre bundle. (b) Mechanical resonance of fibre tip with piezoelectric actuators. (c) A MEMS mirror. . . . .	25
2.3	Image formation of a GRIN lens. (a) Ray path through a GRIN lens. (b) Dependence of the working distance on the fibre-lens spacing for a 0.2-pitch, 0.5-mm GRIN lens. . . . .	28
2.4	Schematic diagram of PCFs. (a) A high-index guiding PCF with a solid silica core. (b) A hollow-core PCF guiding light with photonic bandgaps. . . . .	30
3.1	Schematic diagrams of the experimental setup for measuring the polarisation characteristics of a fibre coupler. (a) Setup for near infrared illumination. (b) Setup for visible illumination. . . . .	47
3.2	Coupling efficiency from port 1 to ports 2 and 3 at wavelength 435 nm. (a) Mode profile at port 2. (b) Mode profile at port 3. . . . .	49

3.3	Coupling efficiency from port 1 to ports 2 and 3 at wavelength 532 nm. (a) Mode profile at port 2. (b) Mode profile at port 3. . . . .	49
3.4	Coupling efficiency of the single-mode fibre coupler over the visible and the near infrared wavelength ranges. . . . .	50
3.5	(a) Degree of polarisation of 800 nm laser beams propagating through ports 3 to 1 as a function of the incident polarisation angle at port 3. (b) Degree of polarisation of a pulsed beam as a function of the input power at port 3 with linear polarisation. . . . .	51
3.6	Degree of polarisation of visible beams at 435 nm (solid curve) and 532 nm (dashed curve) guided from ports 1 to 2 as a function of the incident polarisation angle at port 1. . . . .	52
3.7	Schematic diagram of the experimental SHG microscope using a single-mode fibre coupler. (a)-(c) Mode profiles in the excitation and signal arms when a visible beam is coupled to port 1. O <sub>1</sub> and O <sub>2</sub> : 0.25 NA 10× microscope objectives, O <sub>3</sub> : 0.85 NA 40× imaging objective, ND: Neutral density filter, BF: Bandpass filter, FM: flip mirror. . . . .	54
3.8	Nonlinear optical spectra in a nonlinear optical microscope using the single-mode fibre coupler. (a) Emission spectrum of AF-50 dye at wavelength 800 nm. (b) Emission spectra as a function of the excitation wavelength over the range of 780 – 870 nm. (c) SHG peak intensity of the spectra as a function of the excitation wavelength with (solid curve) and without (dashed curve) fibre coupler. The excitation power is approximately 4 mW on the sample and the excitation polarisation is parallel to the fundamental laser polarisation. . . . .	56
3.9	SHG axial response to a thin layer of AF-50 dye at wavelength 800 nm. (a) Axial response curves as a function of the input power to port 3 of the fibre coupler. (b) Quadratic dependence of the SHG peak intensity of axial response curves on the excitation power. . . . .	58

3.10	Axial responses to a thin layer of AF-50 dye in a nonlinear optical microscope using a fibre coupler for SHG collection (solid curve) and TPEF collection (dashed curve). The excitation wavelength is 800 nm. . . . .	59
3.11	Axial resolution performance of a SHG microscope using a fibre coupler as a function of excitation wavelength. (a) SHG axial responses of the system at excitation wavelengths of 800 nm (solid curve) and 860 nm (dashed curve). (b) SHG axial resolution of the system as a function of detected SHG wavelengths.	60
3.12	SHG and TPEF images of a triangle-shaped paper sheet excited by parallel polarisation (top) and perpendicular polarisation (bottom) beams at wavelength 800 nm. The excitation power is approximately 4 mW on the sample. SHG images ((a) and (d)) are obtained with a 400/9 nm bandpass filter and TPEF images ((b) and (e)) with a 510/20 nm bandpass filter. Images in (c) and (f) are obtained by overlaying the SHG and TPEF images. Scale bar is 50 $\mu m$ . . . . .	62
3.13	SHG polarisation anisotropy measurement with the KTP crystal powder in a laser scanning microscope. (a)-(b) SHG images obtained with orthogonal polarisation orientations of the analyser. (c) Dependence of the SHG intensity on the rotation angle of the analyser, where the results fit a $\cos^2 \theta$ function. Scale bar is 5 $\mu m$ . . . . .	63
3.14	SHG polarisation anisotropy measurement with the KTP crystal powder in SHG microscopy using a single-mode fibre coupler. (a) A set of SHG images of the KTP crystal powder obtained by rotating the analyser. (b) Dependence of SHG intensity on the rotation angle of the analyser, where the results fit a $\cos^2 \theta$ function. Scale bar is 5 $\mu m$ . . . . .	64

3.15	SHG polarisation anisotropy measurement with a fish scale in SHG microscopy using a single-mode fibre coupler. (a),(b) SHG images obtained with orthogonal polarisation orientations of analyser. (c) Dependence of SHG intensity on the rotation angle of the analyser, where the results fit a $\cos^2 \theta$ function. Scale bar is $20 \mu\text{m}$ . . . . .	65
3.16	Schematic diagram of the fibre-optic nonlinear optical microscope based on a single-mode fibre coupler and a GRIN rod lens. . . . .	67
3.17	One photon reflection confocal axial response. (a) FWHM of the axial response to a plane mirror and effective NA of the GRIN rod lens as a function of the gap $d$ . (b) Transmission efficiency of the GRIN lens and peak intensity of the axial response to a plane mirror as a function of the gap $d$ . . . . .	69
3.18	(a) FWHM of the TPEF axial response to a thin layer of AF-50 as a function of gap $d$ . (b) A TPEF axial response when $d$ is 5 mm to optimise the axial resolution of the fibre-optic nonlinear optical microscope using a 0.25 pitch GRIN lens. . . . .	70
3.19	Peak intensity of the fluorescence axial response as a function of gap $d$ in a fibre-optic nonlinear optical microscope. . . . .	71
3.20	A series of $xy$ images of $10 \mu\text{m}$ fluorescence polymer microspheres acquired with a single-mode fibre coupler and a 0.25 pitch GRIN lens by (a) setting $d = 1.25$ mm, with a slice spacing of $15 \mu\text{m}$ and (b) setting $d = 5.5$ mm, with a slice spacing of $5 \mu\text{m}$ . Axial resolution for these two gap lengths are shown in Table 3.1. Each slice size is $100 \mu\text{m} \times 100 \mu\text{m}$ . The average power on the sample is 10 mW. . . . .	72
4.1	Schematic diagram of the fiber-optic SHG scanning microscope. . . . .	78
4.2	2D convolution based on Eq. 4.11. The highlighted region is the overlapped area where the integration in Eq.4.11 is performed. The coordinators for a and b are $(l/2, \sqrt{1 - (l/2)^2})$ and $(l - \sqrt{1 - n^2}, 0)$ , respectively. . . . .	81

4.3	3D CTF for fiber-optic SHG microscopy. (a) $A_1 = 0$ , $A_2 = 4A_1$ . (b) $A_1 = 1$ , $A_2 = 4A_1$ . (c) $A_1 = 5$ , $A_2 = 4A_1$ , (d) $A_1 = 0$ , $A_2 = 5$ . . . . .	84
4.4	Axial cross section of the 3D CTF for fiber-optic SHG microscopy using a fibre coupler ( $4A_1 = A_2$ ) for different values of the normalised optical spot size parameter $A_1$ . The dashed curve represents the case for $A_1 = 0$ and $A_2 \rightarrow \infty$ . . . . .	85
4.5	Normalised axial response of a perfect SHG reflector in fibre-optic SHG microscopy using a fibre coupler ( $4A_1 = A_2$ ) for different values of the normalised optical spot size parameter $A_1$ . The dashed curve represents the case for $A_1 = 0$ and $A_2 \rightarrow \infty$ . . . . .	86
4.6	(a) Half width at half maximum of the axial response, $\Delta u_{1/2}$ , as a function of the normalised fiber spot size parameter when $4A_1 = A_2$ (bottom axis) and when $A_1 = 0$ (up axis). (b) Measured axial responses in the fibre-optic SHG microscope using a single-mode fibre coupler for $A_1 = 2.0$ and $8.4$ . . . . .	87
5.1	Scanning electron microscopy image of the double-clad PCF used for nonlinear optical microscopy. . . . .	94
5.2	Coupling efficiency of the double-clad PCF in the wavelength range of 410 – 780 nm for three values of the NA (0.07, 0.25 and 0.65) of coupling objectives. . . . .	95
5.3	Mode profiles in the double-clad PCF. (a)-(f) Digital camera photograph of the output pattern from the double-clad PCF between wavelengths 410 and 800 nm. A microscope objective with 0.07 NA is used for coupling. (g) Overlay of the scanning electron microscopy image and the output pattern at wavelength 800 nm. (h) Gaussian fit of an intensity profile at the output of the fibre. . . . .	95
5.4	Degree of polarisation of the laser beam delivered by (a) the core/inner cladding region and (b) the central core of the double-clad PCF as a function of the linear polarisation angle of the incident beam at wavelength 800 nm. . . . .	97

5.5	Schematic diagram of the nonlinear optical microscope based on a double-clad PCF. O <sub>1</sub> : 0.65 NA 40× microscope objective, O <sub>2</sub> : 0.07 NA 4× microscope objective, O <sub>3</sub> : 0.85 NA 40× imaging objective, ND: Neutral density filter, BF: Bandpass filter, DCM: Dichroic mirror. . . . .	98
5.6	Axial responses of the TPEF and SHG signals from a thin layer of AF-50 dye at an excitation wavelength of 800 nm in a microscope using a double-clad PCF. The inset shows the photograph of the beam profile on the back aperture of the imaging objective. The power on the sample is approximately 1.5 mW. . . . .	99
5.7	(a)-(b) Schematic diagrams show the laser beam coupled to the core of the double-clad PCF and the output pattern after the fibre. (c) Axial responses for TPEF in the case of the well-coupled illumination in the central core and the decoupled illumination in the inner cladding of the fibre. (d)-(e) Schematic diagrams shows the laser beam decoupled to the fibre core and the output pattern after the fibre. . . . .	100
5.8	(a)-(d) Sets of TPEF and SHG axial responses in the nonlinear optical microscope using a double-clad PCF and a standard SMF. (e) Detected intensity of TPEF and SHG from the double-clad PCF-based microscope and a standard SMF-based microscope as a function of the power before the imaging objective. . . . .	102
5.9	SHG images from a scale of black tetra fish with (a) a PCF-based microscope and (b) an SMF-coupler-based microscope. Scale bars represent 10 $\mu m$ . . . . .	103
5.10	Series of SHG imaging sections from (a) a fish scale and (b) a rat tail tendon in the nonlinear optical microscope using a double-clad PCF. The image section spacing is 2 $\mu m$ . The excitation power in the fiber core is approximately 4 mW for (a) and 5 mW for (b). The scale bars represent 10 $\mu m$ . . . . .	104

5.11	SHG polarisation anisotropy measurements with (a) a fish scale and (b) rat tail tendon in a nonlinear optical microscope using a double-clad PCF. Each set of SHG images is obtained without an analyser or with orthogonal polarisation orientations of the analyser. Scale bars are 10 $\mu m$ . . . . .	105
5.12	Schematic diagram of the nonlinear optical endoscope based on a double-clad PCF, a MEMS mirror, and a GRIN lens. CO: 0.65 NA 40 $\times$ microscope objective. . . . .	106
5.13	Detected intensity and axial resolution of two-photon fluorescence as a function of the gap length between the double-clad PCF and a GRIN lens: (a) a GRIN lens of 0.5 mm diameter and (b) a GRIN lens of 1 mm diameter. Both GRIN lenses have a pitch of 0.2 at 810 nm. . . . .	107
5.14	(a) Axial responses of TPEF and SHG in a nonlinear optical microscope using a double-clad PCF and a GRIN lens. (b) Quadratic dependence of TPEF and SHG intensity on the excitation power. The 0.2 pitch GRIN lens has a diameter of 0.5 mm and an NA of 0.5. The excitation wavelength is 800 nm. . . . .	108
5.15	TPEF images obtained from two geometries of fibre-optic nonlinear microscopes: (a) using a double-clad PCF and a GRIN lens (1mm diameter, 0.2 pitch, 0.5 NA) and (b) using an SMF coupler and a GRIN lens (1 mm diameter, 0.25 pitch, 0.46 NA). Scale bars represent 10 $\mu m$ . . . . .	109
5.16	A series of SHG images of rat tail tendon obtained by nonlinear optical microscopy using a double-clad PCF and a GRIN lens. Each section has a lateral dimension of 150 $\mu m \times 150 \mu m$ and is recorded at an axial step of 5 $\mu m$ into the sample. . . . .	110

5.17	A series of nonlinear optical images of the rat esophagus tissue stained with Acridine Orange in a system using a double-clad PCF and a GRIN lens. TPEF (red) and SHG (green) visualise cell nuclei and connective tissue, respectively. Each section has a lateral dimension of $100 \mu m \times 100 \mu m$ and is recorded at an axial step of $5 \mu m$ into the sample. The excitation power on the sample resulting in TPEF and SHG signals is 10 mW and 25 mW, respectively. . . . .	110
5.18	A series of <i>in vitro</i> SHG images of connective tissues in rat stomach obtained by nonlinear optical microscopy using a double-clad PCF and a GRIN lens. Each section has a lateral dimension of $180 \mu m \times 180 \mu m$ and is recorded at an axial step of $5 \mu m$ into the sample. . . . .	111
5.19	Scanning electron microscopy image of a 1D MEMS mirror used for nonlinear optical endoscopy [146]. . . . .	112
5.20	(a) A series of SHG line profiles taken at a $10 \mu m$ step into rat tail tendon and (b) A SHG line profile from unstained rat esophagus tissue obtained with a nonlinear optical endoscope using a double-clad PCF, a 1D MEMS mirror, and a GRIN lens. . . . .	113
5.21	Scanning electron microscopy image of a 2D MEMS mirror in a nonlinear optical endoscope [147]. . . . .	114
5.22	Performance of a 2D MEMS mirror in a nonlinear optical endoscope. (a) Optical scanning angle of slow and fast axes as a function of the applied voltage. (b) A 2D raster scanning pattern generated by the MEMS mirror. . . . .	114
5.23	TPEF images of fluorescence microspheres using nonlinear optical endoscopy based on a double-clad PCF, a GRIN lens, and a MEMS mirror. The power resulting in fluorescence excitation is approximately 1.8 mW and the scanning rate of the mirror is 7 lines/second. The scale bar represents $10 \mu m$ . . . . .	115



5.24	(a) A series of SHG sections of rat tail tendon using a nonlinear optical endoscope based on a double-clad PCF, a MEMS mirror, and a GRIN lens. Imaging spacing is 10 $\mu m$ . The power resulting in the SHG imaging is approximately 30 mW. (b) $Z$ projection of SHG sections shown in (a). Scale bar is 10 $\mu m$ . . . . .	117
5.25	(a) A series of <i>in vitro</i> images of rat large intestine tissue obtained by the nonlinear optical endoscope using a double-clad PCF, a MEMS mirror, and a GRIN lens. Each section is recorded at an axial step of 7.5 $\mu m$ into the sample. Arrows in frame 3 are pointing to the intestinal crypts. The scale bar is 20 $\mu m$ . (b) 3D visualisation of the rat large intestine tissue based on the image stack in (a). Image reconstruction is performed using AMIRA (Mercury Computer Systems). . . . .	118
5.26	(a) A series of <i>in vitro</i> images of the rat stomach tissue obtained by a nonlinear optical endoscope. Each section is recorded at an axial step of 5 $\mu m$ into the sample. Arrows in frame 7 are pointing to the gastric pits of the stomach columnar mucosal tissue. The scale bar is 20 $\mu m$ . (b) 3D visualisation of the rat stomach based on the image stack in (a). . . . .	119
5.27	(a) A series of <i>in vitro</i> images of the rat esophagus tissue obtained by a nonlinear optical endoscope. Each section is recorded at an axial step of 5 $\mu m$ into the sample. The scale bar is 20 $\mu m$ . (b) 3D visualisation of the rat esophagus based on the image stack in (a). . . . .	120
5.28	(a) A series of <i>in vitro</i> images of the porcine buccal cavity mucosal tissue obtained by a nonlinear optical endoscope. Each section is recorded at an axial step of 5 $\mu m$ into the sample. The scale bar is 20 $\mu m$ . (b) 3D visualisation of the porcine buccal cavity mucosal tissue based on the image stack in (a). . . . .	121

5.29	A series of <i>in vitro</i> images of the porcine oropharynx tissue obtained by a nonlinear optical endoscope. Each section is recorded at an axial step of $5 \mu m$ into the sample. The scale bar is $20 \mu m$ . (b) 3D visualisation of the porcine oropharynx tissue based on the image stack in (a). . . . .	122
5.30	(a) A series of <i>in vitro</i> images of the porcine inner lip endothelial tissue obtained by a nonlinear optical endoscope. Each section is recorded at an axial step of $5 \mu m$ into the sample. The scale bar is $20 \mu m$ . (b) 3D visualisation of the porcine inner lip endothelial tissue in (a). . . . .	123
5.31	(a) A series of <i>in vitro</i> images of the 2008 human ovarian carcinoma cell obtained by a nonlinear optical endoscope. Each section is recorded at an axial step of $10 \mu m$ into the sample. The scale bar is $20 \mu m$ . (b) 3D visualisation of the human ovarian cancer tissue. . . . .	124
5.32	(a) A series of <i>in vitro</i> images of the humanu-87 MG glioblastoma tissue obtained by a nonlinear optical endoscope. Each section is recorded at an axial step of $5 \mu m$ into the sample. The scale bar is $20 \mu m$ . (b) 3D visualisation of the breast cancer tissue. . . . .	124
6.1	Schematic diagram of the fabrication process of the double-clad PCF coupler.	129
6.2	Coupling efficiency at output ports 2 and 3 of the double-clad PCF fibre coupler having a coupling-starting pulling length of 6.1 mm as a function of the illumination wavelength at input port 1. Insets, digital camera photographs of output patterns of the double-clad PCF coupler at wavelength 800 nm. . . . .	131
6.3	Coupling efficiency at output ports 2 and 3 of the double-clad PCF fiber coupler having a longer coupling-starting pulling length as a function of the illumination wavelength at input port 1. Insets, digital camera photographs of output patterns of the double-clad PCF coupler at wavelength 800 nm. .	132

6.4	(a) Scheme diagram of a three-port coupler with a splitting ratio of $x/(1-x)$ . (b)-(c) Detected nonlinear signal intensity as a function of coupling ratio in the excitation arm in two- and three-photon processes, respectively. . . . .	133
6.5	Schematic diagram of the nonlinear optical microscope with a three-port double-clad PCF coupler and a GRIN lens. Mirror $M_2$ (shown dashed) is located on a different plane from Mirror $M_1$ . ND: neutral density filter, BF: bandpass filter, CO: coupling objective. . . . .	134
6.6	TPEF axial response to a thin layer of AF-50 dye in a nonlinear optical microscope using a double-clad PCF coupler and a GRIN lens. The excitation wavelength is 800 nm. . . . .	135
6.7	(a) TPEF image sections of 10 $\mu m$ diameter fluorescent microspheres and (b) SHG image sections of KTP crystal powder. Each set of images has an axial depth of 5 $\mu m$ into the sample. The excitation wavelength is 800 nm and a 400/9 nm bandpass filter is placed before the PMT when SHG images are acquired. The excitation power is approximately 10 mW on the sample. Scale bars represent 10 $\mu m$ . . . . .	136
7.1	Schematic transverse cross-section of an engineered double-clad PCF. The profile of effective refractive index is shown at the bottom of the figure. . . . .	144

# List of Tables

2.1	Features of nonlinear optical microscopy using various nonlinear optical phenomena. . . . .	15
2.2	PCFs related to nonlinear optical microscopy. Scale bars represent 10 $\mu m$ . Photographs of PCFs are kindly provided by Crystal Fibre A/S. . . . .	31
2.3	Various fibre-optic nonlinear optical microscopy. . . . .	42
3.1	Characterisation of the GRIN lens-fibre spacing in a fibre-optic nonlinear optical microscope. * These axial resolution values are applied in Fig. 3.20 with 10 $\mu m$ beads imaging. . . . .	72

# Chapter 1

## Introduction

Humans have always desired to explore the macrocosm and the microcosm that cannot be captured directly by our retinas. An optical microscope has been one of the most fundamental instruments to visualise microstructures since Leeuwenhoek in 1673. In particular in life sciences, optical microscopy today is a fascinating tool to provide incredibly detailed views of living cells and document the dynamism of life [1,2].

Confocal scanning microscopy proposed by Minsky in 1955 [3] has been a renaissance for the traditional microscopy technique by achieving a three-dimensional (3D) view [4]. Since the invention of two-photon fluorescence microscopy in 1990 [5], this magic technique based on nonlinear optical phenomena has revolutionised the fields of optical microscopy because of its ability to image deep tissue and produce inherent optical sectioning [6–8]. Not surprisingly, these might be just the inception of a transformation that microscopy will experience in the coming years.

This chapter serves as an introduction to nonlinear optical endoscopy, an emerging stream in research fields of nonlinear optical microscopy that aims to develop a miniaturised device for *in vivo* nonlinear optical imaging. The chapter also describes the objectives and the arrangement of the thesis.

## 1.1 Introduction to nonlinear optical endoscopy

To date, nonlinear optical microscopy has become an indispensable laboratory tool of high-resolution imaging of physiology, morphology, and cell-cell interactions in thick tissue and in live animals. It fills a niche for biological imaging as the best non-invasive means of microscopic imaging modalities [5–8]. Therefore, nonlinear optical microscopy has found extensive applications in biology and medicine, particularly in neuroscience and cancer research [8–11]. However, at present applications of nonlinear optical microscopy to *in vivo* imaging are limited to situations that involve tissue excision for observations on the bench top. To date a key technology for *in vivo* applications in human subjects and minimally surgical procedures is an endoscope that overcomes the physical limitation and remains great functionalities as well [12–14]. As a consequence, to further extend the applications of nonlinear optical microscopy, a nonlinear optical endoscope will be a soul instrument that combines the advantages of both nonlinear optical microscopy and endoscopy to permit cellular imaging within hollow tissue tracts or solid organs that are inaccessible with a commercial optical microscope.

To develop a nonlinear optical endoscope that is actually a miniaturised nonlinear optical microscope, it is of importance to understand the fundamentals of nonlinear optical microscopy and its technique challenges, which will be introduced in the upcoming subsections.

### 1.1.1 Nonlinear optical microscopy

Optical microscopy can be distinguished between linear and nonlinear optical effects. Traditional optical microscopy, including confocal microscopy, is based on single-photon processes, in which light-matter interactions have a linear dependence on the incident light intensity. Using high-order light-matter interactions involving multi-photon processes, nonlinear optical microscopy is fundamentally different and therefore

exhibits unique imaging properties.

There are several major optical nonlinear effects used in biological imaging, including multi-photon absorption, higher harmonic generation, and coherent anti-Stokes Raman scattering (CARS). Among them, fluorescence excitation under two-photon absorption is the most popular method to generate imaging contrast. Since the two-photon process requires two photons to interact simultaneously with a molecule and the two-photon excitation cross section is normally 40 orders smaller than that under single-photon excitation [7, 15], a femtosecond pulsed laser in the near infrared wavelength range is used to localise excitation light in space and time. Compared with its single-photon counterpart, multi-photon fluorescence microscopy takes advantages of intrinsic 3D resolution, greater penetration depth with less phototoxicity, and enhanced spectral flexibility.

In addition to multi-photon fluorescence, second or third harmonics can occur when ultrashort pulses interact with biological tissue to generate harmonics of the laser frequency [16–18]. In second harmonic generation, two photons simultaneously interact with noncentro-symmetric structures, producing visible photons at exactly half of the excitation wavelength [19]. As opposed to multi-photon absorption, harmonic generation is a coherent (phase-preserving) process, and therefore produces highly polarised and predominantly forward-directed radiation rather than isotropic emission. This feature can be used to visualise intrinsic structures without exogenous labeling as well as determine the absolute orientation and organisation degree of protein structures in tissue.

Another nonlinear optical process used for biological microscopy is CARS, which is a chemically specific nonlinear imaging technique and sensitive to molecular vibration states [20]. Different from the contrast caused by fluorescence emission and harmonic generation, inherent molecular vibration signals contain molecular signatures that can be used for identifying biochemical components in tissue. CARS microscopy has proven useful for mapping lipid compartments, protein clusters, and water distributions in tissue.

All these nonlinear optical imaging techniques offer unique approaches to visualise tissue structures three-dimensionally with high-resolution and non-invasive means. In particular, the combination of two-photon excited fluorescence (TPEF) and second harmonic generation (SHG) has stimulated new insights and information about the cancer research [21–24]. TPEF from intrinsic fluorophores (such as NADH and Flavins) and SHG from extracellular matrix (such as collagen and microtubules) provide complementary information on general tissue morphology, redox state and fibril orientation. Therefore nonlinear optical microscopy will be an effective alternative to standard histopathology by producing nonlinear emission spectra and images at the cellular level from deep tissue.

A schematic diagram of a typical nonlinear optical microscope is shown in Fig. 1.1. The femtosecond pulsed laser source is usually a Ti:Sapphire oscillator with a tunable wavelength range over 700 – 1000 nm. The beam is scanned by the  $xy$  scanner (usually a pair of galvanometric mirrors) before focused by the microscope objective.

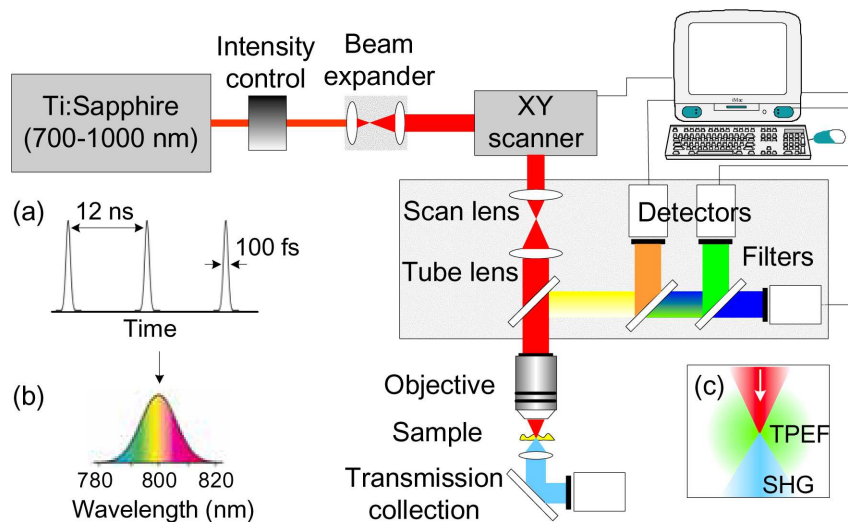


Fig. 1.1: Schematic diagram of a nonlinear optical microscope. (a) Ultrashort pulses from a Ti:Sapphire laser having a repetition rate of 80 MHz and a pulsewidth of approximately 100 fs. (b) Pulses have a bandwidth of approximately 10 nm. (c) Fluorescence is isotropically emitted, whereas optical harmonic is mainly forward-directed.



### 1.1.2 Challenges in nonlinear optical endoscopy

Applying a bulk nonlinear optical microscope for *in vivo* monitoring and diagnosis remains a challenge. The development of nonlinear optical endoscopy that permits nonlinear optical imaging under conditions, in which a conventional nonlinear optical microscope cannot be used is obviously an absolute prerequisite. The core concept is to develop miniaturised nonlinear optical microscopes, which can be applied to epithelial tissue or internal organs of living bodies, rather than examine excised tissue with bulk nonlinear optical microscopes on a bench top. With the advances in optical fibres, micro-optics, and micro-mechanics, this field has been expanding at an incredible speed in the past five years. Although rapid progress has shown the promising landscape, efforts for both instrumentation and knowledge of fibre-optic nonlinear optical microscopy and endoscopy are still in an early stage. To achieve the final aim for *in vivo* applications of nonlinear optical endoscopy, there are several key challenges summarised in the following.

*Multiple imaging modalities.* As we have mentioned in Section 1.1.1, the multi-photon excitation, higher harmonic generation, and CARS can have fundamentally different insights to accomplish selective visualisations of components inside tissue. More importantly, they are usually simultaneous processes under the illumination with ultrashort pulses in conventional nonlinear optical microscopy. Therefore, combinations of multiple nonlinear optical imaging modalities in an endoscope can be of great utility for studying biomedical events in living bodies and drive the progress in nonlinear optical endoscopy. Although there has been a number of fibre-optic nonlinear optical microscopes developed since its first demonstration in 2001 [25], the imaging contrast mechanism is primarily relies on TPEF [26–30]. There has been no report on fibre-optic SHG microscopy before the research undertaken in this thesis. The difficulty in developing fibre-optic SHG microscopy is due to the fact that SHG has polarisation anisotropy and the emission wavelength does not fall into the operation windows of conventional fibre-optic components. Furthermore, imaging theory has not been studied to understand the coherent optical imaging process through fibre-optic SHG

microscopes.

*Sensitivity.* As an imaging technique for *in vivo* applications, the great challenge in developing nonlinear optical endoscopy concerns its signal level after the integration of fibre-optic components for miniaturisation. This challenge primarily arises from a single-mode fibre (SMF) which is typically used in fibre-optic nonlinear optical endoscopy [25–27]. A key problem with using an SMF is its limited ability for efficient excitation delivery and signal collection. On the one hand, ultrashort pulses ( $\sim 80 - 200$  fs in duration) through an SMF experiences severe temporal and spectral broadenings due to group-velocity dispersion, self-phase modulation, and self-steepening [31], leading to significant reductions in the efficiency of nonlinear excitation and penetration depth. On the other hand, a low numerical aperture (NA,  $\sim 0.1$ ) and a small core size ( $\sim 5 \mu m$ ) of an SMF make the fibre sensitive to optical aberrations in imaging systems and therefore limit the collection efficiency of the nonlinear emission at sample sites. Furthermore, the small fibre core acting as a confocal pinhole blocks multiply scattered photons outside the focal volume in biological tissue, resulting in less photons contributing to the imaging formation. An alternative fibre is a multimode fibre that is superior for signal collection as a result of its relatively greater NA and large core size. Unfortunately, multiple spatial modes from multimode fibres cannot be focused to a near diffraction-limited spot to produce efficient nonlinear excitation for high optical resolution. For these reasons, the use of appropriate fibres hence is the heart of the endoscope design.

*Scanning mechanisms.* Although optical fibres allow for remote delivery of light to a given spot, they have to be combined with a scanning mechanism to form a two-dimensional image. Proximal and distal methods are two common scanning mechanisms used for endoscopy. Proximal scanning involving a pair of galvanometric mirrors and a fibre bundle can offer a stationary and ultra-small endoscope probe [29]. However, the lateral resolution is restricted by the crosstalk and the size of pixels in the fibre bundle. Distal scanning is achieved by driving mechanical resonance vibrations of the fibre tip or scanning the laser beam at the fibre end with a micromirror [30,32]. The

current problem of these scanning units is they are bulk and slow. To be applicable in nonlinear optical endoscopy, the miniaturised scanning mechanisms should have compact sizes below 3 mm and rapid scanning rates for studying fast activities and elimination of photobleaching.

*Mechanical flexibility.* The main advantage of nonlinear optical endoscopy over conventional nonlinear optical microscopy is its mechanical flexibility arising from a compact arrangement. In addition to working as a stand-alone tool, a nonlinear optical endoscope should be sufficiently small and flexible to be inserted into the working channels of a clinical endoscope, enabling access to remote locations in the body. To this end, the nonlinear optical endoscope probe should be restricted to a maximum outer diameter of 3 mm with a rigid distal assembly shorter than 10 mm. Thus, it is crucial to choose micro-optics elements and design the endoscope probe to meet this criterion. Components based on micro-optics and microfabrication technology definitely have great potential to meet these optomechanical demands.

## 1.2 Thesis objectives

The objective of this research is to exploit novel fibre-optic nonlinear optical endoscopy and understand its performance with microscope imaging theory, leading to innovations in nonlinear optical microscopy in terms of instrumentation and knowledge. This objective is achieved in two aspects.

First, a TPEF and SHG microscope using an SMF coupler is designed, constructed, and characterised. It is the first demonstration of a fibre-optic SHG microscope. Image formation of the fibre-optic SHG microscope is analysed by the 3D coherent transfer function (CTF).

Fibre-optic TPEF microscopy based on an SMF coupler has been successfully demonstrated, exhibiting advantages of great flexibility, enhanced optical sectioning and self-alignment [26, 27]. However, different from TPEF, SHG has polarisation

anisotropy and the emission wavelength is further away from the operation wavelength of the coupler. To open the possibility of fibre-optic nonlinear optical microscopy having multiple imaging modalities, the effectiveness of an SMF coupler for SHG microscopy is investigated in this thesis. Propagation characteristics of the SMF coupler under various operation conditions, which are important for simultaneous TPEF and SHG detection through the system, are studied. Furthermore, the arrangement based on a single fibre and a single gradient index (GRIN) lens has a significant impact on the imaging performance of the fibre-optic system. As a consequence, these effects are measured and evaluated.

To gain an understanding of fibre-optic SHG microscopy using an SMF coupler, image formalisation and numerical analysis of the 3D CTF are explored. The spatial frequency passband of fibre-optic SHG microscopy is theoretically studied and compared with that of fibre-optic reflection-mode non-fluorescence microscopy. Axial resolution and signal level as a function of the normalised fibre spot size parameters in fibre-optic SHG microscopy are investigated both theoretically and experimentally.

Second, the concept of the utilisation of a double-clad photonic crystal fibre (PCF) and a double-clad PCF coupler is proposed and adopted to a novel nonlinear optical endoscope. Hence the development of nonlinear optical endoscopy shifts to a new paradigm that aims at *in vivo* imaging with high efficiency. The investigations undertaken in this thesis concern the construction and characterisation of compact nonlinear optical microscopes, revealing resolution and signal level in these new systems.

A custom-designed double-clad PCF that allows for nonlinear optical imaging is first used. The ability of this double-clad PCF to deliver pulsed illumination, collect SHG and TPEF signals, and improve the efficiency of the microscope system is explored. Furthermore, to achieve a practical instrument, a micromirror based on microelectromechanical system (MEMS) is adopted to scan the illumination light in the endoscope system. An endoscope is constructed by use of the double-clad PCF and the MEMS mirror. Extensive investigations, particularly with regard to such issues

as resolution and signal level, are undertaken. More importantly, extensive imaging experiments regarding various tissues are carried out to demonstrate the functionality of the nonlinear optical endoscope.

The use of a double-clad PCF coupler can further simplify the excitation and collection light paths of the new system. There has been no report on the fabrication and application of a double-clad PCF coupler before the research undertaken in this thesis. Therefore, the possibility of fabrication of a double-clad PCF coupler is studied. Characteristics of the PCF coupler are investigated in terms of the coupling efficiency and mode propagation. The feasibility of the PCF coupler for nonlinear optical imaging is explored.

### 1.3 Preview of the thesis

The research undertaken in this thesis deals with the design, construction, and characterisation of fibre-optic nonlinear optical endoscopy. In particular, a fibre-optic microscope using an SMF coupler and a GRIN lens is thoroughly investigated. In this case, an 3D CTF analysis on fibre-optic SHG microscopy is derived to understand image formation in nonlinear optical imaging systems. Furthermore, this thesis presents a concept of nonlinear optical microscopy using a double-clad PCF, a double-clad PCF copuler, and a MEMS mirror.

To introduce a foundation on which the research presented in this thesis is built, a review of current techniques used in fibre-optic nonlinear optical imaging is given in Chapter 2. Several imaging modalities used in nonlinear optical microscopy are briefly reviewed in Section 2.2. Major technology and components, which are essential to form a fibre-optic nonlinear optical microscope, are outlined in Section 2.3. A particular attention is given to the applications of PCFs to nonlinear optical sensing or imaging in Section 2.4. Four different PCFs for nonlinear optical microscopy, large-mode-area PCFs, hollow-core photonic bandgap fibres, double-clad PCFs, and highly

nonlinear PCFs, are reviewed on the basis of their principles and functions. Strengths and limitations of the existing fibre-optic nonlinear optical microscopes are discussed in Section 2.5. A summary of the review is given in Section 2.6.

Chapter 3 demonstrates TPEF and SHG optical microscopy using an SMF coupler for both illumination delivery and nonlinear emission collection. Since TPEF and SHG are fundamentally different imaging modalities and the simultaneous collection of TPEF and SHG through the SMF coupler are desirable, detailed characterisation of the SMF coupler under different conditions is presented in Section 3.2. The ability of the SMF coupler to perform SHG imaging is demonstrated in Section 3.3 through extensive investigations into nonlinear spectra, axial resolution, images, and polarisation anisotropy measurement. Section 3.4 shows the dependence of axial resolution and signal level on the GRIN lens-fibre spacing and further optimises fluorescence collection of the system based on an SMF and a GRIN lens.

Chapter 4 studies the imaging theory based on the 3D CTF for the fibre-optic SHG microscope implemented in Chapter 3. The theoretical investigation gives the image formation of the system in terms of spatial frequencies. Section 4.1 serves as an introduction to the 3D CTF and a brief review of its history in fibre-optic confocal microscopy. In Section 4.2 an analysis of SHG image formation is given followed by the formalisation of the 3D CTF in Section 4.3. The theoretical results of the dependence of axial resolution on coupling parameters are presented in Section 4.4, while the experimentally measured results are also given.

A paradigm shift in fibre-optic nonlinear optical microscopy occurs after the introduction of a double-clad PCF results in a signal level improvement of two orders of magnitude. Chapter 5 shows the integration of a double-clad PCF, a MEMS mirror and a GRIN lens to form a nonlinear optical endoscope that enables 3D nonlinear imaging for tumour and internal organ tissues. To understand optical properties of the double-clad PCF, a detailed characterisation of the coupling efficiency is undertaken in Section 5.2. In Section 5.3 the double-clad PCF is used to construct a TPEF and SHG microscope, demonstrating its capability of 3D nonlinear optical imaging. The novel

application of a MEMS mirror to nonlinear optical microscopy is shown in Section 5.4 in conjunction with a double-clad PCF and a GRIN lens. Finally, substantial 3D nonlinear optical images of various tissues obtained with the endoscope are shown in Section 5.5 and a conclusion is drawn in Section 5.6.

A nonlinear optical microscope using a novel double-clad PCF coupler for further compact design is presented in Chapter 6. This PCF coupler offers a great possibility for all-fibre nonlinear optical endoscopy. Its fabrication process is described in Section 6.2, while a particular attention is paid to the mode splitting in the coupler that is important for nonlinear optical imaging. Furthermore, a system arrangement for the compact nonlinear optical microscope using the double-clad PCF coupler is shown in Section 6.3. Investigations into axial resolution and the imaging capability of such a system are undertaken in Section 6.4.

Chapter 7 gives the conclusions drawn from the work undertaken in this thesis and includes a discussion of future work in this field. The prospect and strategies for achieving the future research are discussed in Section 7.2.

# Chapter 2

## Review of fibre-optic nonlinear optical microscopy

### 2.1 Introduction

Ever since researchers realised that microscopy based on nonlinear optical effects can provide information that is blind to conventional linear techniques, applying nonlinear optical imaging to *in vivo* medical diagnosis in humans has been the ultimate goal. The development of nonlinear optical endoscopy is the primary method to extend applications of nonlinear optical microscopy toward this goal. Fibre-optic approaches that allow for remote delivery and collection in a minimally invasive manner are normally used in nonlinear optical endoscopy. This is largely attributable to the many advantages that fibre-optics offers to imaging systems, including mechanical flexibility, self-alignment, and enhanced optical sectioning. Fibre-based imaging systems also enable minimally invasive clinical diagnostics and surgical procedures, long-term and bedside imaging studies in living subjects [33–36]. In particular, fibre-optic nonlinear optical microscopy combining advantages of fibre-optics and nonlinear optical imaging has found its niche as a complementary nonlinear optical imaging instrument [37, 38].



A detailed investigation into nonlinear optical endoscopy requires a comprehensive understanding of the optical processes that occur in these imaging modalities. It is also important to consider the features of the fibre-optic components and their optical responses after the introduction to nonlinear optical imaging. This chapter is a review of main technologies in miniaturised microscopy that have been or can be used in fibre-based nonlinear optical microscopy, with a particular attention given to the applications of photonic crystal fibres (PCFs) for nonlinear optical sensing and imaging. The chapter is organised as follows. Section 2.2 reviews fundamental principles of popular imaging modalities used in nonlinear optical microscopy. Section 2.3 looks at the major components in conventional fibre-optic nonlinear optical microscopy based on single-mode fibres (SMFs). PCFs with novel functions in nonlinear optical microscopy are reviewed in Section 2.4. Strengths and limitations of the different types of fibre-optic nonlinear optical imaging systems are also discussed in Section 2.5.

## 2.2 Nonlinear optical microscopy

Nonlinear optics has been growing at a prodigious rate after the first demonstration of SHG with a pulsed ruby laser in 1961 [19]. Over the last two decades, the development of imaging techniques based on nonlinear optical effects have been propelled by rapid technological advances in mode-locked femtosecond lasers, laser scanning microscopy and fluorescence probe synthesis. Taking advantages of high spatial resolution due to the higher-order dependence on the excitation intensity, nonlinear optical microscopy has been a powerful tool in bioscience.

Nonlinear optical effects used as imaging contrast mechanisms occur when a sample interacts with an intense laser beam and exhibits a nonlinear response to the applied field strength. In the light-matter interactions, the induced polarisation of the material subject to the vector electric field can be expressed as [19]:

$$P = \chi^{(1)}E + \chi^{(2)}E^2 + \chi^{(3)}E^3 \dots , \quad (2.1)$$

where  $\chi^{(i)}$  is the  $i^{\text{th}}$  order nonlinear susceptibility tensor. The bulk nonlinear optical susceptibilities  $\chi^{(2)}$  and  $\chi^{(3)}$  are obtained from the corresponding high-order molecular nonlinear optical coefficients (hyperpolarizability) by using a sum of the molecular coefficients over all molecule sites. Typically materials with conjugated-electron structures give large optical nonlinearities.

The usual linear susceptibility  $\chi^{(1)}$  contributes to the absorption and reflection of light in materials. The  $\chi^{(3)}$  corresponds to third-order processes such as two-photon absorption, third harmonic generation (THG), and coherent anti-Stokes Raman scattering (CARS), while second harmonic generation (SHG) results from  $\chi^{(2)}$ . The unique features of each nonlinear optical imaging contrast mechanism are summarised in Table 2.1. Not surprisingly, the combination of these nonlinear optical imaging mechanisms extends the useful range of nonlinear optical microscopy. Although this thesis is focused on two-photon excited fluorescence (TPEF) and SHG microscopy, each of nonlinear optical effects, which is of significance to optical imaging, is reviewed in the upcoming sections.

### 2.2.1 Multi-photon fluorescence microscopy

Multi-photon excitation was predicted by Göppert-Mayer in 1931, theoretically showing that multiple photons are simultaneously absorbed by a material system to achieve an excited state that corresponds to the sum of the energy of the incident photons (Table 2.1). The first experimental demonstration of two-photon absorption, just following the demonstration of SHG, was to excite fluorescence emission in  $\text{CaF}_2:\text{Eu}^{3+}$  after the invention of pulsed ruby lasers [39]. Three-photon excitation was first achieved in naphthalene crystals in 1964 [40]. Subsequently, multi-photon excitation has been applied to molecular spectroscopy. The unprecedented biological applications of multi-photon absorption began with the invention of two-photon laser scanning microscopy by Denk *et al.* in 1990 [5], originally developed for localised photochemical activation of caged biomolecules. Six years after that, three-photon fluorescence microscopy was

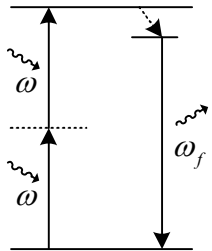
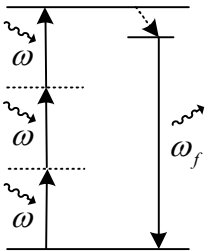
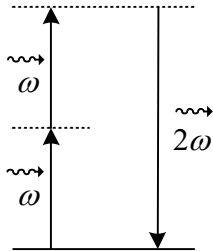
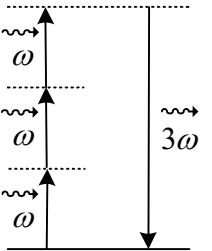
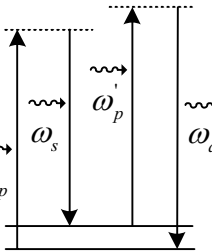
Features	2PEF	3PEF	SHG	THG	CARS
Energy level description					
Corresponding susceptibility	$\chi^{(3)}$	$\chi^{(5)}$	$\chi^{(2)}$	$\chi^{(3)}$	$\chi^{(3)}$
Discovery in optics	1961 [39]	1964 [40]	1961 [50]	1962 [51]	1965 [75]
Introduction to microscopy	1990 [5]	1996 [43]	1974 [52]	1997 [58]	1982 [76]
Advantages	<ul style="list-style-type: none"> <li>• Deeper imaging with less phototoxicity;</li> <li>• Spatial localisation for fluorescence excitation;</li> <li>• Intrinsic fluorescence from NADH, flavins, and green fluorescence protein.</li> </ul>	A new window to excite deeper ultraviolet fluorophores such as amino acids, neuro transmitters with less background and photodamage to live cells.	<ul style="list-style-type: none"> <li>• Coherent process, symmetry selection;</li> <li>• Probing well-ordered structures, functions of membranes, nonfluorescence tissues;</li> <li>• No absorption of light.</li> </ul>	<ul style="list-style-type: none"> <li>• Coherent process, no symmetry requirement;</li> <li>• No light absorption;</li> <li>• Imaging both in bulk and at surfaces for extended conjugation of pi electrons.</li> </ul>	<ul style="list-style-type: none"> <li>• Coherent process;</li> <li>• Inherent vibrational contrast for the cellular species, requiring no endogenous and exogenous fluorophores;</li> <li>• Vibrational and chemical selectivities.</li> </ul>
Main applications	Depth imaging in brain slices, combined with disease models and fluorescence indicators.	General cells and tissues morphology, redox state by use of intrinsic ultraviolet emissions.	Structural protein arrays, collagen-related diseases, membrane potential with styryl dyes.	General cells and tissues, developmental biology, neuroscience.	C-H stretching band, amide I band, phosphate stretching band in cells and tissues.
Laser sources	Tunable Ti:Sapphire laser over 700-1000 nm with a pulse width of 100 femtosecond			Optical parametric oscillator (OPO), Cr:Forsterite at 1230 nm	Picosecond Ti:Sapphire laser, OPO, Nd:Vanadate at 1064 nm

Table 2.1: Features of nonlinear optical microscopy using various nonlinear optical phenomena.

also reported and shown its imaging capability for cellular processes by harnessing the UV fluorescence of native molecules [15, 41–43].

The efficiency of multi-photon absorption depends on the multi-photon absorption cross section of the molecule, and on two or more photons interacting with a molecule simultaneously ( $\sim 10^{-16}$  s). Therefore, the maximum fluorescence output available for image formation is obtained by using ultrashort-pulsed lasers. In an  $n$ -photon process excited with laser pulses of width  $\tau$  occurring at a rate  $f$ , the fluorescence output is enhanced by a factor of  $1/(\tau f)^{n-1}$  compared to continuous-wave illumination [8]. Particularly in microscopic applications, the fluorescence strength (and potential photobleaching and photodamage related to fluorescence excitation) drops off rapidly away from the focal plane, so that inherent 3D resolution is achieved without confocal detection optics. This spatial localisation enables 3D resolved activation of caged bioactive molecules by photochemical release from an inactivating chromophore within femtoliter volumes.

In multi-photon fluorescence microscopy, ballistic (nonscattered) photons efficiently contribute to the fluorescence generation in the focal volume. The two-photon excited fluorescence signal at imaging depth  $z$  is proportional to  $e^{-2z/l_s}$ , where  $l_s$  is the mean free path describing the scattering strength of tissue. In general, near infrared light used by multi-photon fluorescence microscopy experiences less scattering in most biological tissue, and therefore gives relatively deep penetration compared with confocal microscopy [44–46]. Furthermore, multi-photon fluorescence microscopy uses wide-field detection to collect both nonscattered fluorescence photons from the focal region and multiply scattered fluorescence photons contributing to the image formation. Thus, the efficient fluorescence excitation and collection in multi-photon fluorescence microscopy make it an ideal tool to image deep into turbid biological tissue. With a laser generating 100 fs pulses with 1 W average power at wavelength 925 nm, the imaging depth of approximately 600 – 800  $\mu\text{m}$  in the neocortex is achievable [47]. The deeper penetration even can be up to 1 mm in the neocortex if a regenerative amplifier was used [47].

Multi-photon absorption spectra exhibit significant deviations from single-photon

counterparts due to their different selection rules, though emission spectra are generally similar. Multicolor imaging is allowed to excite different fluorophores simultaneously through different order processes with a single wavelength, in which emissions are spectrally shifted by hundreds of nanometers and uninterrupted for collections. Multi-photon fluorescence microscopy therefore offers great flexibility to study physiology and pathology of tissue by exciting intrinsic indicators, such as the secretion by serotonin through three-photon excitation [41, 42] and redox state by NAD(P)H through two-photon excitation [6, 23].

Advantages of multi-photon fluorescence microscopy, combined with animal cancer models and gene-expression, have provided unprecedented morphological and functional insights into tumour studies and have revealed new approaches to develop novel therapeutics that target not only the tumor surface but also internal organs [9–11]. In particular, the recent advances in semiconductor nanoparticles and metal nanoparticles, such as quantum dots [48] and gold nanorods [49], have opened up another exciting possibility for multi-photon fluorescence microscopy to study tumor pathophysiology.

### **2.2.2 Harmonic generation microscopy**

Nonlinear optical microscopy can be further extended to the use of higher harmonic light (SHG and THG), in which the energy of incident photons instead of being absorbed by a molecule is scattered via a process of harmonic up-conversion [50, 51]. SHG was the first demonstration of nonlinear optical phenomena after the invention of laser [19]. Shortly thereafter, SHG was applied to spectroscopy for interfaces characterisations and laser physics for frequency doubling. In 1974, the first combination of SHG and optical microscopy was reported to visualise the crystal structure in ZnSe [52]. However, the first biological SHG imaging experiment was demonstrated in 1986 [53], wherein SHG was used to study the orientation of collagen fibres in rat tail tendon. Due to the advance in commercial femtosecond lasers, only in the last few years has the harmonic generation microscopy been established as

the powerful imaging modality for visualisation of structural proteins in biological tissue [54–57]. The THG microscopy has also been emerging recently [58–61]. Harmonic generations, especially SHG, have been used to obtain high-resolution 3D images of endogenous arrays of collagen, microtubules and muscle myosin in wide variety of cells and tissues.

Since harmonic generation microscopy is based on nonlinear optical processes, it retains the benefits of multi-photon excitation microscopy, such as the intrinsic 3D sectioning ability and a relatively greater depth penetration. As the imaging mechanisms are different from multi-photon absorption, harmonic generations do not involve an excited state (see Table 2.1), and therefore leave no energy deposition in tissue and permit noninvasive imaging desirable for clinical applications. Furthermore, harmonic generations are coherent processes, where the phase of the radiated harmonic light is tightly matched to the phase of the applied fundamental light, so that harmonic light exhibits a significant dependence on the spatial distributions of both molecules and the field of the fundamental light.

This coherent emission feature enables the polarisation dependence of harmonic light that provides information about molecular organisation and nonlinear susceptibilities not available from fluorescence light with random phase [62–65]. Different from conventional polarisation microscopy examining the linear birefringence of samples, harmonic generation microscopy can obtain the absolute orientation of molecules by use of arbitrary combinations of fundamental and harmonic polarisations [18]. Another physical implication during the coherent processes is that harmonic emission is propagated in the forward direction. Therefore, a transmission collection geometry has been used in most of harmonic generation microscopy. However, in turbid tissue imaging with a focused beam, if the scatterer size is approximately equal to the illumination wavelength or much less, the orientation and distribution of scatterers and the off-axis angle of emission due to the Gouy phase anomaly through the focal volume have impact on the forward-directed emission profile [56, 62]. Consequently, backward SHG becomes pronounced, making the epi-collection for *in vivo* tissue

imaging practical [22, 66].

The second-order susceptibility  $\chi^{(2)}$  responsible for SHG only exists in noncentrosymmetric materials. In contrast, THG can be applied to image general cellular structures due to the nonvanishing  $\chi^{(3)}$  for all materials. Collagen fibres and cell membrane stained by styryl dyes were considered to be efficient SHG generators in the earlier research of SHG microscopy [67–71]. Recently, it has been found that several structural protein assemblies in tissue give large SHG signals without exogenous molecular probes. SHG imaging has been used to study skin, muscle, cornea, and brain pathology by visualising the effects of disease on the extracellular matrix [23, 57, 72, 73]. Another active application of SHG microscopy is cancer detection, showing that collagen in tumor models demonstrates an abnormal structure on which transformed cells exhibit the increased motility [23, 66, 74]. Particularly, the combination of TPEF from intrinsic fluorophores and SHG from endogenous structural proteins is a viable alternative to normal histological analysis and allows direct visualisation of cancer cell movement *in vivo* to understand steps of metastasis [11, 66].

### 2.2.3 Coherent anti-Stokes Raman scattering microscopy

In addition to harmonic generation microscopy, coherent anti-Stokes Raman scattering (CARS) microscopy is another 3D high-resolution imaging technique that circumvents exogenous probes. As shown in Table 2.1, CARS is a four-wave mixing process in which a pump beam at frequency  $\omega_p$ , a Stokes beam at frequency  $\omega_s$ , and a probe beam at frequency  $\omega_p'$  are interacted with a sample to result in an anti-Stokes signal at  $\omega_{as} = \omega_p - \omega_s + \omega_p'$ . In most experiments, the pump and the probe beams are derived from the same laser. The vibrational contrast in CARS microscopy arises from the resonant oscillation when the beat frequency  $(\omega_p - \omega_s)$  matches the frequency of a particular Raman active molecular vibration. Furthermore, due to its coherence nature, CARS signal generation only occurs when the field-sample interaction length is less than the coherence length. The generated CARS signal is proportional to  $(\chi^{(3)})^2 I_p^2 I_s$ ,

having a quadratic dependence on the pump field intensity and a linear dependence on the Stokes field intensity. It therefore provides the CARS microscopy a 3D sectioning capability.

The first systematic study of CARS was carried out in 1965 [75]. Since typical CARS signals are orders of magnitude stronger than the corresponding spontaneous Raman response, CARS spectroscopy has been the most extensively used nonlinear Raman technique. Although the first report on CARS microscopy [76] was more than two decades ago, rapid development has been made only in the past few years [20], attributing to the advance in pulsed laser technology. Unlike multi-photon and harmonic generation microscopy, typical CARS microscopy uses two synchronised mode-locked picosecond lasers. The picosecond pulses enable high spectral resolution with a narrower bandwidth for a specific vibrational mode and improved signal-to-background ratio.

CARS microscopy is well suited for vibrational imaging of lipids, proteins and chromosomes in unstained cells, and for mapping the distribution and diffusion of specific molecules. Recently the chemical imaging capability of CARS in bulk tissue has been demonstrated by a real-time epi-detection mode [77], showing that CARS can differentiate tissue structures based on their respective chemical composition. A combination of CARS and multi-photon fluorescence permits simultaneous vibrational and fluorescence imaging of samples [78]. Therefore CARS microscopy can be a potential tool for non-invasive optical biopsy, in which CARS adds a chemical selectivity to complement functional and morphological information provided by TPEF and SHG.

### **2.3 Fibre-optic nonlinear microscopy using single-mode fibres**

If fibre-optic and microfabrication components are introduced to nonlinear optical endoscopy, accurate knowledge of the combination of these miniaturised components



and nonlinear optical microscopy is essential to create such an imaging instrument. To date, the primary application involving fibre-optics and nonlinear optical imaging is fibre-optic nonlinear optical microscopy. In this section, main technologies for conventional fibre-optic nonlinear optical microscopy that is primarily based on SMFs are reviewed. This enables a comprehensive understanding of the performance of a fibre-optic imaging system utilising nonlinear optical phenomena, and thus provides a reasonable guidance to design a nonlinear optical endoscope for our objectives.

### 2.3.1 Single-mode fibres and ultrashort pulse delivery

Optical fibres have been extensively used in imaging and sensing systems due to their mechanical flexibility and compact size. The simplest application of optical fibres in microscopy is the delivery of light to an arbitrary location, which allows remote laser excitation or signal collections for miniaturised or portable forms of microscopy.

Optical fibres can be considered as two-dimensional (2D) structures that are effectively invariant along the length. To enable the propagation of light in such a structure, light needs to be introduced into the core with a value of the propagation constant,  $\beta$ , that cannot propagate in the cladding [79–83]. At a fixed optical frequency  $\omega$ , the maximum value of  $\beta$  that can exist in a medium with refractive index  $n$  is  $\beta = nk = n\omega/c$ . For  $\beta < nk$ , light is propagating; for  $\beta > nk$ , it is evanescent. To date two types of materials, the conventional homogeneous material and artificial fabricated photonic crystals, have been used to enable the mode guidance along a fibre. For conventional fibres (Fig. 2.1), consisting of a core surrounded by a cladding layer whose refractive index is slightly lower than that of the core, light modes are propagated in the core but are evanescent in the cladding. This is the basic principle of total internal reflection (TIR) in fibre optics. Microstructure fibres consisting of photonic crystals will be reviewed in Section 2.4.

Unlike the light delivery in linear techniques, the important issue that arises in nonlinear optical microscopy concerns temporal and spectral distortions of pulses after

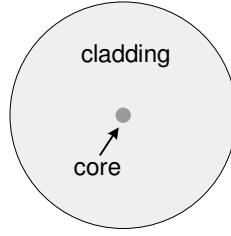


Fig. 2.1: Schematic diagram of a conventional fibre consisting of two bulk materials.

the propagation through optical fibres. Pulse propagation in fibres can be accurately described by the nonlinear Schrödinger equation given by [31]

$$\frac{\partial A}{\partial z} + \underbrace{\frac{\alpha}{2}A}_{\text{Gain/loss}} + \underbrace{\frac{i}{2}\beta_2\frac{\partial^2 A}{\partial T^2}}_{\text{Dispersion}} = i\gamma \left[ \underbrace{|A|^2 A}_{\text{SPM}} + \underbrace{\frac{2i}{\omega_0}\frac{\partial}{\partial T}(|A|^2 A)}_{\text{Self-steepening}} \right], \quad (2.2)$$

where  $A$  is the slowly varying amplitude of the pulse envelope. Eq. 2.2 implicates fundamental processes, including the linear effect of gain/loss, the dispersion through the group-velocity dispersion (GVD) parameter  $\beta_2$ , self-phase modulation (SPM) and self-steepening through the nonlinear parameter  $\gamma$ . The propagation of ultrashort pulses through an optical fibre results in temporal and spectral broadenings of the pulses due to GVD and SPM and the asymmetric spectrum shape due to self-steepening. These effects have a significant impact on the efficiency of nonlinear optical processes, and therefore limit the biomedical application of fibre-based nonlinear optical microscopy.

GVD arises from the fact that different frequency components associated with the pulse travel at different speeds given by  $c/n(\omega)$ , where  $n(\omega)$  is the refractive index of a medium. Conventional optical fibres made of fused silica are normal dispersion media ( $\beta_2 \approx 35 \text{ ps}^2/\text{km}$  at 800 nm) over the Ti:Sapphire wavelength range [31]. As a result, the spectrum of pulses is not affected, but the frequency components leaving the fibre become temporally modulated. It turns out that pulses are subject to temporal broadening with slower-moving components (shorter-wavelength) occurring near the trailing edge of the pulse whereas faster-moving components (longer-wavelength) near

the leading edge. However, it is possible to compensate for GVD in fibres by negatively prechirping, which gives different time delays for different frequency components during their passage through the prechirp unit such as gratings, prisms, and in-fibre Bragg gratings. Thus the trailing edge catches up with the leading edge during the propagation to minimise the pulsewidth leaving the fibre [31].

The efficiency of SPM in fibres is strongly dependent on the peak power of pulses and the nonlinear parameter  $\gamma = (4n_2\omega)/(c\pi d^2)$ , where  $n_2$  is the nonlinear index coefficient ( $3.2 \times 10^{-16}$  cm<sup>2</sup>/W) and  $d$  is the mode field diameter [31, 84]. For a fibre designed for single-mode operation at wavelength 800 nm,  $d$  is approximately 5.5  $\mu$ m. When high peak-power pulses are confined to this small area, an increased local refractive index gives rise to a phase shift, and therefore the spectrum of the pulse is broadened as a consequence of the time dependence of the nonlinear phase shift. Self-steepening is another interesting high-order nonlinear effect arising from the intensity-dependant group velocity, leading to a spectral blue shifting of the pulse.

According to the dispersion length  $L_D = \tau_0^2/\beta_2$  (where  $\tau_0$  is the initial pulse width) and the nonlinear length  $L_{NL} = (\gamma P_0)^{-1}$  (where  $P_0$  is the peak power of the incident pulse), for 100 fs pulses at wavelength 800 nm with an average power of 400 mW, nonlinearity dominates the propagation and the spectrum broadens significantly in the first 1.2 cm of the fibre. After this, GVD becomes the dominant effect and the pulse broadens. It is important to note that the pulse distortion through SPM, which occurs in a nonlinear manner, is difficult to be compensated by the prechirp unit that is useful for the linear dispersion. Furthermore, when the negatively prechirped pulses propagate through the fibre, SPM compresses the spectrum and results in a minimum output pulsewidth that is significantly dependent on the input power. Hence, nonlinear effects should be avoided as much as possible during pulse delivery.

The pulsewidth of a laser beam can be restored by use of a prechirp unit, if pulses with low average power ( $< 8$  mW) is delivered with a negligible SPM effect [85, 86]. However, this is less than 1% of the output from a typical Ti:Sapphire laser and relatively low for practical applications. Clark *et al.* have demonstrated a scheme

based on both spectral and temporal compression for femtosecond pulse delivery by use of two SMFs and six prisms [87]. The delivered pulses are significantly shorter than those delivered based on negative prechirping alone. Possible delivered pulse energies can be up to 5 nJ.

An alternative way for reduction of nonlinearity is to use a large-core fibre to minimise peak intensities over a larger area. It has been shown that prechirped pulses with high energy through the large-core fibre (10  $\mu\text{m}$ ) are substantially shorter than the pulses propagated through a standard SMF [84]. Consequently, two-photon excitation through an optical fibre at high power can be enhanced by use of single-mode propagation through a large-core fibre. However, a further increase of the fibre core size leads to the propagation of several transverse modes that cannot be focused to a single diffraction-limited point as well as introduce additional temporal broadening due to intermodal dispersion. Fortunately, engineering the photonic crystal structures in a fibre adds more attractive optical properties to conventional fibres. These applications of PCFs for pulse delivery will be further discussed in Sections 2.4.1 and 2.4.2.

It is important to note that the nonlinear pulse distortion during propagation can be exploited for multi-photon imaging applications. Because a reduction in illumination wavelength leads to a smaller diffraction spot size, the nonlinear spectral broadening and the spectral blue shift result in an improvement in axial resolution [88, 89]. Additionally, a broadened spectrum generated by supercontinuum through highly nonlinear PCFs enables the extended spectral window from Ti:Sapphire for TPEF imaging [90]. More details will be presented in Section 2.4.4.

In addition to SMFs, an SMF coupler consisting of one or more input fibres for distributing optical signals into two or more output fibres is one of the most important fibre components and is the guided wave equivalent of a bulk optic beam splitter. To date, fibre couplers have been used extensively in various imaging modes, including confocal microscopy and optical coherent tomography [33]. This is largely attributable to the many advantages that an SMF coupler offers, such as self-alignment, the reduction of multiple scattering, and an enhanced optical sectioning effect. In

particular, a three-port SMF coupler can deliver an ultrashort-pulsed laser beam as well as collect fluorescence signal for TPEF microscopy and endoscopy [26,27].

It should be pointed out that the current fibre-optic nonlinear optical imaging primarily relies on TPEF. More recently, CARS microscopy using an SMF has been demonstrated (see Section 2.5) [91]. There has been no report on compact imaging system using higher harmonic generation modalities. Although lots of efforts have been made, fibre-optic nonlinear optical microscopy lacks multiple imaging modalities to provide complementary information. Therefore, development of fibre-optic SHG microscopy is one of the objectives of this thesis, as will be described in Chapters 3 and 4.

### 2.3.2 Scanning mechanisms

Scanning mechanisms in miniaturised microscopy can be divided into two categories as proximal scanning and distal scanning depending on the position of the unit relative to laser sources (Fig. 2.2). Proximal scanners do not have to be inserted into a narrow working channel of an endoscope and enable a compact probe geometry. Distal scanners close to the tip of an endoscope probe are usually combined with a single fibre, offering versatile optical designs and high resolution for optical imaging.

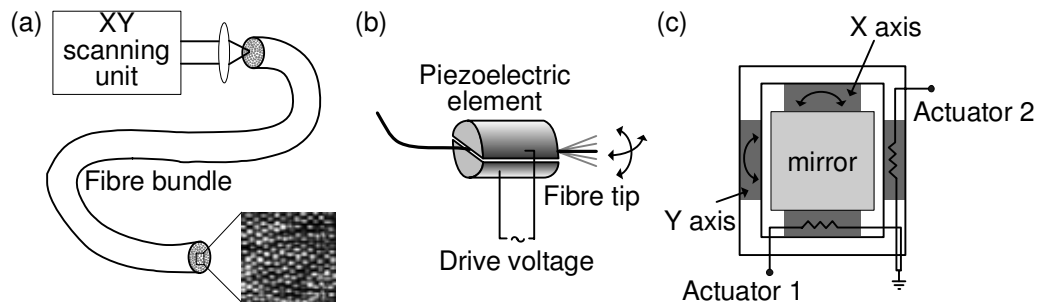


Fig. 2.2: Scanning mechanisms in miniaturised microscopy. (a) Proximal scanning of a fibre bundle. (b) Mechanical resonance of fibre tip with piezoelectric actuators. (c) A MEMS mirror.

Proximal scanning typically involves a pair of galvanometer mirrors and an imaging fibre bundle (Fig. 2.2(a)) [29,35,36]. A fibre bundle consists of up to 100,000 individual fibres closely packaged within an overall diameter of less than 3 millimeters and with a numerical aperture (NA) of approximately 0.3. The laser beam is raster scanned on the proximal end of the bundle and transferred to the distal end before focused on a specimen. Each fibre within the bundle serves as a point source as well as a detection pinhole for imaging. By choosing resonant galvanometer mirrors, imaging acquisition rates as high as 15 frame/s can be achieved [92]. However, pixilation of the fibre bundle gives rise to a limited lateral resolution dependent on the spacing of adjacent fibres. Furthermore, due to the thin cladding layer between each fibre, the leakages of excitation laser beam or collected signal to adjacent fibres can result in a reduced contrast of imaging. Nonetheless, this effect can be reduced by use of a spatial light modulator to provide sequential illumination on each fibre [93].

For illumination delivery through a single fibre, either the fibre tip or the light coupled from the fibre is scanned by a proximal scanner inside the endoscope probe [25,30,94]. A piezoelectric or an electromagnetic actuators can be excited near the mechanical resonance frequency of the fibre end to generate a 2D scanning pattern, as shown in Fig. 2.2(b). A piezoelectric bending element has been used to drive the motion of the fibre tip in a form of a Lissajous pattern [25]. The resolution and repeat frequency are determined by the ratio of driving frequencies. Alternatively, a spiral scan pattern can be produced by a tubular piezoelectric actuator consisting of two pairs of drive electrodes at a scanning frequency of approximately 1300 Hz [30]. Furthermore, a concept of the rotational scanning method has been experimentally demonstrated to achieve circumferential information inside internal organs [27].

Microfabricated mirrors based on microelectromechanical systems (MEMS) technology have rapidly emerged recently. A MEMS mirror can facilitate endoscopic beam scanning because of its small size, low power consumption, and excellent microbeam manipulating capability [95–99]. 2D scanning can be achieved with a single MEMS mirror having a mirror plate size of approximately 0.5 – 2 mm (Fig. 2.2(c)). MEMS

scanners are created through sequential material etching and deposition processes, which are similar to the technology used for the integrated circuit fabrication. MEMS mirrors are typically based on electrostatic actuation or electrothermal actuation, providing angular rotations of up to 30 degrees with low driving voltages.

MEMS mirrors have been applied to endoscopic optical coherent tomography (OCT) and confocal imaging [96–99]. Currently, a MEMS scanning OCT endoscope actuated by optical modulation is commercially available. More recently, a 2D single crystalline silicon mirror that is 0.75 mm in size driven by vertical comb electrostatic actuators has been fabricated and demonstrated for two-photon microscopy [100]. Different from the bulk galvanometer mirrors and other miniaturised scanning units, such mirrors can provide line acquisition rates up to 3.5 kHz for studying dynamic processes with high time-resolution. Although the fabrication of MEMS devices requires complicated processes and expensive facilities, MEMS technology can integrate micro-components and give enormous benefit for construction of a compact microscope, such as microscopes-on-a-chip. Therefore, a mirror based on MEMS technology is an ideal scanning mechanism not only for nonlinear optical endoscopic imaging but also for the advancement of compact microscope systems in the future.

In addition to MEMS scanning mirrors, microfabrication components such as chevron beam thermal actuators have been proposed to facilitate scanning of a GRIN lens and a micro-prism [101]. Furthermore, some novel scanning methods such as multiple laser foci produced by a micro-lens array enable high-speed multi-focal imaging. However, the signal detection requires a multianode photomultiplier tube and the cross talk between pixels usually reduces the imaging contrast [94].

### 2.3.3 Compact objective lens

Conventional microscope objectives are typically  $\sim 2 - 3$  cm in diameter and provide superior transmission efficiency and optical resolution. A miniaturised objective needs new optical design to achieve a compact size as well as retain optical properties.

Gradient index (GRIN) lenses are usually submillimeter in sizes and enormously flexible to fit imaging requirement with less cost [102, 103]. A GRIN lens uses a variable concentration of a dopant in glass to generate a special refractive index profile  $n(r) = n_0(1 - Ar^2/2)$  (Fig. 2.3(a)), where  $n_0$  is the refractive index at the centre,  $\sqrt{A}$  is the gradient constant, and  $r$  is the distance to the central axis. Unlike a conventional lens using curved surfaces to refract light, a GRIN lens uses the radial refractive index profile of a nearly parabolic shape to guide light with a cosine ray trace [79]. The period of the sinusoidal path (pitch of the lens) is given by  $p = \sqrt{AL}/(2\pi)$ , where  $L$  is the lens length.

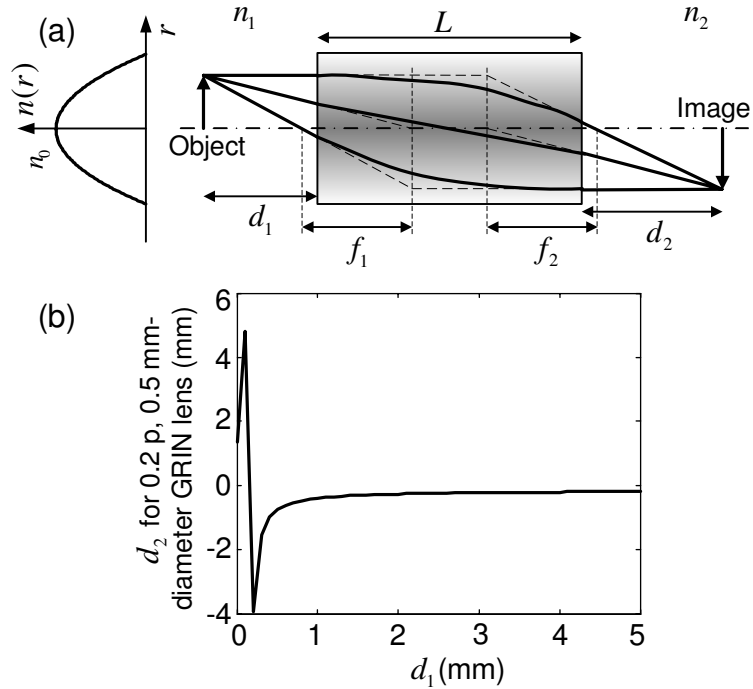


Fig. 2.3: Image formation of a GRIN lens. (a) Ray path through a GRIN lens. (b) Dependence of the working distance on the fibre-lens spacing for a 0.2-pitch, 0.5-mm GRIN lens.

Using paraxial ray-tracing matrices, image formation of a GRIN lens can be estimated. For a GRIN lens immersed in a different medium having a refractive index of  $n_m$  ( $m=1,2$ ), a collimated light will be focused to a focal spot showing an effective focal distance  $f = n_m/(n_0\sqrt{A}\sin(L\sqrt{A}))$  from the principle plane. A laser beam emerging from the fibre at a distance  $d_1$  to the GRIN lens surface can be focused to an image



distance

$$d_2 = \frac{n_0 n_2 d_1 \cos(L\sqrt{A}) + (n_1 n_2 / \sqrt{A}) \sin(L\sqrt{A})}{n_0^2 d_1 \sqrt{A} \sin(L\sqrt{A}) - n_0 n_1 \cos(L\sqrt{A})} \quad (2.3)$$

on the opposite side, as shown in Fig. 2.3(a). The scanning range on the sample can be calculated based on the transverse magnification

$$M_T = \frac{n_1}{n_1 \cos(L\sqrt{A}) - n_0 d_1 \sqrt{A} \sin(L\sqrt{A})} . \quad (2.4)$$

Fig. 2.3(b) depicts the calculated result based on Eq. 2.3, showing the lens-image distance  $d_2$  as a function of the fibre-lens spacing  $d_1$  for a GRIN lens having a diameter of 0.5 mm and a pitch of 0.2 at wavelength 830 nm (GRINTECH). It is observed that a laser beam can be focused to a spot and that the working distance  $d_2$  is monotonously decreased when the fibre-lens spacing  $d_1$  is larger than 0.2 mm.

As a great complement to a GRIN lens, a custom miniature objective can offer higher NA and less optical aberrations over a wide wavelength range. Microscope objectives having NA of 0.46 – 1.0 and outer diameters of 3 – 7 mm have been applied to confocal fluorescence endoscopy [104]. However, the achromatic range (480 – 650 nm) of those miniature objectives needs to be extended to cover the wavelength range required by nonlinear optical microscopy (350 – 1000 nm).

A more compact lens has been demonstrated as a GRIN fibre lens fabricated for monitoring brain motions *in vivo* [105]. By controlling the refractive index profile and the length of a GRIN fibre, it can function as a lens that is twice smaller than a GRIN lens in diameter. More recently, a lensed PCF has been reported, showing that the collapse of air holes and the formation of a lens on the tip of a PCF can be achieved by using an electric arc discharge [106]. Two primary parameters determining the optical properties of the lens are the length of the air-hole collapsed region and the curvature of the lens. Although these fibre-based lenses have not been demonstrated in imaging fields, the compact size and the effective focusing ability provide great potential for *in vivo* nonlinear optical endoscopic imaging.

## 2.4 PCFs in nonlinear optical microscopy

As has been mentioned in Section 2.3.1, the TIF principle in conventional optical fibres has been known for many years and the optical performance of fibres has been limited by this physical mechanism. However, within the last decade, fibres using photonic crystals as a new physical mechanism to guide light have revolutionised fibre optics. Photonic crystals are composite materials that have a periodic structure with a length scale of the order of optical wavelengths, first demonstrated in 1987 by Yablonovitch and John. In 1996, Russell *et al.* realised the first microstructured silica fibre with a periodic array of several hundred air holes running down their length, and founded the field of PCFs [83].

PCFs may be divided into two classes, high-index core fibres (Fig. 2.4(a)) and photonic bandgap fibres (Fig. 2.4(b)). In a high-index guiding fibre, a 2D photonic crystal having a lower effective refractive index than a core material can be used as a fibre cladding. As a result, modes can be guided in the solid silica core surrounded by silica-air photonic crystal cladding in a form of modified TIF (Fig. 2.4(a)). Alternatively, a hollow-core fibre enables the modes propagation in vacuum with bandgap material as a cladding layer (Fig. 2.4(b)), because the photonic bandgaps of the photonic crystal support no propagation modes [83]. Due to the 2D photonic crystals in the fibre, PCFs can control the light in the ways that are not possible or even imaginable for standard optical fibres. By engineering the air holes running along the length of the fibre, PCFs offer a greater freedom of design to overcome the limitations

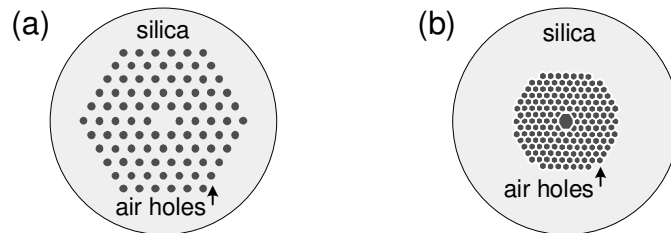


Fig. 2.4: Schematic diagram of PCFs. (a) A high-index guiding PCF with a solid silica core. (b) A hollow-core PCF guiding light with photonic bandgaps.

of a conventional silica fibre [107]. For example, PCFs can lead to a single-mode operation over a large wavelength range; the engineerable contribution of the waveguide dispersion can lead to a significant shift of the zero-dispersion wavelength towards the visible spectral region; and the high nonlinearity of the fibre core enables spectacular nonlinear effects such as the generation of broadband supercontinuum [108–110].

Unique features of PCFs have attracted unprecedented applications in ever-widening areas of science and technology. To date, several types of PCFs have been applied to or have shown great potential for nonlinear optical microscopy (Table 2.2). Although some of them have not been adopted in nonlinear optical endoscopy, a review in the upcoming subsections can provide a comprehensive understanding of these fibres for the future development of PCF-based nonlinear optical endoscopy.

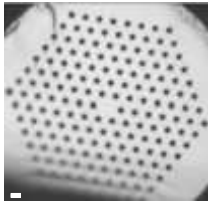
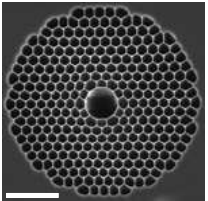
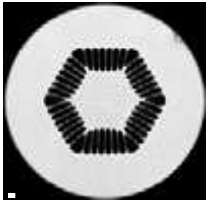
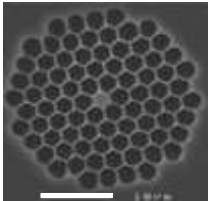
Features	LMA PCFs	Hollow-core PBFs	Double-clad PCFs	Highly nonlinear PCFs
Fibre images				
Operation wavelength	Wide range	Near zero-dispersion wavelength	Wide range	Near zero-dispersion wavelength
Advantages	Reduced SPM effect for ultrashort pulse delivery; Endless single-mode over wide wavelength range.	Low loss; High power threshold for nonlinear effects; No prechirping for high energy pulse delivery.	Reduced SPM effect in the core; High NA in the inner cladding; Dual function for pulse delivery and collection.	Extremely high nonlinear coefficient; Ideal media to generate supercontinuum for multi-spectral imaging.
Limitations	Low NA for signal collection; Dispersion compensation is required.	Narrow operating wavelength window; Low NA for signal collection.	Dispersion compensation is required.	Broadened pulse durations; inefficient collection with small core.

Table 2.2: PCFs related to nonlinear optical microscopy. Scale bars represent 10  $\mu\text{m}$ . Photographs of PCFs are kindly provided by Crystal Fibre A/S.

### 2.4.1 Large-mode-area PCFs

A large-mode-area (LMA) PCF is typically a high-index guiding type. The cladding of the fibre consists of a triangular array of air holes (see Table 2.2). The large core allowing for light guidance by modified total internal reflection is actually a high index defect created by several missing air holes. Offering new characteristics beyond those of conventional fibres, LMA PCFs have a large core size for the the single-mode operation over a broad wavelength range and significantly reduced nonlinear effects desirable for high power delivery [111].

SMFs with relatively large cores can be made using fabrication methods such as modified chemical vapour deposition simply by reducing the refractive index difference between the core and the cladding. However, the maximal core size reliably achieved by this method is limited by the accurate control of the minimal refractive index difference. In contrast, PCFs provide a greater accuracy to design the index of the cladding region for (in principle) unlimited large effective mode areas. Similar to standard step-index fibres, a normalised frequency  $V$  used for analysis of the cut-off properties of a PCF is give by [83]

$$V_{PCF} = (2\pi\rho/\lambda)\sqrt{n_{core}^2(\lambda) - n_{cladding}^2(\lambda)} , \quad (2.5)$$

where  $\rho$  is the effective fibre core radius. The effective refractive index of the core  $n_{core}(\lambda)$  and particularly the refractive index of the cladding region  $n_{cladding}(\lambda)$  are strongly wavelength-dependent. If the ratio of the guided wavelength to the hole-to-hole spacing (pitch,  $\Lambda$ ) approaches zero, the effective cladding index approaches the effective core index. Therefore, control of the hole size and distribution may tailor the exact effective refractive index of the cladding. For a high-index core fibre with given refractive indices of hole and background materials, the  $V$  value is only dependent on the ratio between the hole diameter and the hole-to-hole pitch, and increases with the ratio [83].

The unusual properties of the cladding facilitate the design of a fibre with a large mode area or with endless single-mode operation. LMA PCFs usually have a large

pitch,  $\Lambda$  approximately  $10\lambda$  or larger, and air holes diameter around  $4.5\lambda$  or smaller. Another interesting phenomenon in LMA PCFs is its single-mode guidance for any wavelength, at which silica is transparent. However, the scaling of the core size is restricted by the increasing propagation losses due to the very small effective-index contrast between the core and the cladding. So far the core diameter of a fibre maintaining its effective single-mode behavior can be up to  $35 \mu m$ .

Ouzounov *et al.* have investigated femtosecond pulse propagation through LMA PCFs [111]. The LMA PCFs have core diameters of  $15 \mu m$  and  $25 \mu m$ , respectively. Temporal and spectral shapes of prechirped pulses through the PCFs have been measured and compared with those from an SMF. It is found that a high coupling efficiency and the delivery of femtosecond pulses of high energies are achievable due to the relatively large size of core. The fibres are primarily operated in the single-mode regime, although higher-order modes can be observed in the case of misalignment. More importantly, pulse durations after the LMA PCF ( $25 \mu m$  in diameter) are less broadened compared with that after conventional optical fibres. Hence this LMA PCF allows for the delivery of 3 nJ pulses as short as 140 fs at wavelength 800 nm over a length of 1.3 meter [111].

Although LMA PCFs have been demonstrated for the effective delivery of femtosecond pulses, they have not been applied to any imaging modality. The near-diffraction-limited output beam with a femtosecond timescale from the fibre makes it well suitable for the excitation of nonlinear optical processes. However, the low NA of these types of fibres will give rise to a limited collection efficiency of nonlinear optical signals.

### **2.4.2 Hollow-core photonic bandgap fibres**

Although a hollow-core photonic bandgap fibre (PBF) was not the first demonstration of a PCF, in 1991 the idea of trapping the light inside a hollow fibre core by creating two-dimensional photonic crystals was the initial aim of research on PCFs [83]. This

motivation was driven by the formation of photonic bandgaps, where light in certain frequency ranges cannot propagate within photonic crystals materials. In PBFs, an air core is created by locally breaking the periodicity of a photonic crystal (see Table 2.2). Such a defect region supports modes with frequencies falling inside the photonic crystal bandgap of the surrounding photonic crystals. Thereby, light can only propagate in the air core but blocked from penetrating the cladding by the complete out-of-plane 2D photonic bandgap. Thus the cladding in a PBF has a higher refractive index than the core, which is radically impossible in conventional fibres.

The hollow-core PBF was first developed in 1999 [83]. After that, hollow-core PBFs have become the most fascinating manifestation of 2D photonic bandgap structures. Since light is guided in air, the effect of material nonlinearity is significantly reduced. It also enables the ultra-low loss transmission, holding the promise to break the barrier made from the conventional fibres [112]. Furthermore, the GVD of hollow-core PBFs is dominated by the waveguide dispersion. By carefully designing the size and distribution of air holes, the dispersion profile of hollow-core PBFs could change from normal to anomalous dispersion in the transmission window. Thus the zero-dispersion wavelength of the hollow-core fibre can be shifted from the conventional 1310 nm (zero-dispersion wavelength for bulk silica) to a shorter wavelength, such as 800 nm or down to a visible wavelength [107]. It also implies that anomalous dispersion at some wavelengths could support propagation of short pulses at a high power level with neither temporal nor spectral distortions as optical solitons [83].

Due to all these advantages, hollow-core PBFs are ideally suitable for high energy ultrashort pulse delivery. It has been demonstrated that propagation of 470 nJ pulses with 75 fs pulse duration at wavelength 1510 nm through a hollow-core PBF is achievable [107]. In any conventional fibre, delivery of such high power pulses is impossible due to the interplay of dispersion, nonlinearity, and fibre damage. More importantly, these fibres can be designed to support ultrashort pulse delivery at a wavelength around 800 nm particularly falling into the excitation wavelength range for TPEF microscopy.

Göbel *et al.* have first demonstrated the propagation of femtosecond pulses through a hollow-core PBF having the zero-dispersion wavelength near 810 nm [113]. Without the use of a prechirping unit, the fibre enables nearly distortion-free propagation for pulse energy of 4.6 nJ at wavelength 812 nm (corresponding to the power of 350 mW). Over the operating wavelength range, light propagated primarily in a fundamental mode. At the optimal wavelength of 812 nm, the spectral width of pulses remains unchanged for high power illumination, and the temporal broadening is negligible (not higher than 15%). After this, a number of two-photon fluorescence microscopes using the hollow-core fibre have been reported. Tai *et al.* first introduced the hollow-core PBFs to two-photon fluorescence imaging to show that image quality is comparable to that acquired by a conventional TPEF microscope [114]. Currently, hollow-core PBFs have been adopted by nonlinear optical endoscopy to deliver femtosecond pulses with high energy [94, 115].

Since hollow-core PBFs are based on photonic bandgaps of photonic crystals material, their operating wavelength is limited to a narrow wavelength range, typically several tens of nanometers around the central wavelength. For light having frequencies outside the bandgap, the modes in the core cannot be confined and attenuation of the fibre is high. Even for light guided by PBFs, the collection efficiency of the fibre is limited as a result of its low NA ( $\sim 0.1 - 0.2$ ). Furthermore, the pulse is significantly broadened below and above the zero-dispersion wavelength. This temporal broadening due to the linear GVD can be compensated by inserting prechirp components before pulses are launched into fibres. But it degrades the advantages of hollow-core PBFs. Therefore, hollow-core PBFs could not be used in a single-fibre endoscope system to facilitate simultaneous pulse delivery and backward signal collection.

### 2.4.3 Double-clad PCFs

Double-clad PCFs are the manifestation of the double-clad concept in PCFs. Traditional double-clad fibres have been made as step-index fibres of different materials,

having a rare-earth ion doping into the core as the gain media of a fibre laser. Double-clad fibres are pumped by a multimode diode through the inner cladding and provide lasing and amplification in the single-mode core. Yelin *et al.* have ever combined a normal double-clad fibre with spectrally encoded imaging to achieve high signal-to-noise ratio images with a scale of approximately 1 cm [116]. Nevertheless, the performance of the system could be further improved by use of a double-clad PCF that has the superior geometry than the fibre they used. Introducing the PCFs technology into the double-clad fibres enables an extremely high NA (up to 0.7) in the inner cladding of the PCFs with pure silica [83]. It allows more efficient pumping and higher damage threshold than double-clad fibres. The high accuracy and flexibility of the design of the effective refractive index difference between the core and the inner cladding can realise a large mode area in the double-clad PCF. The large mode area design for the single-mode signal can avoid nonlinear effects, and thus overcome the performance limitations of ultrafast fibre laser and amplifier systems with high peak power [117, 118].

In double-clad PCFs, the high NA of the inner cladding is achieved by separating the inner and outer claddings with a web of silica bridges that are substantially narrower than the wavelength of the guided light (Table 2.2). Rare-earth dopants, such as Yb, Nd, and Er, can be incorporated into the core [83]. The LMA doped core is placed in a microstructured inner cladding. The effective refractive index of the inner cladding is controlled by the size and the spacing of air holes, offering the single-mode guidance in cores for excellent beam quality of the emitted light.

If the double-clad PCFs have no rare-earth dopants as gain media in the core, it could be passive and guide light with different frequencies through different areas with high NA. Myaing *et al.* have used a double-clad PCF fabricated at the University of Bath for TPEF biosensing [119]. The fibre has an inner core diameter of 6  $\mu\text{m}$  and an NA of 0.8 for the inner cladding exhibiting a hexagonal shape. The ultrashort laser beam at wavelength 810 nm propagates through the inner core to excite a dye gelatin directly without focusing and the fluorescence emission is backward collected through the same fibre. Comparing the signal achieved under same conditions by



a standard SMF, they found that the double-clad PCF fibre improves the detection efficiency by a factor of approximately 40. However, the imaging capability of this kind of fibre, particularly the ability to perform 3D optical sectioning in nonlinear optical microscopy, had not been shown [120].

Fu *et al.* first introduced a new design of the double-clad PCF for nonlinear optical imaging, which allows for a single-fibre-based nonlinear optical endoscope for high-resolution 3D imaging [121]. The signal level of nonlinear optical microscopy based on our custom-designed fibre has been enhanced significantly by two orders of magnitude compared with the standard SMF. This result has opened up the possibilities of nonlinear optical imaging for internal organs by a new imaging device, namely a nonlinear optical endoscope. Research on double-clad PCFs-based nonlinear optical endoscopy will be presented in Chapters 5 and 6.

#### 2.4.4 Highly nonlinear PCFs

Highly nonlinear PCFs are today the most commonly used type in various PCFs. They guide light in a very small core (diameters down to  $1\ \mu\text{m}$ ) surrounded by the cobweb-like microstructure or the air-hole cladding (see Table 2.2). As we have mentioned in Section 2.3.1, the effective nonlinearity  $\gamma$  of a fibre is strongly dependent on the nonlinear coefficient of the core material and the effective mode area. Furthermore, index guiding PCFs can have a larger NA than conventional fibres by increasing the effective core/cladding refractive index difference. By use of small-scale cladding and large air-filling fractions in the PCFs, light can be confined extremely tightly within the small core. As a result, the fibre has a small effective mode area and exhibits a high nonlinearity. A typical value of the effective nonlinearity for a standard fibre is  $1\ \text{W}^{-1}\text{Km}^{-1}$ , whereas nonlinear PCFs can be designed to have a  $\gamma$  value at  $215\ \text{W}^{-1}\text{Km}^{-1}$  [83].

In addition to its high nonlinearity, zero-dispersion wavelengths of the fibre can be designed over a wide range in the visible and near infrared spectra. These

two unique features make the highly nonlinear PCFs fascinating for nonlinear applications, of which supercontinuum generation (SCG) has been the most spectacular manifestation [83]. SCG is the formation of broadband spectra when high-power ultrashort pulses propagate through a nonlinear optical medium, and was first observed in 1970. After the invention of PCF technology, the interest of SCG has been intensively renewed [108–110].

As described above, due to the small effective mode area and the zero-dispersion wavelength near wavelength 800 nm, applications of highly nonlinear PCFs have been extensively associated with standard Ti:Sapphire laser sources instead of amplified Ti:Sapphire laser. The ability to generate a supercontinuum using low-peak-power pulses from the standard Ti:Sapphire laser and a short length of highly nonlinear PCFs (several centimeters to several tens of centimeters) has led to a boom in supercontinuum research. The spectral broadening in SCG arises from the interplay of several nonlinear effects, primarily including self-phase modulation, self-steepening, stimulated Raman scattering, and four-wave mixing. Wideband SCG over an octave can be achieved by using the pump pulse in the anomalous GVD region near the zero-dispersion wavelength of the fibre. It has been demonstrated that the supercontinuum generated in PCFs has the bandwidth of sunlight but is  $10^4$  times brighter [80].

The broad bandwidth and high spectral brightness of the SCG based on highly nonlinear PCFs have been applied to a number of imaging modalities (OCT [122], CARS [78], confocal [123], and TPEF microscopy [124–127]). The combination of a highly nonlinear PCF and a grating pair has been used for pulse compression to enhance the two-photon excitation efficiency. Nonlinear PCFs can enhance the SPM-induced spectral broadening of 250 fs pulses in the positive dispersion region, and the subsequent negative dispersion from the grating pair compresses the pulses below 25 fs [124, 125]. The double frequency of the broadband spectra after the nonlinear PCFs can also be used as a complementary light source to excite dyes, whose two-photon absorption spectra are below the tunable range of a Ti:Sapphire laser [126]. In particular, broadband spectra caused by SCG enable multispectral excitation light to

acquire multicolor imaging for multifunctional visualisation [127]. A supercontinuum ranging from 700 nm to 950 nm has been used to achieve two-photon fluorescence images of nuclei, F-actin, and mitochondria of cells at three different spectral channels.

Highly nonlinear PCFs have offered novel applications of nonlinear optical microscopy. However, the small core results in a limited coupling efficiency for visible light. Thus it is an ideal light source to extend present two-photon microscopy, but not optimised for signal collection. Furthermore, the picosecond pulse duration after these nonlinear effects gives rise to a decrease of the excitation efficiency for nonlinear optical processes.

## 2.5 Geometries of fibre-optic nonlinear optical microscopy

Although the major technologies in miniaturised microscopy described in Sections 2.3 and 2.4 take enormous advantages for their own, the difficulty in creating a fibre-optic nonlinear optical endoscope is the design and integration of these technologies for an optimised nonlinear optical imaging performance. To date, fibre-optic TPEF microscopy is the primary embodiment of the development of fibre-optic nonlinear optical endoscopy. The present research in fibre-optic TPEF microscopy may be classified by applications into three categories, portable TPEF microscopy, rigid TPEF endoscopy, and flexible TPEF endoscopy.

Portable TPEF microscopy has been designed as a compact and light-weight imaging device, which can be carried by behaving animals or used for epithelial tissue imaging. Helmchen *et al.* first demonstrated a miniature head-mounted TPEF microscope suitable for studies of dendritic morphology and calcium transients in brains of anesthetized or awake animals [25]. In their design, an SMF fibre is used for both delivery of laser pulses and illumination scanning. It has been demonstrated by Bird *et al.* that a spectral blue shift in an SMF leads to an improvement in resolution under

two-photon excitation although an SMF in TPEF microscopy experiences temporal and spectral broadenings [88, 89]. This miniature microscope has sufficient resolution and flexibility to measure the neural activity on a cellular scale, but its application is limited by the imaging blurring during sudden movements of rats. Recently, a portable TPEF microendoscope having a size of  $3.5 \text{ cm} \times 1.2 \text{ cm} \times 1.5 \text{ cm}$  and a mass of only 3.9 gram has been reported [115]. It is based on a compound GRIN lens probe, and a hollow-core PBF for near distortion-free delivery of femtosecond pulses, and another high NA multimode fibre for fluorescence collection, exhibiting micrometer-scale resolution for brain imaging. Unfortunately, the use of two fibres for separate pulse delivery and signal collection hinders its further miniaturisation.

Like the traditional rigid endoscopy, TPEF microendoscopy uses the combination of several GRIN lenses as a probe to provide an enough length for imaging in deep tissues [28, 103, 128]. The compound GRIN lens probe typically has a relay lens and an objective lens with a diameter of sub-millimeter, enabling the insertion into solid tissue with minimal invasion as well as translating an image plane from proximal scanning mirrors to the focal plane in tissue. Less lenses are chosen to avoid aberrations occur in lenses of multiple pitches. Since there is no any fibre employed in the system and the GRIN endoscopes do not suffer from SPM with an illumination power less than 200 mW, the endoscope has a minimal pulse distortion compared with other geometries of fibre-optic TPEF microscopy. Although rigid TPEF endoscopy has a compact probe in diameter, it must be combined with a conventional TPEF microscope to facilitate the pulse delivery and laser scanning.

Flexible TPEF endoscopy has an optical probe with a few millimeters in diameter that can be incorporated into a traditional endoscope. It is well suited to image either epithelia tissue such as skin or internal organs such as gastrointestinal tracts and cervix. It has been demonstrated that a fibre bundle combined with a compound GRIN lens enables two-photon imaging through a 1-mm-diameter probe [29]. Its proximal scanning method also avoids vibrations of the fibre or the scanning unit during rapid accelerations. The limitation of this system arises from disadvantages of a fibre bundle

described in Section 2.3.2.

Bird *et al.* first demonstrated a two-photon endoscopy based on an SMF coupler [26, 27]. The SMF coupler exhibits unique optical properties, such as low-pass filter and inherent confocal pinhole. More importantly, the use of an SMF coupler enables an all-fibre imaging system that could not be gained by other fibre-optic devices. The application of this geometry has been extended to SHG imaging [129], which will be shown in Chapter 3 in this thesis. Since an SMF is not ideal for signal collections, the signal level of the system is inevitably low. An introduction of a double-clad PCF to the endoscopy has resulted in significant enhancement of signal level [121]. The integration of such a double-clad PCF and a MEMS mirror offers a great flexibility and a superior system performance [32]. The design and characterisation of double-clad PCF-based endoscopy will be presented in Chapter 5. More recently, Fu *et al.* have developed a method for fabricating a double-clad PCF coupler for further size reduction of the nonlinear optical endoscope [130]. The detail of this work will be presented in Chapter 6.

It should be noticed that the concept of CARS endoscopy has been experimentally demonstrated recently [91]. A step-index SMF has been used to simultaneously deliver pump and Stokes beams having pulse width of a few picoseconds and to collect the CARS signal in the backward direction. No significant changes in the profiles of pump and Stokes beams are observed below an average power of 80 mW. Since CARS is a different imaging mechanism from TPEF, a half wave plate and a delay line are inserted in the beam lines to overlap polarisations and the pulse trains to optimise the CARS signal. More recently, supercontinuum generated by a highly nonlinear PCF has enabled simultaneous CARS and two-photon fluorescence images [78]. Organelles in a living yeast cell such as mitochondria and nucleus can be visualised through the combination of CARS and two-photon processes. These studies have demonstrated a great potential of the multicolor and multifunction endoscopy by combining all these nonlinear optical mechanisms through fibre-optics.

## 2.6 Chapter summary

The aim of the thesis is to develop nonlinear optical endoscopy based on fibre-optics methods. This chapter has illustrated current nonlinear optical imaging modalities used for high-resolution 3D microscopy and reviewed important technologies that have

Geometries	Fibres	Scanning	Advantages	Limitations
Portable TPEF microscopy	Mechanical flexibility. Reduced size and weight for freely moving animals.			
Head-mounted TPEF microscopy [25]	SMF	Distal, Lissajous.	First demonstration of miniaturised TPEF microscopy.	Unstable imaging during sudden movements.
Portable TPEF microendoscopy [115]	Hollow-core PBF	Proximal, Lissajous.	Very light weight, no pulse distortion and reduced SPM.	Design of two fibres hinders miniaturization.
Handhold TPEF microscopy [94]	Hollow-core PBF	Proximal, multi-focal.	High-speed multi-focal imaging, no pulse distortion and reduced SPM.	Relatively large and heavy among the miniaturised TPEF microscopes.
Rigid TPEF endoscopy	Combination of GRIN lenses enables minimally invasive and deep imaging in tissues.			
TPEF micro-endoscopy [28,103,128]	None	Proximal, raster.	Minimal pulse distortion, deep tissue imaging.	Rigid GRIN probes, aberrations in long GRIN probes.
Flexible TPEF endoscopy	Potential applications in imaging of internal organs with great mechanical flexibility.			
SMF coupler TPEF and SHG endoscopy [26,27,129]	SMF coupler	Distal, rotational.	Mechanical flexibility, all fibre design.	Dispersion compensation needed, limited signal level.
Fibre-bundle TPEF endoscopy [29]	Fibre bundle	Proximal, raster.	Mechanical flexibility, stationary and compact probe.	Dispersion compensation needed, limited resolution.
Double-clad fibre TPEF endoscopy [30]	Double-clad fibre	Distal, spiral.	Mechanical flexibility.	Dispersion compensation needed, limited signal level.
Double-clad PCF TPEF and SHG endoscopy [32,121]	Double-clad PCF	Distal, MEMS.	Mechanical flexibility, reduced SPM, improved signal level.	Dispersion compensation needed.
CARS endoscopy [91]	SMF	None	First demonstration of fibre-optic CARS microscopy.	Scanning mechanism needed, limited signal level.

Table 2.3: Various fibre-optic nonlinear optical microscopy.

been applied to the fibre-optic nonlinear optical microscopy toward the development of nonlinear optical endoscopy. This review is of great importance if the optimised design and construction of a nonlinear optical endoscope are accomplished.

Table 2.3 gives characteristics and geometries of current fibre-optic nonlinear optical microscopes. The comparison of these system geometries shows that flexible nonlinear optical endoscopy is of importance for epithelial tissue imaging in most organs of the body. However, current fibre-optic nonlinear optical microscopy lacks multiple nonlinear optical imaging modalities, which will be explored in Chapters 3 and 4. Furthermore, PCFs play an important role to improve the performance of the system towards application of nonlinear optical endoscopy. A double-clad PCF is ideally suited to deliver the ultrashort pulses and collect nonlinear signals simultaneously for a single-fibre-based nonlinear optical endoscopy. The use of a double-clad PCF in nonlinear optical imaging can optimise the signal level of the system and overcome major limitations of other PCFs. It will be described in greater details in Chapters 5 and 6.

# Chapter 3

## Nonlinear optical microscopy using a single-mode fibre coupler

### 3.1 Introduction

Two-photon fluorescence microscopy has been widely used as the best noninvasive means of fluorescence microscopy for three-dimensional imaging in thick tissue and in live animals. Although second harmonic generation (SHG) has been demonstrated almost as soon as the first laser had been built, only more recently has it emerged rapidly as a powerful contrast mechanism in nonlinear microscopy [16–18]. As discussed in Section 2.2.2, due to its coherent scattering nature, SHG facilitates direct imaging of highly polarisable and ordered noncentro-symmetric structures without exogenous molecular probes, and polarisation anisotropy to extract nonlinear organisation of samples. Therefore, SHG imaging of endogenous proteins such as collagen, microtubules in live tissue may provide a new angle for tissue morphology, cell-cell interaction and diseases diagnosis.

At present, the majority of SHG studies in biological tissue are obtained in a transmitted detection geometry on the bench top with bulk optics, that preclude



*in vivo* applications on live animals. There has been no report on using fibre-optic components for SHG microscopy. This situation arises from two major difficulties in adopting fibre-optic components in SHG microscopy. First, the wavelength range where SHG signal falls in is further away from the designed wavelength of the fibre-optic components compared with that of normal two-photon fluorescence. Second, polarisation preservations of an illumination laser beam and the collected second harmonic signal are essential, which directly affect the visualisation of polarisable biomolecular arrays in cells and tissue. Although the polarisation feature of a fused-taper fibre device has been demonstrated at the designed wavelength [131], polarisation characteristics of fibre-optic components under femtosecond pulsed illumination and in a spectral window away from the designed window have not been reported. As we have mentioned in Section 2.3.1, two-photon excited fluorescence (TPEF) microscopy based on a single-mode fibre (SMF) coupler has been demonstrated, whereas the effectiveness of the fibre coupler has not been demonstrated in SHG microscopy due to the difficulties described above.

The aim of this chapter is to present a fibre-optic SHG microscope that uses a three-port SMF coupler. Experimental investigation is carried out in the polarisation characteristics of the fibre coupler under various illumination conditions. Performance of the fibre-optic SHG microscope is characterised and compared with that of the TPEF imaging modality. A particular attention is given to the SHG polarisation anisotropy measurement of the system. Characterisation of the nonlinear optical microscope based on an SMF coupler and a GRIN lens is also investigated to optimise signal collection and axial resolution of the system.

The structure of the chapter is divided into five sections beginning with this introduction section. Section 3.2 is the experimental investigation of polarisation characteristics of the fibre coupler under femtosecond pulsed and continuous-wave (CW) illumination. SHG and TPEF microscopy using an SMF coupler is presented in Section 3.3. The performance comparison of SHG and TPEF microscopy in terms of emission spectra, resolution and imaging is made throughout this section. In section

3.4, applications toward nonlinear optical endoscopy using an SMF coupler and a GRIN lens are evaluated through the measurement of the resolution and signal level of the system. A chapter conclusion is drawn in Section 3.5.

## 3.2 Polarisation characteristics of a single-mode fibre coupler

### 3.2.1 Experimental arrangement

Two schematic diagrams of the experiment setup for measuring the polarisation characteristics of the three-port fibre coupler are shown in Fig. 3.1 [132]. In a fibre-optic nonlinear optical microscope, a near infrared femtosecond pulsed beam is delivered through port 3 (excitation arm) to port 1 (sample arm), and the signal collected via port 1 is in the visible wavelength range and returned via port 2 (signal arm) into a photomultiplier tube (PMT). Therefore, near infrared and visible illumination is carried out in our experiment in order to understand the polarisation evolutions of the forward excitation laser beam and the backward nonlinear optical signals. To measure the polarisation characteristics of the fibre coupler under excitation laser beam illumination, a near infrared femtosecond beam and a near infrared CW beam are coupled into port 3 (Fig. 3.1(a)), respectively. Evolutions of input polarisation states can be measured from port 1. To further understand the mode profile, the splitting ratio, and the polarisation properties of the fibre coupler for the collected SHG signal, laser beams in the visible range are used to illuminate port 1, as shown in Fig. 3.1(b). In both cases, the fibre coupler is arranged to avoid strain and stress. The fibre coupler used is three-port fused silica SMF coupler (Newport, F-CPL-S12785) having an equal splitting ratio of 50/50, a core/cladding ratio of approximately 5/125, numerical aperture (NA) 0.16 and an operation wavelength of 780 nm. Each arm of the coupler is approximately 1 meter in length.

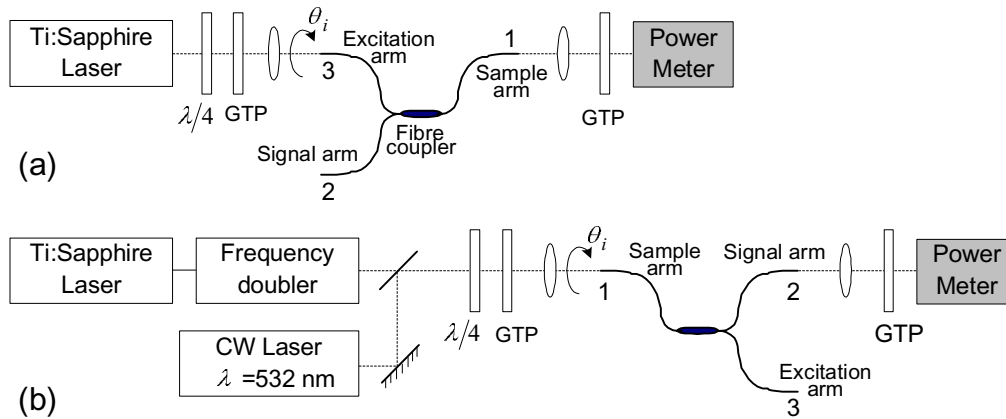


Fig. 3.1: Schematic diagrams of the experimental setup for measuring the polarisation characteristics of a fibre coupler. (a) Setup for near infrared illumination. (b) Setup for visible illumination.

To measure polarisation characteristics of the near infrared laser beam (Fig. 3.1(a)), a pulsed beam generated from a Ti:Sapphire laser (Spectra Physics, Tsunami) at wavelength 800 nm with a repetition rate of 82 MHz and a pulse width of approximately 80 fs is coupled through a microscope objective (Melles Griot, 10 $\times$ /0.25NA) into port 3. In the case of near infrared CW illumination, the laser is operated without the engagement of the mode-locking function. To obtain polarisation characteristics of the fibre coupler for visible light (Fig. 3.1(b)), firstly a femtosecond pulsed beam at wavelength 435 nm obtained by the combination of the Ti:Sapphire laser and a frequency doubler (Spectra Physics, Model 3980) is launched into port 1 via the microscope objective. Secondly a 532 nm CW beam generated from a solid state laser (Spectra Physics, Millennia) is used to illuminate the fibre coupler.

In both geometries, an arbitrary linear polarisation direction can be made by the rotation of the  $\lambda/4$  plate and the Glan Thompson polariser (GTP, Newport: 10GT04). A neutral density filter wheel placed before the coupling objective allows the variation of the input power. The linearly polarised beam is launched into the input port of the fibre coupler and the maximum ( $I_{max}$ ) and minimum ( $I_{min}$ ) powers of the output beam are measured through an analyser (GTP, Newport: 10GT04) after changing the linearly polarised beam is launched into the input port of the fibre coupler and the maximum ( $I_{max}$ ) and minimum ( $I_{min}$ ) powers of the output beam are measured through an analyser (GTP, Newport: 10GT04) after changing the incident polarisation angle  $\theta_i$  at the input port of fibre coupler. In experiments, the initial incident polarisation angle corresponds to the maximum degree of polarisation.

The input and output power from each arm of the fibre coupler is monitored with a factory calibrated portable optical power meter (Nova, Ophir).

### 3.2.2 Coupling efficiency and splitting ratio

Before characterisation of the polarisation property of the fibre coupler, it is of importance to understand the propagation properties of the SHG signal, which is in the visible wavelength range, through the fibre coupler. Particularly, considerations of the coupling efficiency and the splitting ratio need to be given to the visible range in which the fibre coupler is not designed for single-mode operation and an equal splitting ratio between ports 2 and 3 is not necessarily maintained.

To investigate into the feature, the mode profile and the coupling efficiency at ports 2 and 3 are measured, respectively, when a pulsed beam at wavelength 435 nm illuminates port 1. The result is shown in Fig. 3.2. The coupling efficiency at port 2 for 435 nm wavelength illumination is approximately 29%, with a splitting ratio of port 2 to port 3 of 99.6/0.4. More importantly, it is found that the field distribution at port 2 remains a single-mode profile (inset (a) of Fig. 3.2), whereas the field distribution at port 3 presents a profile of the LP<sub>21</sub> mode distribution (inset (b) of Fig. 3.2). This phenomenon is consistent with the estimation based on the parameter  $V$  of the fibre. At wavelength 435 nm, the  $V$  number of 3.97 allows for the propagation of LP<sub>21</sub> mode [31, 133].

To confirm the propagation properties of the fibre at the visible wavelength, the mode profile and the coupling efficiency at ports 2 and 3 are further measured with a CW beam at wavelength 532 nm launched into port 1, shown in Fig. 3.3. The measurements show that the coupling efficiency at port 2 for 532 nm is approximately 41% and the splitting ratio is 99.7/0.3. A lower-order mode, LP<sub>11</sub> mode, is observed at port 3 because of the  $V$  value of 3.24 for wavelength 532 nm, while light emerging at port 2 still remains a single-mode profile. These results confirm that the propagation properties of the coupler are similar in both cases. The reduction in the coupling

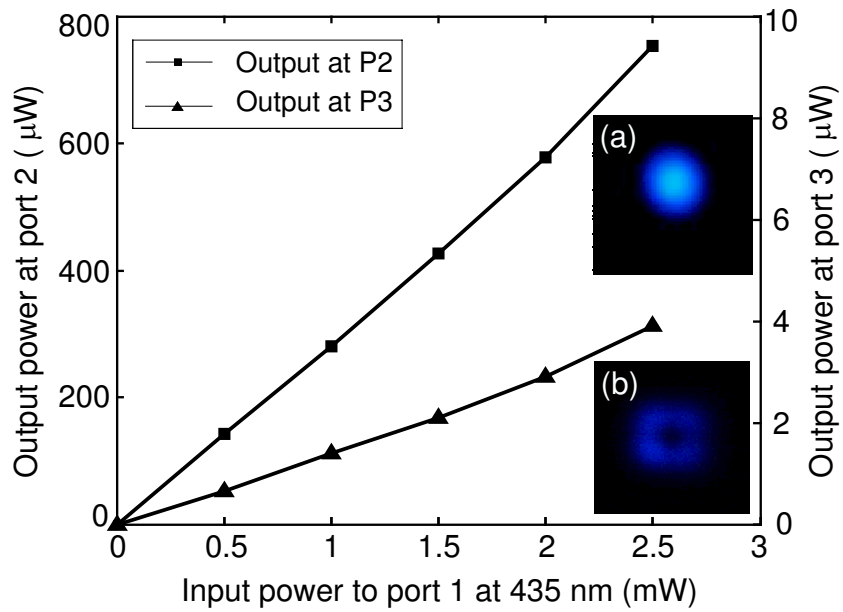


Fig. 3.2: Coupling efficiency from port 1 to ports 2 and 3 at wavelength 435 nm. (a) Mode profile at port 2. (b) Mode profile at port 3.

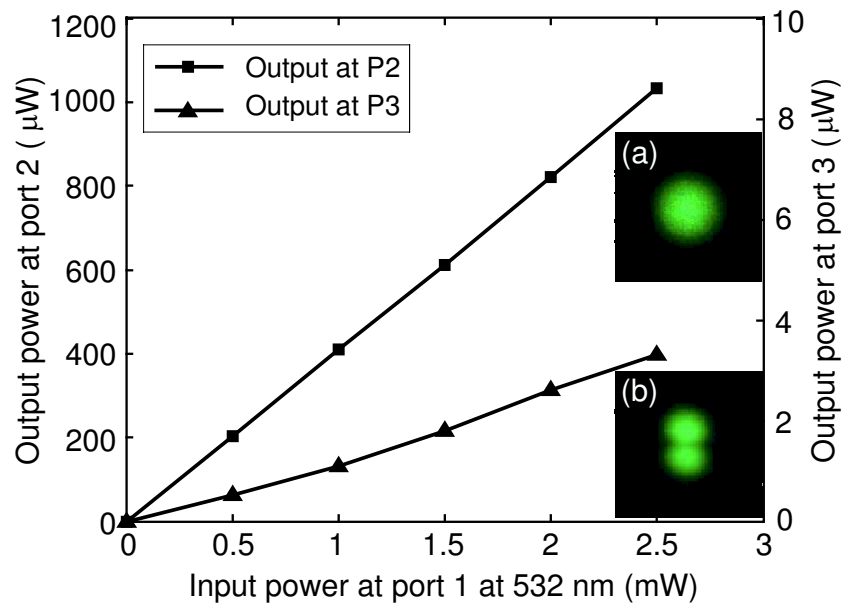


Fig. 3.3: Coupling efficiency from port 1 to ports 2 and 3 at wavelength 532 nm. (a) Mode profile at port 2. (b) Mode profile at port 3.

efficiency at wavelength 435 nm may result from the greater loss of a higher-order mode at the coupler junction.

The coupling measurements show that the fibre coupler can act as a low-pass spectral filter at a visible wavelength. Furthermore, port 2 is ideally suited to be a signal arm, since the strength of the visible beams guided by the fibre coupler in this arm is two orders of magnitude higher than that in the excitation arm. The coupling efficiency of the fibre coupler over the whole wavelength range are depicted in Fig. 3.4. The coupling efficiency from port 3 in the excitation arm to port 1 is 20 – 41% in the wavelength range 770 – 870 nm, while almost 100% of the visible light in the sample arm (port 1) splits into the signal arm (port 2). As a result, using port 3 for delivery of a pulsed laser beam and port 2 for signal collection may maximise the strength of nonlinear signals.

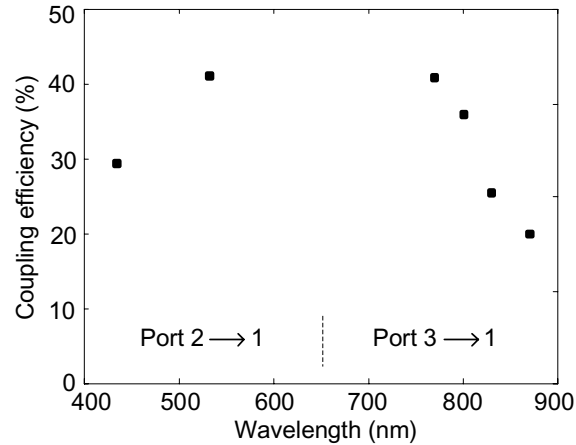


Fig. 3.4: Coupling efficiency of the single-mode fibre coupler over the visible and the near infrared wavelength ranges.

### 3.2.3 Degree of polarisation

To characterise the output polarisation states under various illumination conditions, we introduce the degree of polarisation defined as  $\gamma = (I_{max} - I_{min}) / (I_{max} + I_{min})$  [134]. The variation of the output polarisation states of the CW and pulsed beams at wavelength 800 nm through the fibre coupler (port 3→1) as a function of the incident polarisation

angle  $\theta_i$  at port 3 is shown in Fig. 3.5(a). It is seen that the linear polarisation states can be preserved in the conventional SMF coupler at certain incident angles in both CW and pulsed illumination cases with different input powers.

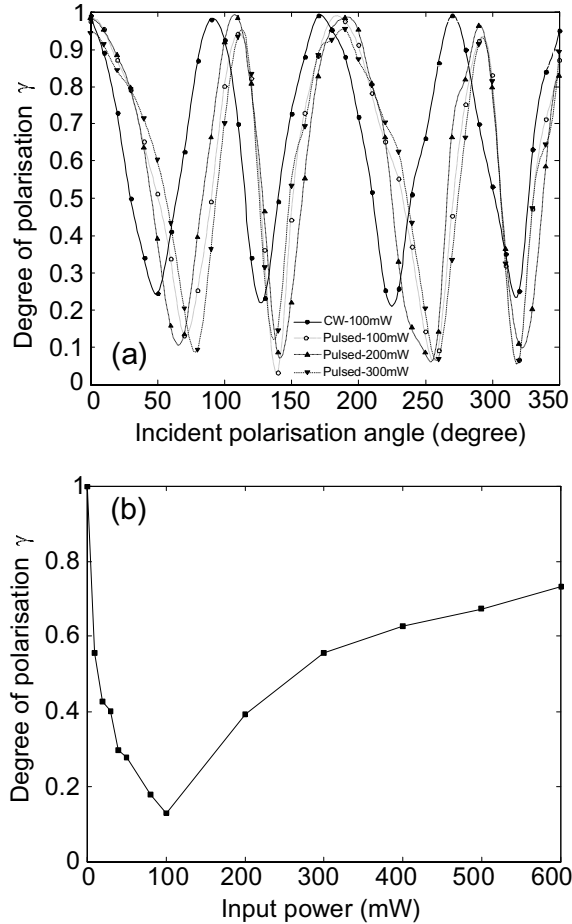


Fig. 3.5: (a) Degree of polarisation of 800 nm laser beams propagating through ports 3 to 1 as a function of the incident polarisation angle at port 3. (b) Degree of polarisation of a pulsed beam as a function of the input power at port 3 with linear polarisation.

Different from the CW illumination, the pulsed illumination can lead to a number of nonlinear phenomena, such as self-phase modulation (SPM) and self-steepening. Consequently, a nonlinear depolarisation response varies significantly with the input power. Fig. 3.5(b) shows the dependence of  $\gamma$  on the input power of the pulsed beam having linear polarisation. Due to the birefringence and SPM, the measured depolarisation dependence exhibits an oscillatory behaviour while the depolarisation effect remains constant in the case of CW illumination [134].

It should be pointed out that pulsed illumination can give rise to a nonlinear depolarisation response, but the linear polarisation can still be maintained at certain incident angles. In Fig. 3.5(a), while SPM caused by the intensity-dependence of the refractive index results in pulse broadening and a phase mismatch between the two orthogonal polarisation components, the maximum degree of polarisation as high as 0.96 is achieved in the case of 300 mW input power that is sufficient to excite biological samples.

In the same manner as shown in Fig. 3.5(a), Fig. 3.6 shows the polarisation characteristics of the fibre coupler (port 1 $\rightarrow$ 2) at wavelengths 435 nm and 532 nm. It is observed from the data that the linear polarisation states of the visible beam in both pulsed and CW conditions propagating through the conventional fibre coupler can be maintained at certain incident polarisation angles. A further observation of Figs. 3.5 and 3.6 reveals that the maximum degree of polarisation appears at an angular interval of approximately 90 degrees of the incident polarisation angle. This feature may be caused by the birefringence effect of the fibre. Normally, fused silica glass used in optical fibres does not have significant birefringence for glass lack crystalline structures. Real fibres, however, experience inhomogeneities and imperfections, which

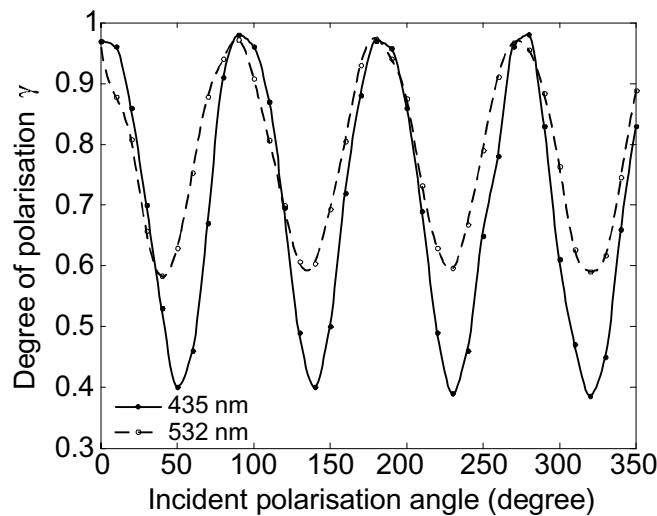


Fig. 3.6: Degree of polarisation of visible beams at 435 nm (solid curve) and 532 nm (dashed curve) guided from ports 1 to 2 as a function of the incident polarisation angle at port 1.



produce a low level of birefringence. As a result, the linear polarisation state of a light beam launched along an axis of a birefringence fibre can be maintained.

These results demonstrate that the linear polarisation states of pulsed and CW beams over a range from near infrared to visible wavelengths can be preserved in a conventional three-port SMF coupler. The degree of polarisation of approximately 1 is obtained at an angular interval of approximately 90 degrees of the incident linear polarisation angle. It implies that the polarisation characteristics of the fibre coupler enable the delivery of a linearly polarised excitation beam in the near infrared range and the propagation of well-polarised SHG signal at a visible wavelength. The capability of the SMF coupler for anisotropy polarisation measurement will be presented in Section 3.3.5.

## **3.3 A SHG microscope based on a single-mode fibre coupler**

### **3.3.1 Experimental arrangement**

The experimental arrangement of the SHG microscope is depicted in Fig. 3.7. The ultrashort-pulsed Ti:Sapphire laser and the SMF coupler described in Section 3.2.1 are again used in experiments. The laser beam is coupled into port 3 (excitation arm) of the coupler via a Melles Griot 0.25 NA 10× objective  $O_1$ . The fibre is placed in a chuck holder in an  $xyz$  positioner so that the fibre tip could be precisely adjusted at the focus of the objective. Variation of the optical input power coupled to the fibre is achieved using a neutral density filter, ND, placed just before the coupling objective  $O_1$ . The output beam from port 1 (sample arm) of the coupler is collimated by a second Melles Griot objective  $O_2$  (10×/0.25NA) to fill the back aperture of an imaging objective  $O_3$  (Olympus: UplanApo, 40×/0.85NA).

The backscattering SHG signal from a sample is collected by the objective  $O_3$  and

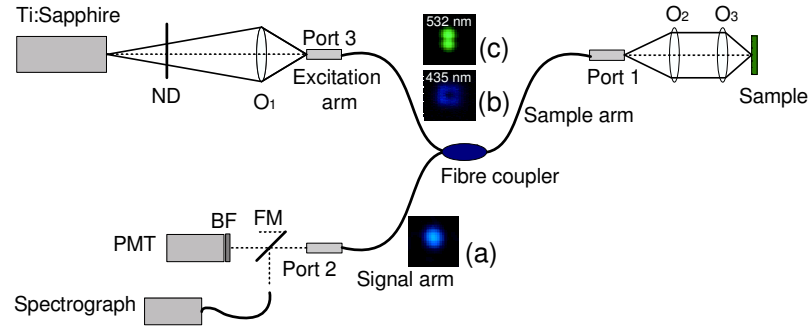


Fig. 3.7: Schematic diagram of the experimental SHG microscope using a single-mode fibre coupler. (a)-(c) Mode profiles in the excitation and signal arms when a visible beam is coupled to port 1.  $O_1$  and  $O_2$ : 0.25 NA 10 $\times$  microscope objectives,  $O_3$ : 0.85 NA 40 $\times$  imaging objective, ND: Neutral density filter, BF: Bandpass filter, FM: flip mirror.

delivered via port 2 (signal arm) of the fibre coupler to a PMT for imaging or a CCD-based fibre-coupled spectrograph (Acton Research Corporation) to collect spectra. An appropriate bandpass filter (BF) is placed in front of the PMT to ensure that only the SHG signal is detected. Switching between imaging and spectra acquisition is obtained by changing the direction of a flip mirror (FM). To further understand the arrangement of the SHG microscope, mode profiles of visible beams guided in the excitation and signal arms are shown again as insets (a)-(c) of Fig. 3.7. In this geometry, the fibre coupler is analogous to a low-pass filter, through which main strength of signals at a visible wavelength propagates to the detector. Furthermore, the fibre tips of the coupler act as pinholes in a conventional confocal arrangement to reduce the multiple scattering of signals.

### 3.3.2 Nonlinear optical spectra

It is clear from the discussion in Sections 2.2.2 and 3.2.2 that emission of SHG is fundamentally different from the TPEF and that its propagation efficiency through the fibre coupler is also slightly different. The ability of the fibre coupler to guide signals over a wide spectral window is of great significance to collect undistorted nonlinear optical images. In this situation, an experimental investigation into the spectra of the emitted nonlinear optical signals through the fibre coupler is required to characterise

the system.

We choose AF-50 dye as a sample to demonstrate the effectiveness of the fibre-optic SHG microscope. This dye, which has extended conjugated pi networks and aromatic heteroatom substitution (inset of Fig. 3.8(a)), possesses large second-order and third-order nonlinear susceptibilities. Therefore, SHG and TPEF can be produced simultaneously. A thin layer of AF-50 dye is produced by evaporation of a mixture of AF-50 dye and isopropyl alcohol on a coverslip and has an average thickness of approximately 250 nm measured by atom force microscopy.

First, AF-50 dye is excited by an ultrafast-pulsed laser beam at wavelength 800 nm. The excitation polarisation emerging from the fibre coupler is parallel to the polarisation of the incident laser. The emission spectrum collected by the spectrograph is shown in Fig. 3.8(a). It is observed that the emission spectrum reveals a sharp SHG peak at 400 nm and a TPEF lobe in the wavelength range from 430 to 600 nm. The bandwidth of the SHG spectrum is approximately 9 nm, which is consistent with the following estimation. For an excitation beam with a Gaussian profile, the full-width at half-maximum (FWHM) of SHG should be  $1/\sqrt{2}$  of the fundamental [16, 17]. Under the experimental condition where the excitation power is approximately 4 mW on the sample, the spectral broadening of pulses arising from SPM is negligible and does not make impact on the bandwidth of the SHG emission spectra. Fig. 3.8(a) also implies that the simultaneous collection of SHG and TPEF signals can be achieved efficiently through the fibre coupler although SHG and TPEF occur at a much shorter wavelength region than the designed operating wavelength of the fibre coupler.

To further confirm the spectral peak generated from the SHG process, we collect the emission spectra while scanning the laser from wavelength 780 to 870 nm. The result shown in Fig. 3.8(b) demonstrates that, for all the excitation wavelengths used, the SHG spectra track with the fundamentals and peak at exactly half the excitation wavelengths. It should be noted that the slight difference of the spectral bandwidth at each excitation wavelength results from the variations of the bandwidth of the laser source over the wide emission window. Additionally, the SHG and TPEF signals vanish

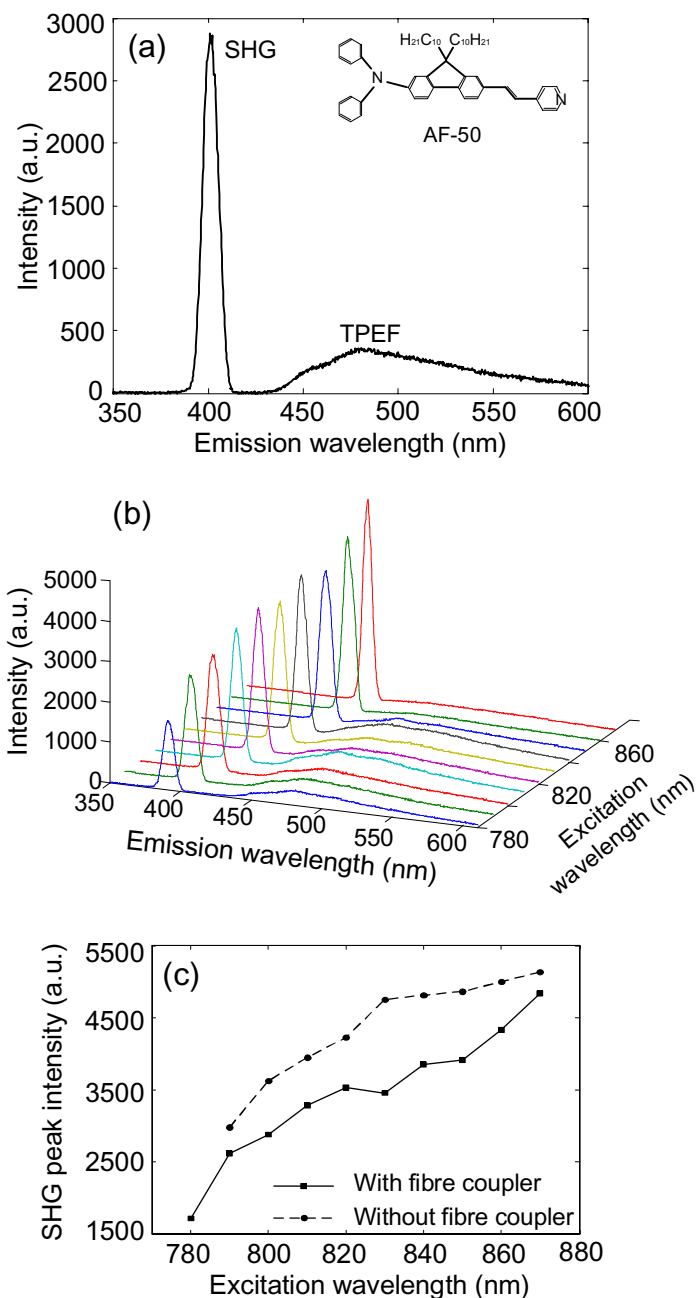


Fig. 3.8: Nonlinear optical spectra in a nonlinear optical microscope using the single-mode fibre coupler. (a) Emission spectrum of AF-50 dye at wavelength 800 nm. (b) Emission spectra as a function of the excitation wavelength over the range of 780 – 870 nm. (c) SHG peak intensity of the spectra as a function of the excitation wavelength with (solid curve) and without (dashed curve) fibre coupler. The excitation power is approximately 4 mW on the sample and the excitation polarisation is parallel to the fundamental laser polarisation.

when the laser is out of mode-locking, indicating that the signals are based on nonlinear optical processes.

It has been reported that an intense laser beam may result in SHG through media having interfaces [19]. To check if the AF-50 dye is the only origination of the SHG signal, SHG spectra is collected again in the wavelength range between 780 and 870 nm without using the fibre coupler. The peak intensity of the SHG spectra is depicted in Fig. 3.8(c) as a function of the excitation wavelength obtained with and without the fibre coupler. The solid curve in the figure is derived from the spectra collected by focusing the output beam from port 2 of the fibre coupler into the spectrograph, while the dashed one is collected directly from the sample without the use of the fibre coupler. The increased SHG peak intensity propagated through the fibre coupler and detected by the spectrograph may arise from the increased SHG cross section of AF-50 and the improved coupling efficiency of the fibre coupler in the visible range that has been discussed in Section 3.2.2. The intensity and variations of the SHG signal shown in Fig. 3.8(c) indicate that the fibre coupler and the coverslip we used does not produce any SHG signal while delivering pulses having an average power of hundreds milliwatt.

### 3.3.3 Nonlinear optical axial response

One of the advantages of TPEF and SHG microscopy is high spatial resolution due to the higher-order dependence of signals on the excitation intensity. To investigate the optical sectioning ability of the fibre-optic nonlinear optical microscope, we measure the axial response of the system to a thin layer of AF-50 dye that has been described in Section 3.3.2. The axial response is obtained by recording the SHG intensity when scanning the sample continuously in the  $z$  direction. The axial position of the sample is driven by a computer-interfaced piezo scanning stage (Physik Instrumente) with a resolution of  $0.1 \mu\text{m}$  and a 6 mm scanning range. Bandpass filters having appropriate central wavelengths with a bandwidth of approximately 9 nm are placed before the PMT to collect the SHG signal.

Typical SHG axial responses to the thin layer at wavelength 800 nm are shown in Fig. 3.9(a), where the input power to port 3 of the fibre coupler is varied in the range of 4 – 12 mW. This set of the axial response curves allows for simultaneous monitoring the SHG efficiency and axial resolution. The FWHM of the axial response curves measured in the SHG microscope, is approximately  $1.8 \mu\text{m}$ . The SHG efficiency of the system can be measured through an observation of the peak intensity of the axial response curves. The peak SHG intensity from each axial response curve in Fig. 3.9(a) is plotted as a function of the input power in Fig. 3.9(b) in a log-log scale. It can be seen that the gradient of the log-log plot is approximately  $2.0 \pm 0.1$ , confirming the second-order nonlinear frequency conversion process.

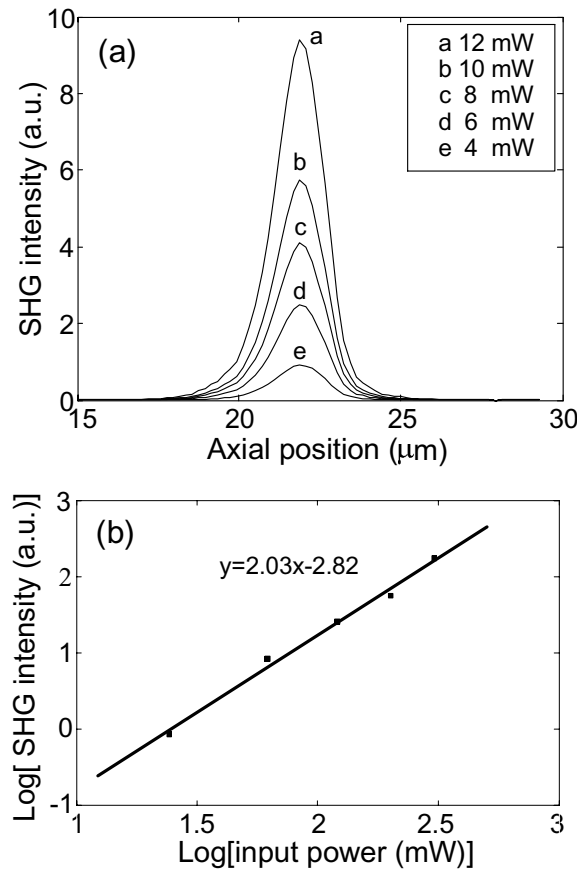


Fig. 3.9: SHG axial response to a thin layer of AF-50 dye at wavelength 800 nm. (a) Axial response curves as a function of the input power to port 3 of the fibre coupler. (b) Quadratic dependence of the SHG peak intensity of axial response curves on the excitation power.

To investigate the resolution performance of the simultaneous SHG and TPEF

collection in the fibre-optic nonlinear optical microscope, we measure the axial responses of the system to the SHG and TPEF by use of the thin layer of AF-50. To record the TPEF axial response, a 510/20 nm bandpass filter is placed before PMT to eliminate the second harmonic and reflected fundamental wavelengths. In Fig. 3.10, the axial responses obtained with the SHG and TPEF signals at an excitation wavelength of 800 nm are depicted. It reveals that the FWHM of SHG and TPEF curves is approximately  $1.8 \mu\text{m}$  and  $2.1 \mu\text{m}$ , respectively, demonstrating that a slight improvement in resolution of approximately 14% for the SHG signal collection is obtained if compared with the TPEF axial response. This feature is due to the fact that the SHG wavelength is shorter than the TPEF wavelength. It should be pointed out that in this effective confocal arrangement, the axial resolution of the SHG microscope using a fibre coupler is improved by approximately 28% compared with that in a fibre-optic TPEF microscope using a large area detector without a pinhole [88].

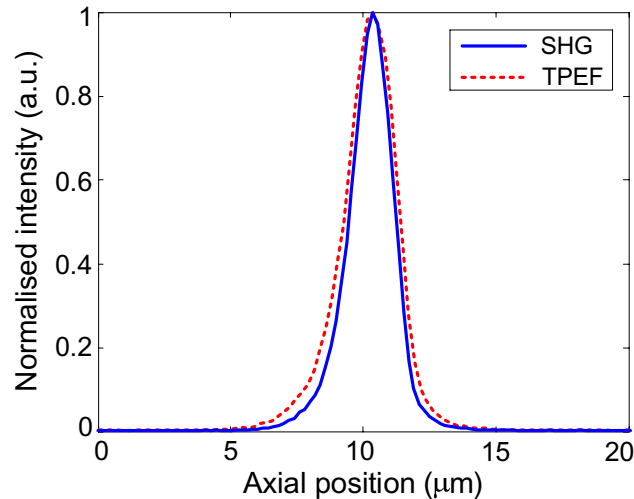


Fig. 3.10: Axial responses to a thin layer of AF-50 dye in a nonlinear optical microscope using a fibre coupler for SHG collection (solid curve) and TPEF collection (dashed curve). The excitation wavelength is 800 nm.

Fig. 3.11 shows the axial resolution performance of the fibre-optic SHG microscope as a function of the excitation wavelength. In this case, the laser is tuned between 800 and 860 nm and corresponding SHG axial responses are recorded. It is shown that the FWHM of the SHG axial responses varies between  $1.8 \mu\text{m}$  and  $1.9 \mu\text{m}$  as the excitation wavelength tunes from 800 to 860 nm. The measurements of axial

resolution as a function of the illumination wavelength shown in Figs. 3.10 and 3.11 are in good agreement with the theoretical prediction based on the normalised fibre spot size parameter. An extensive theoretical investigation into the resolution performance of the SHG microscope using a fibre coupler is presented in Chapter 4.

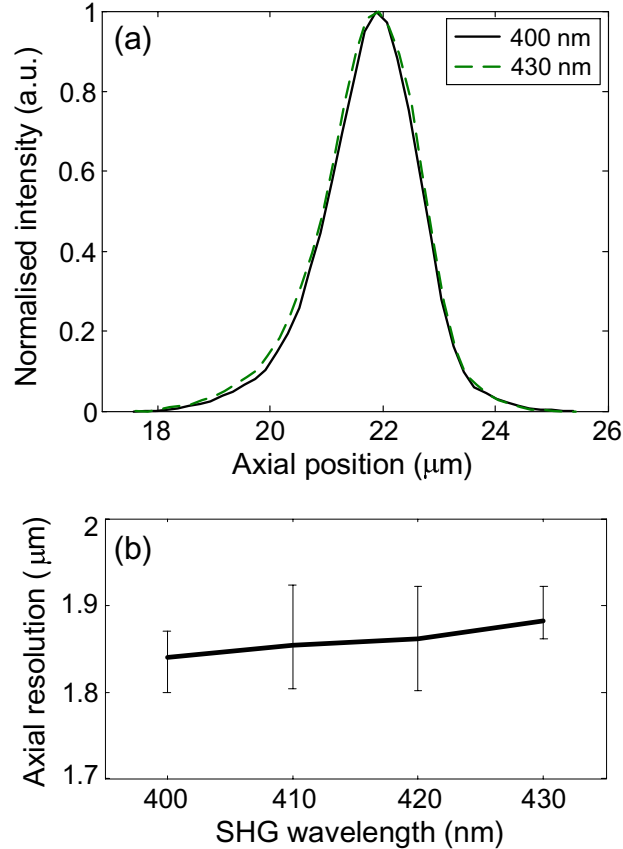


Fig. 3.11: Axial resolution performance of a SHG microscope using a fibre coupler as a function of excitation wavelength. (a) SHG axial responses of the system at excitation wavelengths of 800 nm (solid curve) and 860 nm (dashed curve). (b) SHG axial resolution of the system as a function of detected SHG wavelengths.

### 3.3.4 SHG and TPEF imaging

Achieving high contrast and high spatial resolution is one of the primary goals for optical imaging. Understanding the imaging properties of the fibre-optic nonlinear optical microscope using SHG and TPEF signals can provide stratagem to achieve the best imaging performance based on the two imaging contrast mechanisms. Specifically,



the use of SHG polarisation anisotropy can result in the local structural information that cannot be provided by other optical imaging modalities. To demonstrate the imaging capability and the polarisation sensitivity of the instrument, we measure the SHG and TPEF images of a triangle-shaped sample excited by two beams with parallel and perpendicular polarisation states. As has been demonstrated in Section 3.2.3, linear polarisation of the laser beam is preserved through the fibre coupler. Generally, polarisation anisotropy measurements are made by obtaining images through rotations of the analyser before the detector while maintaining the excitation polarisation. Alternatively, absolute molecular orientations can be determined by rotating the excitation polarisation. The sample consists of a paper sheet ( $75 \text{ g/m}^2$ ) with a mixture of AF-50 dye and isopropyl alcohol. For this bulk sample, rotation of the excitation polarisation is chosen to demonstrate the polarisation anisotropy of SHG imaging and the variation of polarisation direction is achieved by rotating the  $\lambda/4$  plate before the fibre coupler. The sample is scanned two-dimensionally by a scanning stage (Physik Instrumente) with a scanning range of  $200 \mu\text{m}$ .

The SHG and TPEF images are obtained from the same sample site at the same focal plane by using a  $400/9 \text{ nm}$  and a  $510/20 \text{ nm}$  bandpass filters, respectively, as shown in Fig. 3.12. It can be seen that SHG and TPEF images from the same sample produce fundamentally different patterns of contrast. SHG can produce the distribution mapping of  $\chi^{(2)}$  about the local structural organisation, while TPEF can give the distribution mapping of  $\chi^{(3)}$  about molecular distributions. Therefore the combination of simultaneous SHG and TPEF can provide the complementary information shown in the overlay images of SHG and TPEF. A further observation from the SHG images (Figs. 3.12(a) and (d)) shows that SHG images with orthogonal-polarisation excitation display the distinguished appearance, which is due to the fact that the SHG signal arises from electric dipole interaction. Details of the SHG anisotropy measurement of the system will be discussed in the upcoming subsection.

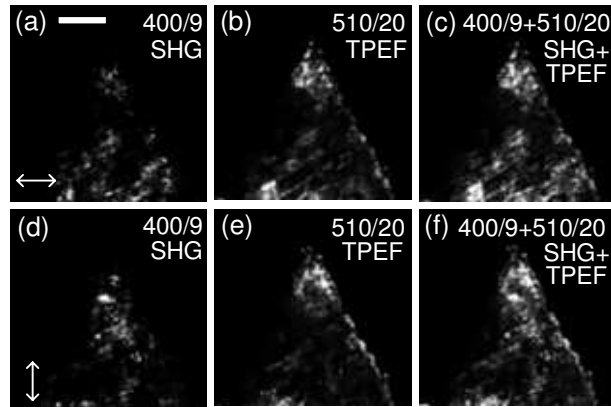


Fig. 3.12: SHG and TPEF images of a triangle-shaped paper sheet excited by parallel polarisation (top) and perpendicular polarisation (bottom) beams at wavelength 800 nm. The excitation power is approximately 4 mW on the sample. SHG images ((a) and (d)) are obtained with a 400/9 nm bandpass filter and TPEF images ((b) and (e)) with a 510/20 nm bandpass filter. Images in (c) and (f) are obtained by overlaying the SHG and TPEF images. Scale bar is 50  $\mu m$ .

### 3.3.5 SHG polarisation anisotropy

As has been described in Sections 2.2.2 and 3.3.4, one of the unique features in SHG microscopy is determination of the molecular orientation by use of polarised SHG signals. To demonstrate the ability of the fibre-optic nonlinear optical microscope to measure the polarisation anisotropy, a standard nonlinear optical crystal, the powder of KTP crystals (Shandong University, China), is used as a sample to give linearly polarised SHG emission with an excitation beam having an arbitrary linear polarisation state.

We first analyse quantitatively the polarisation anisotropy of the KTP crystal powder in a commercial nonlinear laser scanning microscope (Olympus, Fluoview 300, epi-detection). When the laser excitation polarisation is fixed, SHG signals are expected to have parallel polarisation with the laser and therefore should yield a  $\cos^2 \theta$  pattern by rotating the analyser before the PMT. In Fig. 3.13, two SHG images of the KTP crystal powder with orthogonal excitation and the extracted SHG intensity as a function of the analyser rotation angle are well consistent with the prediction based on a  $\cos^2 \theta$  pattern. The deviation of the experimental data from the theoretical

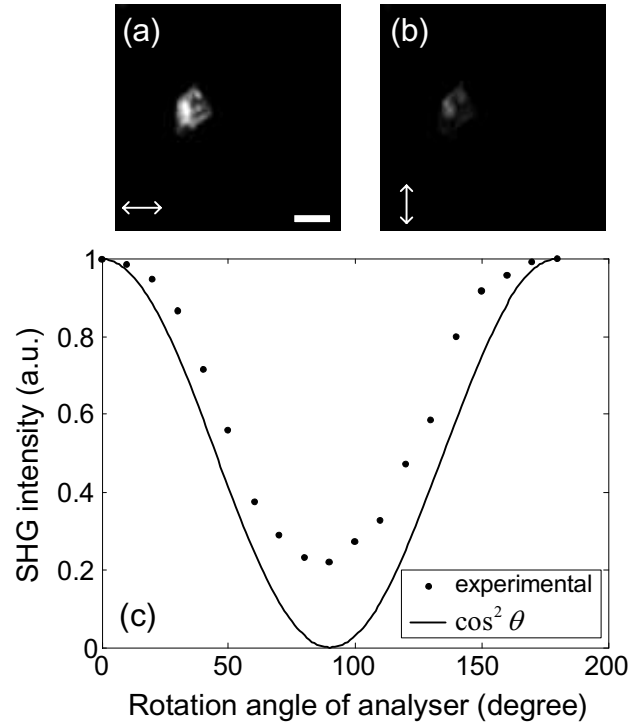


Fig. 3.13: SHG polarisation anisotropy measurement with the KTP crystal powder in a laser scanning microscope. (a)-(b) SHG images obtained with orthogonal polarisation orientations of the analyser. (c) Dependence of the SHG intensity on the rotation angle of the analyser, where the results fit a  $\cos^2 \theta$  function. Scale bar is  $5 \mu m$ .

expectation may arise from the depolarisation effect of galvanometric mirrors and the imaging objective.

The SHG microscope using an SMF coupler exhibits the same manner of SHG polarisation anisotropy of the KTP crystal powder. Fig. 3.14(a) shows a series of SHG images of the KTP crystal powder when the laser with linear polarisation is delivered by the fibre coupler and the analyser is rotated by  $180^\circ$ . Intensity analysis from the SHG images is depicted in Fig. 3.14(b), demonstrating that the SHG intensity varies as a  $\cos^2 \theta$  function. The capability of the system for the polarisation anisotropy measurement is further confirmed by the SHG signals obtained from a fish scale (Fig. 3.15). The fish scale consists of abundance of highly ordered collagen fibrils, which are corresponded to SHG signals. It should be pointed out that although the birefringence axis of the fibre coupler for the excitation wavelength and the SHG

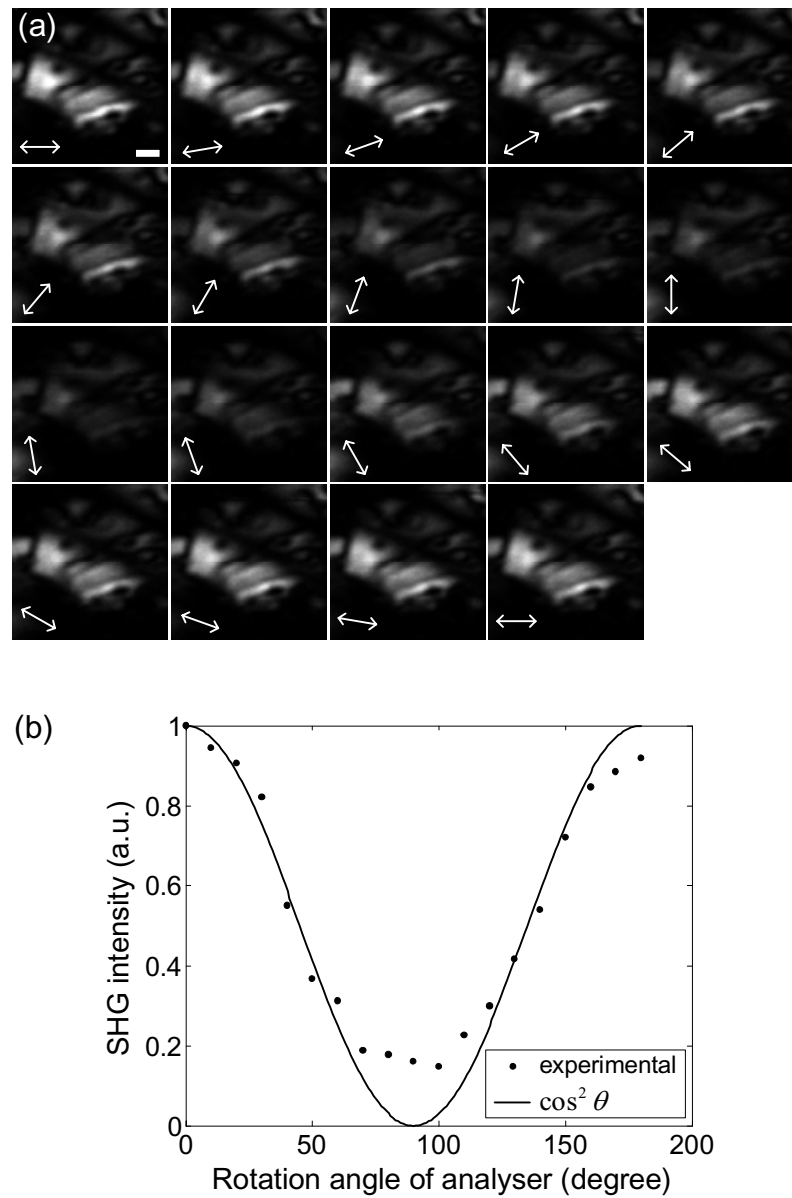


Fig. 3.14: SHG polarisation anisotropy measurement with the KTP crystal powder in SHG microscopy using a single-mode fibre coupler. (a) A set of SHG images of the KTP crystal powder obtained by rotating the analyser. (b) Dependence of SHG intensity on the rotation angle of the analyser, where the results fit a  $\cos^2 \theta$  function. Scale bar is  $5 \mu\text{m}$ .

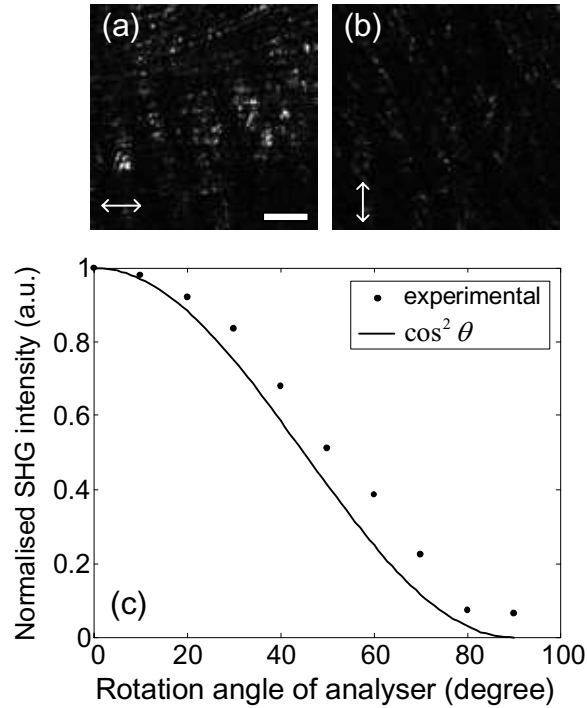


Fig. 3.15: SHG polarisation anisotropy measurement with a fish scale in SHG microscopy using a single-mode fibre coupler. (a),(b) SHG images obtained with orthogonal polarisation orientations of analyser. (c) Dependence of SHG intensity on the rotation angle of the analyser, where the results fit a  $\cos^2 \theta$  function. Scale bar is  $20 \mu\text{m}$ .

wavelength might not be identical, the microscopy system based on the SMF coupler shows the powerful capability to probe local molecular orientations by use of the SHG polarisation anisotropy.

### 3.4 Characterisation of the GRIN lens-fibre spacing

The fibre-optic nonlinear optical microscope presented in Section 3.3 has used an SMF coupler to replace major bulk optical components for illumination delivery and signal collection. To achieve a further compact and miniature microscope such as an endoscope, GRIN lenses are usually integrated into the imaging system to replace the bulk imaging objective (see Section 2.3.3). Our previous study has demonstrated the

feasibility of a fibre-optic two-photon endoscope based on an SMF coupler, a GRIN rod lens, and a microprism [27].

When a GRIN lens is integrated into the fibre-optic system, the location of the focal point of a GRIN rod lens can be set by adjusting the magnitude of the gap between a source and the entrance face of the GRIN rod lens. Consequently, the NA of a GRIN rod lens is effectively changed as the gap between a light source and a GRIN lens varies [135]. Such an effective change in NA of a GRIN rod lens can affect the performance of fibre-optic nonlinear optical endoscopy in three aspects. The first aspect is imaging resolution that depends on the square of the effective NA [136], the second one is the illumination and collection efficiency that shows a complicated dependence on the effective NA, and the third one is the SHG and TPEF strength that depends on the fourth power of the effective NA [137]. Therefore, a signal optimisation of fibre-optic nonlinear optical endoscopy becomes possible and is thus necessary because nonlinear optical signals from biological tissues are usually weak.

In such a situation, it is of significance to experimentally investigate the impact of the GRIN lens-fibre spacing on the signal level of fibre-optic nonlinear optical microscopy. In particular, this effect in a system based on GRIN lenses having different pitch lengths is of importance for practical imaging applications.

### **3.4.1 Experimental arrangement**

A schematic diagram of the fibre-optic nonlinear optical microscope based on a fibre coupler and a GRIN lens is depicted in Fig. 3.16. The arrangement is similar to the system shown in Fig. 3.7, except for the following modifications: The output beam from port 1 of the coupler crosses the gap and is focused by the GRIN rod lens. The fluorescence emitted from the sample is recollected by the GRIN rod lens and delivered via port 2 of the coupler into a photomultiplier tube masked with a  $510 \pm 20$  nm bandpass filter (BF). It should be noticed that the signal level and axial resolution performance of the nonlinear optical microscopy system using a fibre and a

GRIN lens is strongly dependent on the gap length between the GRIN lens and fibre. Therefore, to simplify the experiment, only TPEF from AF-50 dye is used throughout the investigation in Section 3.4.

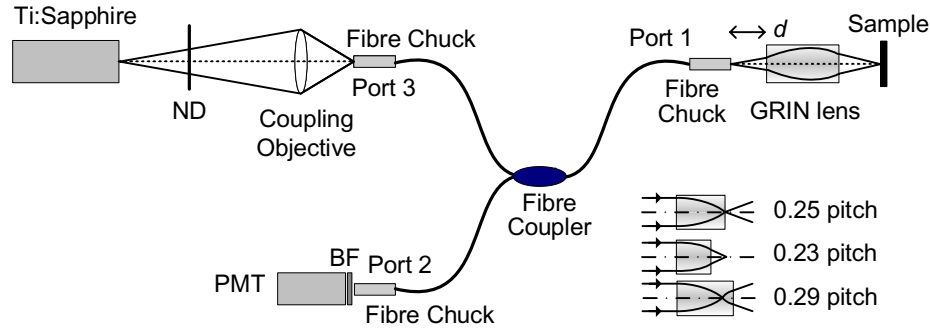


Fig. 3.16: Schematic diagram of the fibre-optic nonlinear optical microscope based on a single-mode fibre coupler and a GRIN rod lens.

Three GRIN rod lenses of pitches 0.25, 0.23 and 0.29 (Newport) are chosen to confirm and compare the signal optimisation condition in fibre-optic TPEF microscopy. The difference of the pitch length implies that the focal position of the three GRIN rod lenses is at the surface of the lens, inside the lens and outside the lens, respectively, if a collimated beam is used (see Fig. 3.16). The 1.8-mm-diameter plano-plano GRIN lenses are designed for a wavelength of 830 nm. The 0.25 pitch GRIN lens has an NA of 0.6, while the NA of the 0.23 pitch and 0.29 pitch GRIN lenses is 0.46. The magnitude of the gap between the fibre coupler end and a GRIN lens,  $d$ , is controlled by a one-dimensional translation stage having a resolution of  $10 \mu\text{m}$ . The maximum length of the gap is 5.5 mm to overfill the entrance face of the GRIN rod lens. The thin layer of AF-50 dye is driven by a scanning stage that has been used in experiments presented in Section 3.3.

### 3.4.2 Determination of the effective numerical aperture

To achieve the effective NA of a GRIN rod lens, the axial response of the system to a plane mirror is recorded by continuous scanning in the  $z$  direction. The measurement of the FWHM of the axial response curve allows for the analysis of axial resolution of

the system  $\Delta z$ , and then the effective NA of the GRIN rod lens ( $\sin \alpha$ ) can be derived from [136]

$$u = (8\pi/\lambda)\Delta z \sin^2(\alpha/2) , \quad (3.1)$$

where  $u$  is an axial optical coordinate and  $\lambda$  is the wavelength of the illumination light. By varying the gap length  $d$ , a set of axial response curves is obtained. The dependence of the FWHM of the axial response and the effective NA on the gap length for the three given GRIN rod lenses is depicted in Fig. 3.17(a). It is shown that the FWHM of the axial response drops rapidly to approximately 13.6, 11, and 13  $\mu m$ , respectively, as the gap length increases. The decrease in the FWHM indicates the improvement in axial resolution and therefore the enhancement of the effective NA of the GRIN lens. The effective NA of the GRIN lens can be calculated based on Eq. 3.1, when the half width at half maximum of the axial response is measured and  $u$  is 5.1 for the case of confocal TPEF microscopy [136]. The effective NA reflects on the system NA that combines the excitation and emission NA. As expected, for all the GRIN rod lenses, the effective NA increases gradually and tends towards a limit (approximately 0.29, 0.31, and 0.28, respectively) when the gap increases until the output laser beam from the fibre coupler overfills the entrance face of the GRIN rod lens.

In addition, analysis of the peak intensity of the axial responses reveals a decrease in the coupling efficiency of the system approximately by 71%, 81%, and 69%, respectively, as shown in Fig. 3.17(b). Such a signal reduction is caused by two physical processes. The first process is the coupling of illumination into a GRIN rod lens, which is confirmed by the transmitted power after the GRIN lens (Fig. 3.17(b)). In all cases, the transmission efficiency for the input power exhibits a slight degradation of approximately 6.3%, 10%, and 6.3%, respectively, as a result of increasing the gap length  $d$  in the range between 0.25 and 5.5 mm. The second process is related to the mismatching between the fibre mode profile and the field distribution of the reflected signal on the end of the coupler. Once the fibre mode profile and the field distribution do not match each other, a significant decrease of collection efficiency will occur [138]. It should be noted that the experimental results of the coupling efficiency



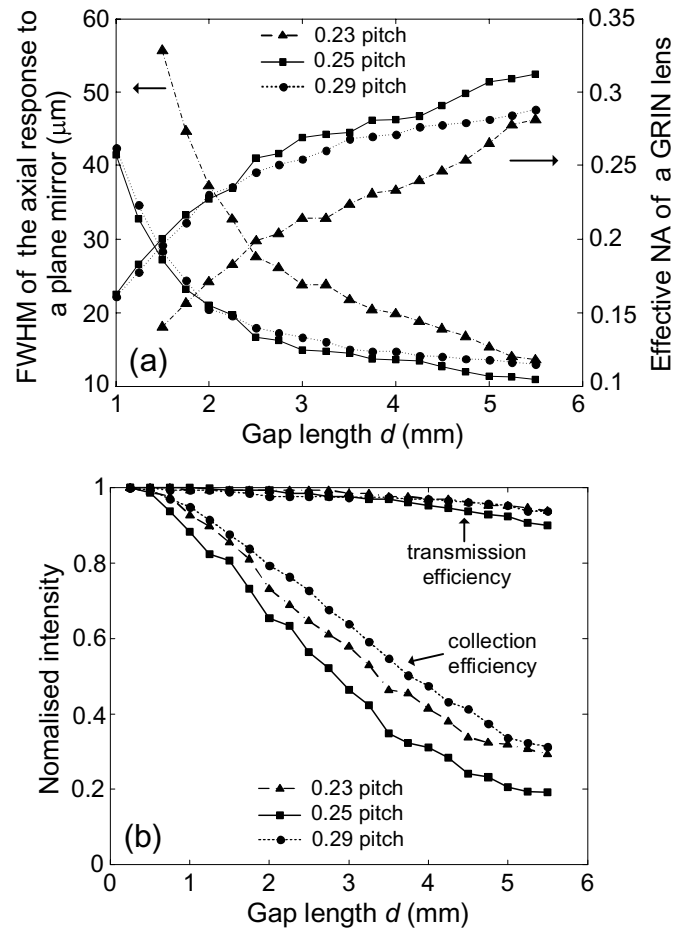


Fig. 3.17: One photon reflection confocal axial response. (a) FWHM of the axial response to a plane mirror and effective NA of the GRIN rod lens as a function of the gap  $d$ . (b) Transmission efficiency of the GRIN lens and peak intensity of the axial response to a plane mirror as a function of the gap  $d$ .

in Fig. 3.17(b) agree with the theoretical calculation of signal level in reflection-mode fibre-optic confocal scanning microscopy in the sense that the maximum reflected signal is achieved when the distance between the fibre and the GRIN lens is small [138].

### 3.4.3 Optimisation of the nonlinear optical signal

To study the nonlinear signal level in the fibre-optic nonlinear optical microscope, a set of TPEF axial responses to the thin layer of AF-50 is obtained. The FWHM of the axial response as a function of the gap length for the three GRIN rod lenses is plotted

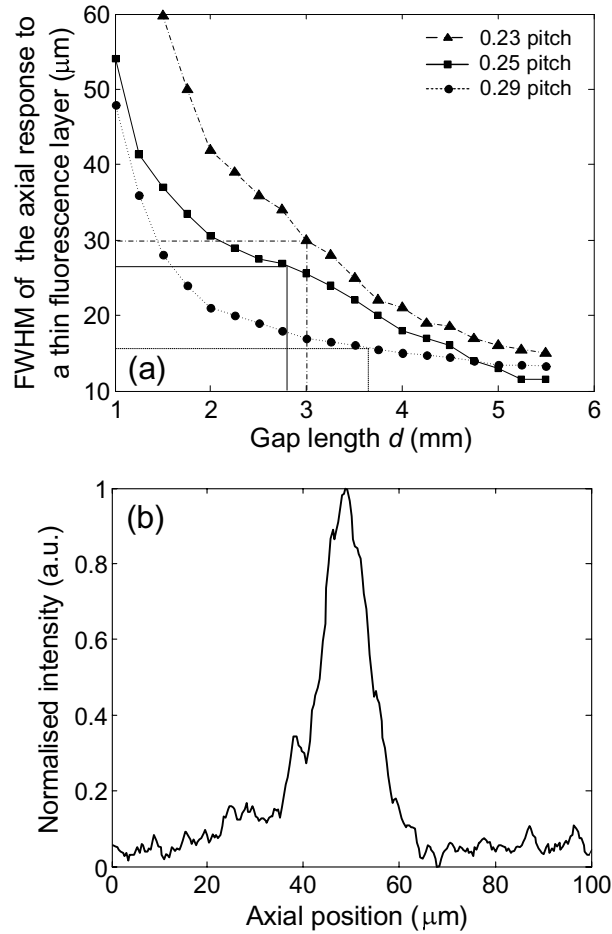


Fig. 3.18: (a) FWHM of the TPEF axial response to a thin layer of AF-50 as a function of gap  $d$ . (b) A TPEF axial response when  $d$  is 5 mm to optimise the axial resolution of the fibre-optic nonlinear optical microscope using a 0.25 pitch GRIN lens.

in Fig. 3.18(a), where the feature of the improvement in axial resolution is observed. It notes that axial resolution of TPEF imaging is 15, 11.6, and 13.3  $\mu\text{m}$  for 0.23, 0.25 and 0.29 pitch GRIN rod lenses, respectively, when the gap length is 5.5 mm. To further understand the axial performance of the system, a particular axial response corresponding to the highest resolution using the 0.25 pitch GRIN lens is presented in Fig. 3.18(b). In this case, the gap length is maximised to fulfill the back surface of the GRIN lens to achieve an optimised axial resolution of 11.6  $\mu\text{m}$ .

Fig. 3.19 shows the peak TPEF intensity of the axial response as a function of gap lengths for the three GRIN lenses. It is clear that the maximum fluorescence intensity is collected by the fibre coupler over the gap length between 0.25 mm and 5.5 mm in

all cases. Further observation from Fig. 3.19 reveals that the maximum fluorescence signal appears at gap lengths of approximately 2, 1.25, and 1.75 mm for the three GRIN lenses. The appearance of the maximum two-photon signal results from two competing physical processes. On the one hand, increasing the effective NA leads to the enhancement of the TPEF signal because the two-photon excitation probability is proportional to the fourth power of the effective NA [137]. On the other hand, as suggested in Fig. 3.17(b), the illumination and collection efficiency of the imaging system drops as the effective NA increases. Therefore, although the emitted TPEF signal increases as the gap length enlarges, the TPEF signal coupled backward by the fibre eventually reduces, as shown in Fig. 3.19.

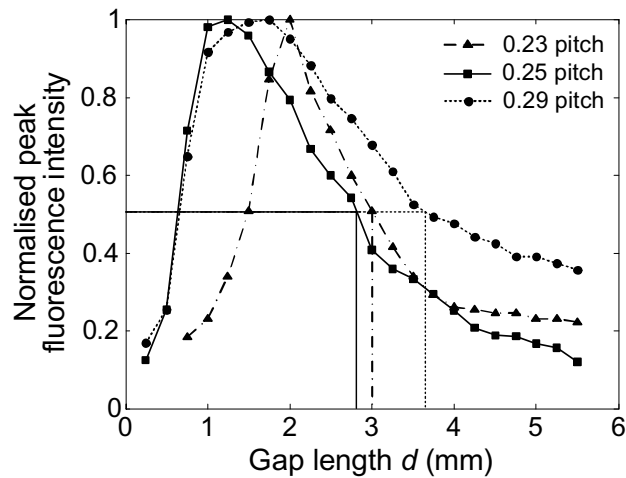


Fig. 3.19: Peak intensity of the fluorescence axial response as a function of gap  $d$  in a fibre-optic nonlinear optical microscope.

The combination of Figs. 3.18(a) and 3.19 implies that there is a trade-off between TPEF axial resolution of the system and the TPEF signal level that is related to the parameters of the GRIN lens. At the maximum signal level, the corresponding axial resolution is 42.0, 38.5, and 24.0  $\mu\text{m}$ , respectively, for 0.23, 0.25 and 0.29 pitch GRIN rod lenses. Consider the gap length at which the TPEF signal level drops to 50% of the maximum (see Fig. 3.19), the axial resolution corresponding to the three GRIN rod lenses is approximately 30.0, 26.0, and 15.7  $\mu\text{m}$  (Fig. 3.18(a)). Table 3.1 summarises the effective NA, optimised axial resolution, and axial resolution at the

maximum fluorescence intensity, etc., which should be considered in applications of TPEF endoscopy. In addition, the appearance of the maximum signal level when the gap length increases can be understood from the transfer function analysis, which will be presented in Section 4.4.3.

GRIN lens pitch at 830 nm	Maximum NA	Effective confocal NA	Optimised confocal $\Delta z$ ( $\mu\text{m}$ )	Optimised TPEF $\Delta z$ ( $\mu\text{m}$ )	TPEF $\Delta z$ at half maximum intensity ( $\mu\text{m}$ )	TPEF $\Delta z$ at maximum intensity ( $\mu\text{m}$ )	$d$ at maximum intensity (mm)
0.23	0.46	0.29	13.6	15	30	42	2
0.25	0.6	0.31	11	11.6*	26	38.5*	1.25
0.29	0.46	0.28	13	13.3	15.7	24	1.75

Table 3.1: Characterisation of the GRIN lens-fibre spacing in a fibre-optic nonlinear optical microscope. \* These axial resolution values are applied in Fig. 3.20 with  $10 \mu\text{m}$  beads imaging.

### 3.4.4 Two-photon fluorescence imaging

To show the optimum imaging performance of the fibre-optic TPEF microscope, two image sets of  $10 \mu\text{m}$  fluorescence polymer microspheres (Polysciences, Fluoresbrite) shown in Fig. 3.20 are obtained with the 0.25 pitch GRIN rod lens when the gap between the fibre coupler end and the GRIN rod lens is 1.25 mm and 5.5 mm, respectively. The

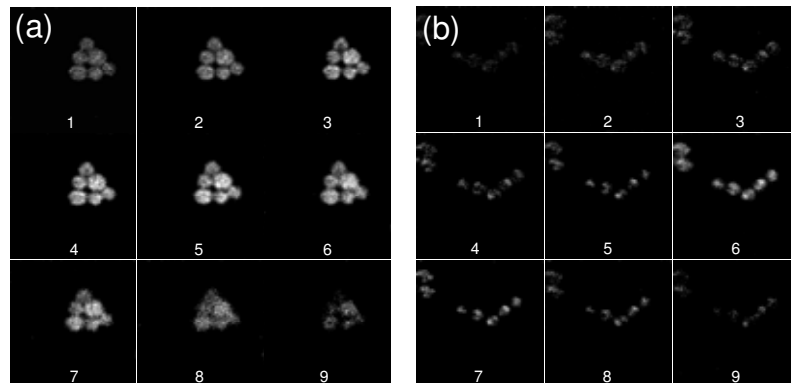


Fig. 3.20: A series of  $xy$  images of  $10 \mu\text{m}$  fluorescence polymer microspheres acquired with a single-mode fibre coupler and a 0.25 pitch GRIN lens by (a) setting  $d = 1.25$  mm, with a slice spacing of  $15 \mu\text{m}$  and (b) setting  $d = 5.5$  mm, with a slice spacing of  $5 \mu\text{m}$ . Axial resolution for these two gap lengths are shown in Table 3.1. Each slice size is  $100 \mu\text{m} \times 100 \mu\text{m}$ . The average power on the sample is 10 mW.

two image sets are recorded with the lateral size of  $100\ \mu\text{m}$  and the slice spacing of  $15$  and  $5\ \mu\text{m}$ , respectively. It is clearly observable that the TPEF images have strong intensity but poor axial resolution with the gap where the optimisation of the signal level is achieved (Fig. 3.20(a)). On the other hand, the optical sectioning ability of the system is optimised with a low signal level when the gap length is at maximum (Fig. 3.20(b)).

### 3.5 Chapter conclusions

This chapter has demonstrated the construction and characterisation of a nonlinear optical microscope that uses an SMF coupler. Simultaneous TPEF and SHG imaging has been efficiently achieved through the SMF coupler. In addition, a GRIN lens has been integrated into the system using an SMF coupler. An intrinsic trade-off between signal level and axial resolution has been observed and investigated in such a system.

The polarisation characterisation of femtosecond pulsed and CW beams propagating through the fibre coupler has demonstrated that the linear polarisation states of pulsed and CW illumination over the broad wavelength range can be preserved in a conventional fused fibre coupler. The degree of polarisation of approximately one is obtained at an angular interval of approximately 90 degrees of the incident polarisation angle. Furthermore, the fibre coupler acts as a low-pass spectral filter in the visible wavelength range with a splitting ratio between 99.6/0.4 and 99.7/0.3, exhibiting an ideal feature desirable for nonlinear optical microscopy.

The nonlinear optical microscope based on an SMF coupler enables the delivery of ultrashort-pulsed laser in the near infrared wavelength range as well as the collection of TPEF and SHG in the visible wavelength range. The system exhibits the axial resolution of  $1.8\ \mu\text{m}$  for SHG imaging, showing a slight enhancement of the optical sectioning effect compared with TPEF imaging using the same excitation wavelength. In particular, based on the polarisation characteristics of the fibre coupler, the fibre-

optic SHG microscope enables the polarisation anisotropy measurement, which cannot be provided by TPEF microscopy alone and can be potentially used to analyse the molecular orientations of structural proteins.

The integration of a GRIN lens into the fibre-optic nonlinear optical microscope is of significance toward the application in nonlinear optical endoscopy. We have demonstrated that the fluorescence signal level and axial resolution are functions of the gap length between the fibre coupler end and the GRIN lens in a fibre-optic nonlinear optical microscope. The collected TPEF intensity exhibits a maximum value as the gap between the fibre coupler end and the GRIN rod lens enlarges, i.e. as the effective NA of a GRIN lens increases. These results elucidate choices in the signal to resolution trade-off in the applications of fibre-optic nonlinear optical endoscopy to achieve the optimised visualisation of biological tissue.

Such a compact system using multiple nonlinear optical imaging modalities may make nonlinear optical endoscopy possible for *in vivo* medical applications, if a scanning mechanism is introduced and the signal level is improved, which will be explored in Chapter 5.

# Chapter 4

## Three-dimensional image formation in fibre-optic second harmonic generation microscopy

### 4.1 Introduction

In the fibre-optic systems described in Chapters 3, two-photon excited fluorescence (TPEF) and second harmonic generation (SHG) have been achieved using the nonlinear optical effects in a reflection confocal mode, where the fibre tips act as a finite-sized confocal pinhole. Consequently, the investigation into image formation of the fibre-optic nonlinear optical microscope is required to study and understand the effect of system parameters on the performance of the microscope. The transfer function is typically used to describe an imaging system by giving the transmission efficiency of each periodic component with different spatial frequencies. The concept of the transfer function can be generalised to include variations in three dimensions to characterise image formation in confocal scanning microscopy and nonlinear optical microscopy [136, 139–142]. The description of imaging using three-dimensional (3D) transfer functions is a generalised method for completely imaging of any object, if

scattering is weak enough that the first Born approximation holds [136, 139].

Physically, TPEF and SHG microscopy correspond to incoherent and coherent imaging processes, which can be understood by an optical transfer function (OTF) and a coherent transfer function (CTF), respectively [136, 139]. Gu and Sheppard have developed a 3D OTF to evaluate the performance of fibre-optic single-photon fluorescence microscopy [136, 139]. Subsequently, Gu and Bird have extended this method to analyse image formation of fibre-optic TPEF microscopy using single-mode fibres (SMFs) [141]. It has shown that, since the fibre tips are used as the illumination source and the pinhole for signal collection, the transfer function performance under two-photon excitation is significantly dependent on the fibre parameters. The use of a fibre coupler leads to an improvement in axial resolution compared with the fibre-optic TPEF system with a single illumination fibre and a large-area detector [88, 89]. Furthermore, the 3D OTF for fibre-optic TPEF microscopy is always positive, which means that image artifacts that may occur in a TPEF microscope with a finite-sized detector can be avoided. However, the 3D OTF is the 3D Fourier transform of the effective intensity point spread function (PSF), representing intensity variations of each spatial frequency component of the object in incoherent imaging systems. As a result, the 3D OTF for fibre-optic TPEF microscopy is not applicable to fibre-optic SHG microscopy where amplitude variations of the object transmission function in coherent imaging systems should be described by the CTF.

Investigations into the performance of the CTF for a fibre-optic confocal scanning microscope for a non-fluorescent object have been conducted [140, 143]. It has been found that the utilisation of optical fibres does not affect the bandpass of spatial frequencies, but reduces the strength of the CTF, particularly along the axial direction. More importantly, fibre-optic scanning microscopy in the case of a non-fluorescent object exhibits the purely coherent imaging nature even for finite values of the fibre spot size, because a fibre is a waveguide that can coherently respond to the amplitude and the phase of the guided light. As a result, fibre-optic non-fluorescent microscopy can be described by a 3D CTF that can be expressed by an analytical expression.



However, the previous studies of the 3D CTF are achieved through fibre-optic systems for linear optical imaging. Therefore, the development of the CTF for fibre-optic SHG microscopy is essential to study the transfer function performance in the case of the second-order optical process.

The study of transfer function performance in this chapter is focused on the geometry of SHG microscopy using an SMF coupler described in Chapter 3. The aim of this chapter is to understand 3D image formation in fibre-optic SHG microscopy using the concept of the 3D CTF and to reveal the dependence of axial resolution and signal level on fibre coupling parameters. The chapter is organised into five sections beginning with this introduction section. In Section 4.2, 3D image formation is derived for the case of SHG and in Section 4.3, the 3D CTF for fibre-optic SHG microscopy is formalised. Numerical results and discussion on axial resolution and signal level are presented in Section 4.4. In particular, the effect of the fibre spot size on the 3D CTF is investigated numerically and experimentally. The chapter conclusions are summarised in Section 4.5.

## 4.2 Three-dimensional image formation

In order to investigate the effect of optical fibres on illumination and collection separately, let us consider the schematic diagram of a fibre-optic SHG microscope as shown in Fig. 4.1 [144]. Two optical SMFs  $F_1$  and  $F_2$  are used to deliver illumination at wavelength  $2\lambda_0$  and collect SHG signal at wavelength  $\lambda_0$ , respectively. When the illumination optical fibre  $F_1$  and the collection optical fibre  $F_2$  are identical, the performance of the system is equivalent to that using a fibre coupler [26, 27, 129].

As SHG is a coherent process, the analysis of image formation in fibre-optic SHG microscopy is similar to that in fibre-optic non-fluorescence microscopy [143]. Although both non-fluorescence and SHG imaging modes are incoherent, the fundamental difference between them is that the electrical field of the SHG emission from a sample

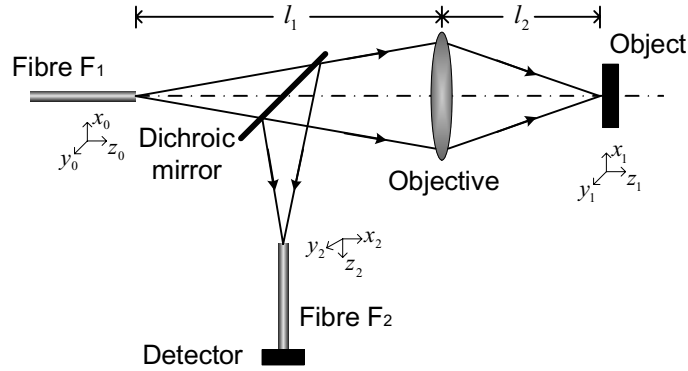


Fig. 4.1: Schematic diagram of the fiber-optic SHG scanning microscope.

is proportional to the square of the illumination field on the sample, while the field in non-fluorescent microscopy is directly proportional to the illumination field. According to the analysis of fibre-optic confocal scanning microscopy [143], the image intensity from a scan point  $\mathbf{r}_s = (x_s, y_s, z_s)$  in fibre-optic SHG microscopy can be expressed, if the optical axis is assumed along the  $z$  direction, as

$$I(\mathbf{r}_s) = \left| \int_{-\infty}^{\infty} U_2^*(x_2, y_2) \delta(z_2) \left[ \int_{-\infty}^{\infty} U_1(x_0, y_0) \delta(z_0) \exp[ik(z_0 - z_1)] h_1(\mathbf{r}_0 + \mathbf{M}_1 \mathbf{r}_1) d\mathbf{r}_0 \right]^2 \varepsilon(\mathbf{r}_s - \mathbf{r}_1) \exp[ik(\pm z_1 - z_2)] h_2(\mathbf{r}_1 + \mathbf{M}_2 \mathbf{r}_2) d\mathbf{r}_2 d\mathbf{r}_1 \right|^2, \quad (4.1)$$

where the term in the first square brackets results from the quadratic dependence of SHG.  $\mathbf{r}_0 = (x_0, y_0, z_0)$ ,  $\mathbf{r}_1 = (x_1, y_1, z_1)$ , and  $\mathbf{r}_2 = (x_2, y_2, z_2)$  represent the positions in the illumination, object and collection spaces, respectively.  $U_1(x, y)$  and  $U_2(x, y)$  are the amplitude mode profiles on the output end of fibre  $F_1$  and on the input end of fibre  $F_2$ , respectively.  $*$  denotes the conjugate operation and the parameters  $\mathbf{M}_1$  and  $\mathbf{M}_2$  are diagonal matrices of the magnification factors of the illumination and collection lenses, respectively [136].  $\varepsilon(r)$  is the object function representing the SHG strength of the object.  $h_1(\mathbf{r})$  and  $h_2(\mathbf{r})$  are the 3D amplitude PSFs for the objective lenses in

illumination and collection paths, given by [136]

$$h_n(x, y, z) = \int \int P_n(\xi, \eta, z) \exp[-j2\pi(\xi x + \eta y)] d\xi d\eta , \quad (4.2)$$

where  $P_n(\xi, \eta, z)$  is the defocused pupil functions of the objective lens and  $n$  is an integer such that  $n = 1, 2$ .

Using the 3D convolution relation, one can simplify Eq. 4.1 as

$$I(\mathbf{r}_s) = \left| h_{eff}(\mathbf{r}_s) \otimes_3 \varepsilon(\mathbf{r}_s) \right|^2 , \quad (4.3)$$

where  $\otimes_3$  denotes the 3D convolution operation.  $h_{eff}$  is the 3D effective PSF for fibre-optic SHG microscopy and given by

$$h_{eff}(\mathbf{r}) = \left[ U_1(\mathbf{M}_1 x, \mathbf{M}_1 y) \otimes_2 h_1(\mathbf{M}_1 r) \right]^2 \left[ U_2^*(\mathbf{M}_1 x, \mathbf{M}_1 y) \otimes_2 h_2(\mathbf{r}) \right] . \quad (4.4)$$

Here  $\otimes_2$  denotes the 2D convolution operation.

### 4.3 Three-dimensional coherent transfer function

Eqs. 4.1 and 4.3 represent a superposition of the light amplitude from a sample and therefore imply that, like fibre-optic non-fluorescence microscopy, fibre-optic SHG microscopy is purely coherent. This feature is of particular importance when one performs SHG interferometric microscopy/tomography [145]. Therefore, fibre-optic SHG microscopy can be analysed in terms of the 3D CTF that is given by the 3D Fourier transform of the effective PSF [136]. The CTF gives the transmission efficiency of each amplitude periodic component in a coherent imaging system. The 3D CTF,  $c(\mathbf{m})$ , for fibre-optic SHG microscopy can thus be described by

$$c(\mathbf{m}) = c_1(\mathbf{m}) \otimes_3 c_2(\mathbf{m}) , \quad (4.5)$$

where

$$c_1(\mathbf{m}) = F_3 \left\{ [U_1(\mathbf{M}_1 x, \mathbf{M}_1 y) \otimes_2 h_1(\mathbf{M}_1 r)]^2 \right\} , \quad (4.6)$$

and

$$c_2(\mathbf{m}) = F_3 \left\{ [U_2^*(\mathbf{M}_1 x, \mathbf{M}_1 y) \otimes_2 h_2(\mathbf{r})] \right\} . \quad (4.7)$$

Here  $F_3$  is the 3D Fourier transform with respect to  $\mathbf{r}_s$  and  $\mathbf{m}$  represents the spatial frequency vector with two transverse components  $m$  and  $n$ , and one axial component  $s$ . For a system using a circular lens, Eq. 4.6 is the 3D CTF for a fibre-optic reflection-mode non-fluorescence microscope with wavelength  $2\lambda_0$  [143]. Suppose that both illumination and collection fibres are SMFs with mode spot radii  $a_1$  and  $a_2$  and that the Gaussian approximation holds for the fibre. Further assume that the paraxial approximation is used and the objective has circular aperture of radius  $a$ . Therefore, the analytical expression for  $c_1(\mathbf{m})$  can be derived as [143, 144]:

$$c_1(l, s) = \exp(-2A_1 s) \begin{cases} 1, & l^2/2 \leq s \leq 1/2 - l(1-l), \\ (2/\pi) \sin^{-1} \left\{ (1-2s)/[2l(2s-l^2)^{1/2}] \right\}, & 1/2 - l(1-l) \leq s \leq 1/2, \\ 0, & \textit{otherwise.} \end{cases} \quad (4.8)$$

Similarly, Eq. 4.7 represents the 3D CTF for a single circular lens with wavelength  $\lambda_0$  and weighted by the Fourier transform of the fibre mode profile  $U_2^*(x, y)$ , given by [143, 144]

$$c_2(l, s) = \exp(-A_2 l^2/2) \delta(s - l^2/2) , \quad (4.9)$$

where

$$A_j = \left[ 2\pi a a_j / (\lambda_j d) \right]^2 \quad (4.10)$$

is the normalised fibre spot size for illumination and collection fibres ( $j = 1, 2$ ) [136].  $d$  is the distance between the fibre ends and the objective. As has been mentioned above, the wavelength in illumination and collection fibres are  $\lambda_1 = 2\lambda_0$  and  $\lambda_2 = \lambda_0$ , respectively. The variables  $l$  ( $l = \sqrt{m^2 + n^2}$ ) and  $s$  denote the radial and axial spatial frequencies normalised by  $\sin \alpha / \lambda_0$  and  $4 \sin^2(\alpha/2) / \lambda_0$ , respectively, where  $\sin \alpha$  is the numerical aperture (NA) of the objective.

According to Eq. 4.5, the 3D CTF can be numerically evaluated, if the delta function in Eq. 4.9 is taken into account, by

$$\begin{aligned} c(l, s) &= \int \int \int \exp\left[\frac{-A_2(m^2 + n^2)}{2}\right] \delta\left(s' - \frac{m^2 + n^2}{2}\right) c_1\left(\sqrt{(m-l)^2 + n^2}, s-s'\right) dm dn ds' \\ &= \int \int_{\sigma} \exp\left[\frac{-A_2(m^2 + n^2)}{2}\right] c_1\left(\sqrt{(m-l)^2 + n^2}, s - \frac{m^2 + n^2}{2}\right) dm dn, \quad (4.11) \end{aligned}$$

where  $\sigma$  represents the area overlapped by  $m^2 + n^2 = 1$  and  $(m-l)^2 + n^2 = 1$  as shown in Fig. 4.2. Finally, 3D CTF for fibre-optic SHG microscopy can be explicitly written as

$$\begin{aligned} c(l, s) &= \int_0^{\sqrt{1-(l/2)^2}} \left[ \int_{l-\sqrt{1-n^2}}^{\sqrt{1-n^2}} \exp\left[\frac{-A_2(m^2 + n^2)}{2}\right] \right. \\ &\quad \left. c_1\left(\sqrt{(m-l)^2 + n^2}, s - \frac{m^2 + n^2}{2}\right) dm \right] dn. \quad (4.12) \end{aligned}$$

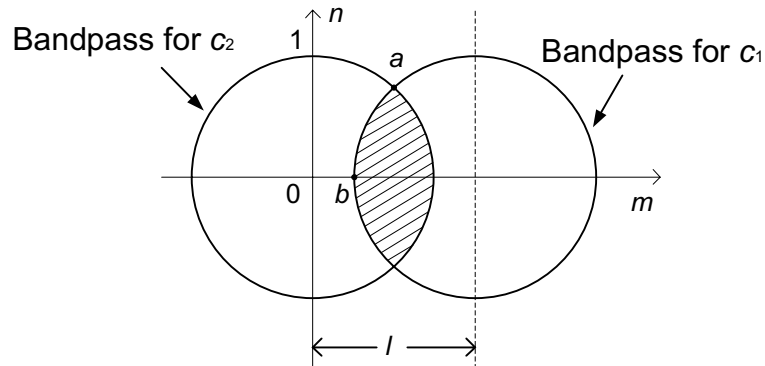


Fig. 4.2: 2D convolution based on Eq. 4.11. The highlighted region is the overlapped area where the integration in Eq.4.11 is performed. The coordinators for a and b are  $(l/2, \sqrt{1-(l/2)^2})$  and  $(l - \sqrt{1-n^2}, 0)$ , respectively.

It should be pointed out that the 3D CTF for fibre-optic SHG microscopy has a spatial frequency passband of  $l^2/4 < (s + s_0) < 1$  with axial and transverse cutoffs 1 and 2, respectively. Here  $s_0 = 1/[2 \sin^2(\alpha/2)]$  is a constant axial spatial frequency shift resulting from the reflection imaging geometry [143]. This feature is the same as fibre-optic reflection-mode non-fluorescence microscopy.

Previous studies have shown that the normalised fibre spot size  $A_j$  plays an important role in transfer function performance of fibre-optic microscopy [141, 143]. Under the paraxial approximation the NA of the objective on the illumination and detection sides can be represented as

$$N_o = a/d . \quad (4.13)$$

In addition, the NA of the SMFs for illumination and collection can be expressed under the Gaussian approximation as

$$N_i = \frac{V_i \lambda_i}{2\pi a_i} , \quad (4.14)$$

where  $V_i$  is the fibre parameter of the illumination and collection fibres ( $i = 1, 2$ ). Therefore, applying Eqs. 4.13 and 4.14 into Eq. 4.10, it can be seen that  $A_j$  is proportional to the square of the ratio of the NA of the objective to the NA of the fibres  $F_1$  and  $F_2$  [136]:

$$A_j \propto (N_o/N_i)^2 . \quad (4.15)$$

The significance of the normalised fibre spot size  $A_j$  is that it plays a similar role to the normalised pinhole radius for a finite-sized detector, and therefore represents the effect of the sizes of the fibre and the objective. The values of  $A_j$  can be varied by changing the NA of the fibre and the objective or the illumination wavelength for a given imaging system. Through the use of Eqs. 4.5 - 4.12, the effect of the parameter  $A_j$  on the 3D CTF for fibre-optic SHG microscopy can be evaluated. When  $A_j \rightarrow 0$ , which corresponds to the case when the NA of the fibre is much larger than that of the objective in illumination and collection paths, the 3D CTF describes confocal SHG microscopy of a point source and a point detector. For the finite value of  $A_j$ , the passband of the 3D CTF in Eq. 4.12 is the same as that in fibre-optic non-fluorescence microscopy. If either  $A_1$  or  $A_2$  becomes infinity, 3D CTF  $c(l, s)$  becomes Eq. 4.9 or Eq. 4.8. No image is formed in this case, because  $c(l, s)$  is zero.

## 4.4 Numerical and experimental results

### 4.4.1 Coherent transfer function

In order to understand the results in Chapter 3, the dependence of the 3D CTF on the normalised fibre spot size is numerically calculated. For a SHG microscope based on a fibre coupler in Chapter 3, we have  $4A_1 = A_2$ , because the delivery of the incident illumination to the sample and the collection of the SHG signal is achieved through the same optical fibre and the excitation wavelength is twice as large as the SHG wavelength. The corresponding 3D CTFs for  $A_1 = 0, 1, 5$  are shown in Figs. 4.3(a)-(c). Fig. 4.3(a) represents the 3D CTF for confocal SHG microscopy with a point source and a point detection. For a finite value of  $A_1$ , the strength of the 3D CTF is reduced in particular along the axial direction, as shown in Figs. 4.3(b) and (c). Observation from Figs. 4.3(a)-(c) reveals that when the normalised fibre spot size,  $A_1$ , for illumination delivery is small, the SHG imaging properties of the system are superior. This is due to the fact that as  $A_1$  increases, the responses of the CTF at high axial and transverse spatial frequencies become weaker.

In the case of independent fibre parameters of  $A_1$  and  $A_2$ , the CTF in the fibre-optic SHG microscope is shown in Fig. 4.3(d), where a point source is used ( $A_1 = 0$ ) and a fibre is used for collection ( $A_2 = 5$ ). In this case, the collection function of the objective becomes weak. Ultimately, when  $A_2 \rightarrow \infty$ ,  $c_2(l, s)$  approaches a delta function at  $l = 0$  and thus the 3D CTF for SHG microscopy is given by Eq. 4.8. A comparison between the performance of the CTF for the two systems based on a point detector and a finite-sized detector can be made through observation of Figs. 4.3(a) and (d). As expected, more information about the finer features and the details in an object can be imaged with a fibre-optic SHG microscope using a point source and a point detector, leading to higher imaging resolution.

It is important to investigate the axial cross section,  $c(l = 0, s)$  of the 3D CTF further as it gives the axial imaging performance, which is studied in detail in the next

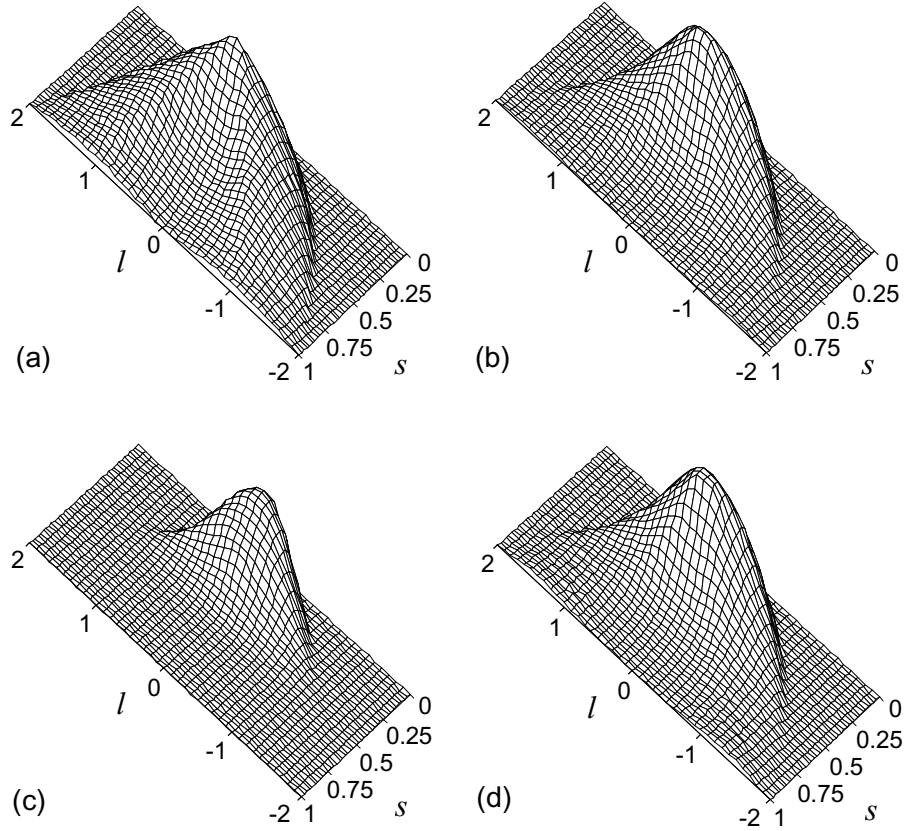


Fig. 4.3: 3D CTF for fiber-optic SHG microscopy. (a)  $A_1 = 0$ ,  $A_2 = 4A_1$ . (b)  $A_1 = 1$ ,  $A_2 = 4A_1$ . (c)  $A_1 = 5$ ,  $A_2 = 4A_1$ , (d)  $A_1 = 0$ ,  $A_2 = 5$ .

subsection. The axial cross section through the CTF for  $l = 0$  corresponds to imaging a planar structure with no variation in the SHG amplitude in the transverse direction. The solid curves in Fig. 4.4 represent the normalised axial cross section of the 3D CTF for SHG microscopy using a fibre coupler ( $4A_1 = A_2$ ), while the dashed line depicts the condition for  $A_1 = 0$  and  $A_2 \rightarrow \infty$ . For  $4A_1 = A_2 = 0$ , the CTF increases linearly up to  $s = 1/3$ , which is contributed by the constant region in Eq. 4.8. After the maximum value at  $s = 1/3$ , the CTF decreases and finally cuts off at  $s = 1$ . When  $4A_1 = A_2$  and  $A_1 \neq 0$ , the strength of the CTF for  $s < 1/3$  is enhanced while that for  $s > 1/3$  is reduced. It can be seen that as  $A_1$  increases, the response of the CTF at high axial spatial frequencies becomes weaker. When eventually  $4A_1 = A_2 \rightarrow \infty$ , the CTF approaches a delta function at  $s = 0$ , which means that there is no axial imaging ability.



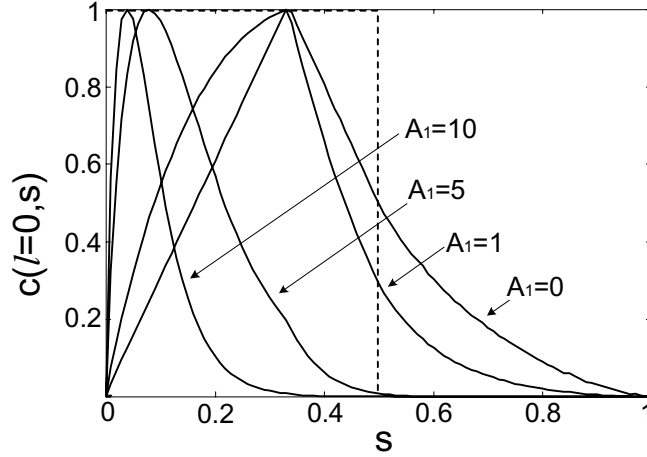


Fig. 4.4: Axial cross section of the 3D CTF for fiber-optic SHG microscopy using a fibre coupler ( $4A_1 = A_2$ ) for different values of the normalised optical spot size parameter  $A_1$ . The dashed curve represents the case for  $A_1 = 0$  and  $A_2 \rightarrow \infty$ .

#### 4.4.2 Axial resolution

To characterise axial resolution, one usually considers imaging of a perfect SHG reflector scanning through the focus of the objective. This axial response is a measure of axial resolution or the optical sectioning property and can be calculated using the modulus squared of the Fourier transform of the axial cross section of the 3D CTF at  $l = 0$  [136, 142, 143]:

$$I(u) = \left| c(l=0, u) \right|^2 = \left| \int c_1(l, u) c_2(l, u) l dl \right|^2. \quad (4.16)$$

Here  $c_1(l, s)$  is the defocused CTF for a fibre-optic reflection-mode non-fluorescence microscope with wavelength  $2\lambda_0$ , thus can be evaluated as [143]

$$c_1(l, u) = \left( 1/(A_1 - iu/2) \right) \exp \left[ - (A_1 - iu/2) l^2 \right] \int_0^{\pi/2} \left\{ 1 - \exp \left[ - (A_1 - iu/2) \rho_0^2 \right] \right\} d\theta, \quad (4.17)$$

where  $\rho_0 = -l \cos \theta + \sqrt{1 - l^2 \sin^2 \theta}$  and  $u = (8\pi/\lambda_0) z \sin^2(\alpha/2)$ . Similarly,  $c_2(l, u)$  represents the defocused CTF for a single circular lens with wavelength  $\lambda_0$ , and is given by [136]

$$c_2(l, u) = \exp \left( - \frac{A_2}{2} l^2 \right) \exp \left( \frac{i}{2} u l^2 \right). \quad (4.18)$$

After mathematical manipulations, such an axial response can be expressed as

$$I(u) = \left| \int_0^1 \left\{ \int \frac{\exp -l^2[(A_1 - iu/2) + (A_2 - iu)/2]}{A_1 - iu/2} \{1 - \exp[-\rho_0^2(A_1 - iu/2)]\} d\theta \right\} l dl \right|^2. \quad (4.19)$$

In a fibre-optic SHG microscope using a fibre coupler ( $4A_1 = A_2$ ), the normalised intensity of the axial response for different normalised fibre spot size parameter  $A_1$  is shown in Fig. 4.5. As we expect, the axial response becomes broader as  $A_1$  increases. It shows that the SHG axial resolution approaches 5.57 for  $A_1 = 0$  and  $A_2 \rightarrow \infty$ . In this case, Eq. 4.19 reduces to  $I(u) = [\sin(u/4)/(u/4)]^2$  and is depicted as a dashed curve in Fig. 4.5, which confirms that SHG microscopy exhibits an inherent optical section property without necessarily using finite-sized detection. This feature also implies that SHG microscopy has an improvement of axial resolution by 35% compared with TPEF microscopy without any pinhole [142].

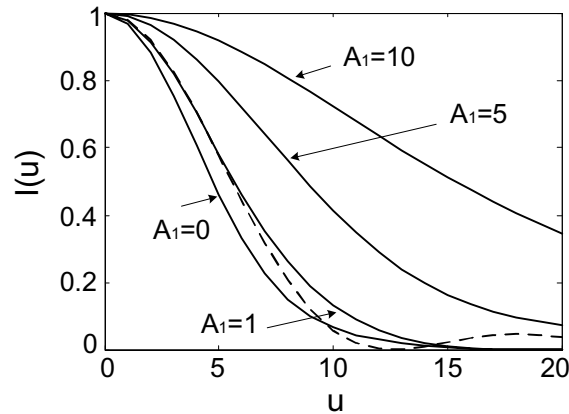


Fig. 4.5: Normalised axial response of a perfect SHG reflector in fibre-optic SHG microscopy using a fibre coupler ( $4A_1 = A_2$ ) for different values of the normalised optical spot size parameter  $A_1$ . The dashed curve represents the case for  $A_1 = 0$  and  $A_2 \rightarrow \infty$ .

In addition, the amount of axial resolution, the half width at half maximum (HWHM),  $\Delta u_{1/2}$ , is plotted as a function of the normalised fibre spot size parameter  $A_1$  in Fig. 4.6(a). It confirms that the SHG axial resolution approaches 5.57 in the case of a point source ( $A_1 = 0$ ) and a large-area detector ( $A_2 \rightarrow \infty$ ). In the case of SHG microscopy using a fibre coupler ( $4A_1 = A_2$ ) presented in Chapter 3, the HWHM

is approximately 4.72 for  $4A_1 = A_2 = 0$ . The HWHM as a function of  $A_1$  exhibits a linear dependence when  $A_1 > 5$ .

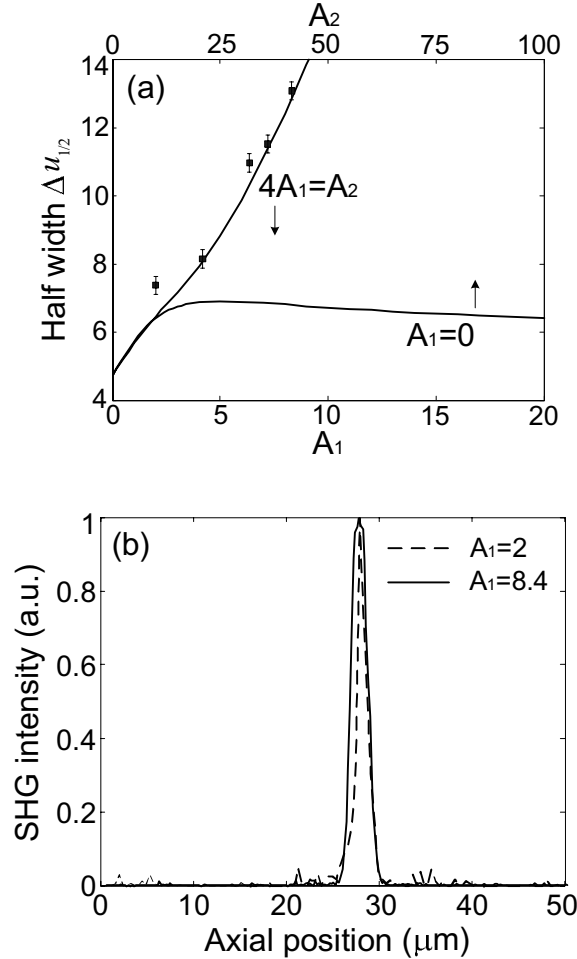


Fig. 4.6: (a) Half width at half maximum of the axial response,  $\Delta u_{1/2}$ , as a function of the normalised fiber spot size parameter when  $4A_1 = A_2$  (bottom axis) and when  $A_1 = 0$  (up axis). (b) Measured axial responses in the fibre-optic SHG microscope using a single-mode fibre coupler for  $A_1 = 2.0$  and 8.4.

To verify the calculation results, we measure the axial responses of the fibre-optic SHG microscope to a thin layer of AF-50 dye under the experimental conditions shown in Fig. 3.7. The measured values of  $\Delta u_{1/2}$  are shown as square spots in Fig. 4.6(a), where  $A_1 = 2.0, 4.2, 6.4, 7.3, 8.4$ , respectively.  $\Delta u_{1/2}$  is derived from the axial response based on  $u = (8\pi/\lambda_0)z \sin^2(\alpha/2)$ . Parameter  $A_1$  is varied by using various values of the NA of the objective to couple the SHG signal into the SMF coupler or changing the illumination wavelength for a given objective. The experimental results further confirm

the dependence of the axial resolution on the normalised fibre spot size parameters. The axial responses of the fibre-optic SHG microscope are shown in Fig. 4.6(b) for  $A_1 = 2.0$  and  $8.4$ , exhibiting axial resolution of  $1.2 \mu\text{m}$  and  $2.1 \mu\text{m}$ , respectively. In the case of  $A_1 = 2.0$ , the NA of the fibre is larger than the convergence angle of the illumination on the fibre aperture, resulting in the improvement in axial resolution. Furthermore,  $A_1 = 6.4$  and  $7.3$  are achieved by tuning the excitation wavelength from  $860 \text{ nm}$  to  $800 \text{ nm}$ . The corresponding axial responses have been shown in Fig. 3.11, where  $\Delta u_{1/2}$  is  $11.5$  with the axial resolution of  $1.83 \mu\text{m}$  at an excitation wavelength of  $800 \text{ nm}$  and  $11.0$  with the axial resolution of  $1.89 \mu\text{m}$  at an excitation wavelength of  $860 \text{ nm}$ . The deviations between the theory and the experimental data might be due to the presence of spherical aberration and the finite thickness of the SHG layer. Compared with the HWHM in fibre-optic TPEF microscopy using an SMF coupler [141], according to Fig. 4.6(a),  $\Delta u_{1/2}$  in fibre-optic SHG microscopy is increased by approximately  $7\%$  for a given normalised fibre spot size  $A_1$ .

### 4.4.3 Signal level

In Section 3.4.3, it is observed experimentally that the detected fluorescence in the nonlinear optical microscopy using an SMF coupler is significantly depended on the gap length, which is related to the normalised fibre spot size  $A_j$ . According to the previous study, the 3D OTF of a fibre-optic TPEF microscope is given by [141]

$$C(\mathbf{m}) = F_3 \left\{ \left| U_1(\mathbf{M}_1 x, \mathbf{M}_1 y) \otimes_2 h_1(\mathbf{M}_1 \mathbf{r}) \right|^4 \right\} \otimes_3 F_3 \left\{ \left| U_2^*(\mathbf{M}_1 x, \mathbf{M}_1 y) \otimes_2 h_2(\mathbf{r}) \right|^2 \right\}, \quad (4.20)$$

where  $F_3$  is the 3D Fourier transform with respect to  $\mathbf{r}_s$ .  $U_1(x, y)$  and  $U_2(x, y)$  are the amplitude profiles on the output end of illumination fibre and the input end of collection fibre. Here  $h_1(\mathbf{r})$  and  $h_2(\mathbf{r})$  are the 3D amplitude PSFs for the objective and collection lenses. The projection of the 3D OTF in the focal plane gives rise to the 2D in-focus OTF, which describes the image property of a thin object in the focal plane. Therefore, for a TPEF system that uses an SMF coupler [141], the detected intensity

of TPEF from a thin fluorescence sheet is proportional to the value of the 2D in-focus OTF  $C_2(l = 0)$  and can be expressed as

$$I(u = 0) = \alpha A_1^5 C_2(l = 0) , \quad (4.21)$$

where  $\alpha$  is a factor of normalisation and  $A_1$  is the normalised fibre spot size.

It should be noted that the excitation power from the illumination fibre is lost by both the truncation of the finite-sized objective and the coupling of the collection fibre. Consequently, under the Gaussian approximation for the SMF coupler, the total fraction of the power converting from the illumination fibre to the collection fibre in a fibre-optic TPEF microscope [138], can be described as

$$\eta = \frac{\alpha I(u = 0)}{A_1} . \quad (4.22)$$

According to the Fresnel diffraction theory, the efficiency of the electric field truncation by the objective can be derived as

$$\eta_1 = 1 - \exp(-A_1) . \quad (4.23)$$

Finally, the signal level in the fibre-optic TPEF microscope using an SMF coupler and a GRIN lens can be expressed as [135, 138]

$$\eta_2 = \frac{\alpha A_1^4 C_2(l = 0)}{1 - \exp(-A_1)} . \quad (4.24)$$

As has been shown in the study of the 3D OTF for fibre-optic TPEF microscopy,  $C_2(l = 0)$  decreases monotonically as  $A_1$  increases. As a result of the balance between  $A_1^4/[1 - \exp(-A_1)]$  and  $C_2(l = 0)$ , the signal level given by Eq. 4.24 leads to a maximum peak, qualitatively confirming the behaviour of Fig. 3.19.

It should be pointed out that the signal level for SHG emission in such a system can be analysed by an equation similar to Eq. 4.24, in which  $C_2(l = 0)$  should be replaced

by the modulus squared of the 2D defocused CTF at  $l = 0$ , which is given by

$$c'(l = 0) = \int c(l = 0, s) ds . \quad (4.25)$$

Therefore, the detected SHG signal as a function of the gap length should exhibit the similar manner as shown in Fig. 3.19.

## 4.5 Chapter conclusions

This chapter has formalised the 3D CTF for fibre-optic SHG microscopy. Its spatial frequency passband is identical to that for fibre-optic reflection-mode non-fluorescence microscopy though the strength of the 3D CTF is reduced due to effects of finite-sized fibre aperture. When the NA of the fibre is much larger than the convergence angle of the illumination on the fibre aperture, corresponding to a normalised fibre spot size of approximately zero, the performance of fibre-optic SHG microscopy behaves as confocal SHG microscopy.

The axial resolution performance of a SHG microscope using an SMF coupler in Chapter 3 has been compared through numerical analysis. It has been shown that SHG microscopy exhibits an inherent optical section property without necessarily using finite-sized detection. Axial resolution of the fibre-optic SHG microscopy is significantly dependent on the normalised fibre spot size. The dependence of axial resolution on fibre coupling parameters shows an improvement of approximately 7%, compared with that in fibre-optic TPEF microscopy. Furthermore, the signal level in fibre-optic nonlinear optical microscopy is qualitatively analysed to understand the experimental results and experimental findings in Chapter 3.

# Chapter 5

## Nonlinear optical endoscopy using a double-clad photonic crystal fibre

### 5.1 Introduction

In Chapter 3, a compact nonlinear optical microscope based on a single-mode fibre (SMF) coupler and a gradient index (GRIN) lens has been achieved to replace complicated bulk optics. The imaging system exhibits a great mechanical flexibility and a compact size, which are desirable for *in vivo* biomedical applications. Furthermore, the ability of the fibre coupler to preserve the linear polarisation of light enables second harmonic generation (SHG) anisotropy measurement to extract molecular orientations of samples. To further extend applications of such an imaging tool, efficient collections of weak two-photon excited fluorescence (TPEF) and SHG are required. Although SMFs can deliver a high quality laser beam and provide an enhanced sectioning capability due to the effective pinhole effect compared with multimode fibres or fibre bundles, the lower numerical aperture (NA) and the finite core size of an SMF give rise to a restricted sensitivity of a nonlinear optical microscope system. Therefore, it is essential to construct a high performance fibre-optic nonlinear optical microscope that can collect images efficiently and maintain the flexibility as well.

As we have seen in Section 2.4, the emergency of photonic crystal fibres (PCFs) has been a renaissance of fundamental research and development on optical fibres. Double-clad PCFs originally developed for fibre lasers have attracted the research in the fields of biosensing and endoscopy for improvement in signal level due to its unique properties of the single-mode central core and the high NA multimode inner cladding. However, as we have mentioned in Section 2.4.3, the prior studies [116, 119] regarding the double-clad PCF are not necessarily applicable in three-dimensional (3D) nonlinear optical microscopy for the following reasons. First, no imaging objective has been used and thus the previous results do not hold for imaging a thick sample, in which an optical sectioning property provided by an objective is necessary. Second, no measurement has been conducted for SHG that is a coherent signal rather than an incoherent signal such as TPEF. Third, due to the different NA of the central core and the inner cladding at different wavelengths, optimising excitation delivery and emission collection with an objective for TPEF and SHG are different. To adopt a double-clad PCF in nonlinear optical microscopy, accurate insight into nonlinear optical imaging performance combining double-clad PCFs is required.

In this chapter, the design and characterisation of a nonlinear optical endoscope that implements a double-clad PCF, a microelectromechanical system (MEMS) mirror and a GRIN lens are presented. Excitation and emission beams are guided by a double-clad PCF that exhibits two efficient transmission paths for excitation and emission wavelengths and the beams are manipulated by a MEMS mirror to form an image. The effectiveness of a double-clad PCF for TPEF and SHG microscopy is experimentally investigated. In particular, the signal collection efficiency in several geometries of nonlinear optical microscopy using the double-clad PCF is compared with that in their counterparts based on an SMF. Potential applications of such a nonlinear optical endoscope are approved by a variety of tissue imaging.

This chapter is organised as follows. Section 5.2 presents the propagation properties of the double-clad PCF characterised by the coupling efficiency, the output pattern, and the polarisation preservation. Based on these characterisation results, a nonlinear



optical microscope using the double-clad PCF is constructed in Section 5.3. The investigation into the enhancement of both TPEF and SHG signal levels is carried out. In Section 5.4, nonlinear optical endoscopy based on the double-clad PCF, a MEMS mirror and a GRIN lens is demonstrated. A particular attention is given to the axial resolution and signal level performance of the system after a GRIN lens and a MEMS mirror are integrated into the imaging system. The usefulness of the endoscope is demonstrated through various tissue imaging experiments described in Section 5.5, including gastrointestinal tract, oral cavity, and cancer tissues. A chapter conclusion is drawn in Section 5.6.

## 5.2 Characterisation of double-clad PCFs

### 5.2.1 Coupling efficiency

The double-clad PCF we have proposed is shown in Fig. 5.1. This fibre is originally designed for multimode pumping in the inner cladding and single-mode emission through the core doped with Yb [117, 118]. Based on our requirement, the doped elements in the core have been removed to produce a passive double-clad PCF for the nonlinear optical imaging. In this way, the fibre is designed to confine near infrared light in the central core as a single transverse mode and confine visible light in the multimode inner cladding. It can be useful for simultaneous nonlinear excitation and signal collection. Furthermore, the NA of the inner cladding produced by the PCF technology is higher than that provided by any other fibre fabrication technology. Hybrid of the single-mode operation in the near infrared wavelength range and the multimode guidance in the visible wavelength range with a high NA in a single fibre can only be offered by PCFs. This is the concept of double-clad PCFs applied to nonlinear optical microscopy in this thesis.

This conceptual double-clad PCF was successfully fabricated by Crystal fibre A/S. The double-clad PCF has a core diameter of  $20\ \mu\text{m}$  (i.e. a  $17\ \mu\text{m}$  mode field diameter at

wavelength 780 nm), an inner cladding with a diameter of  $165\ \mu\text{m}$  and an NA of 0.6 at wavelength 800 nm. The fibre core is surrounded by air holes with a hole to hole pitch ratio of 0.26. Within the outer cladding region of  $340\ \mu\text{m}$  in diameter, a ring of air holes is used to efficiently guide and collect light in the pure silica multimode inner cladding. The background propagation losses are as low as 10 dB/Km at wavelength 800 nm. It should be pointed out that compared with the double-clad fibre used for spectrally encoded endoscopy [116] and the double-clad PCF for TPEF biosensing [119, 120], the size of both core and inner cladding of our fibre is three times larger. Therefore, it gives rise to a further reduced SPM effect and more efficient collection of nonlinear signals.

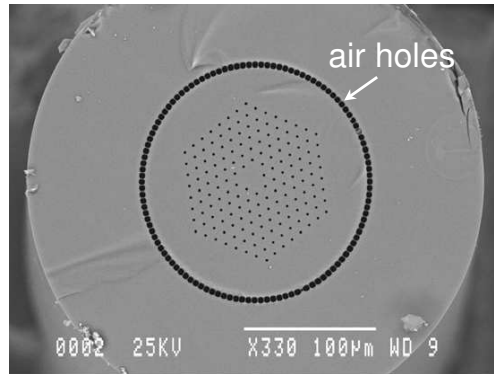


Fig. 5.1: Scanning electron microscopy image of the double-clad PCF used for nonlinear optical microscopy.

As the double-clad PCF in a nonlinear optical microscope is used to deliver a near infrared excitation laser beam and collect nonlinear optical signals in the visible range, it is important to understand the properties of the fibre under various operating conditions. Using the experimental method that has been described in Section 3.2.1, we firstly measure the coupling efficiency and the mode profile of the double-clad PCF in the spectral window of nonlinear optical imaging. Fig. 5.2 shows the coupling efficiency of the fibre for the three given values of the NA of the coupling objectives over the wavelength range between 410 and 870 nm. Moreover, the output patterns of the fibre at different wavelengths are depicted in Fig. 5.3(a)-(f). The correlation of the fibre structure and the mode profile (Fig. 5.3(g)) shows that the double-clad PCF offers the robust single-mode guidance of near infrared light in the central core and the

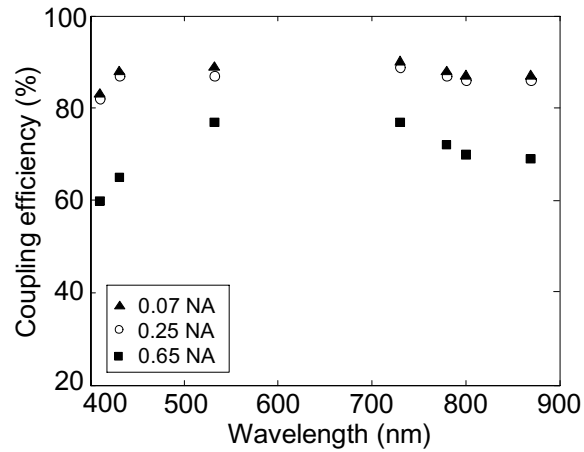


Fig. 5.2: Coupling efficiency of the double-clad PCF in the wavelength range of 410 – 780 nm for three values of the NA (0.07, 0.25 and 0.65) of coupling objectives.

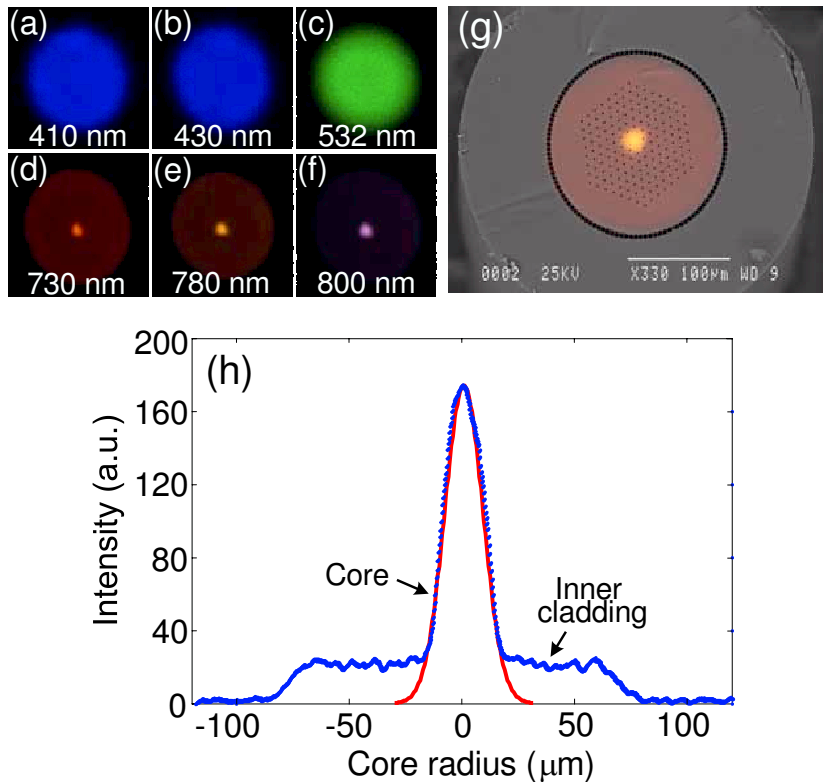


Fig. 5.3: Mode profiles in the double-clad PCF. (a)-(f) Digital camera photograph of the output pattern from the double-clad PCF between wavelengths 410 and 800 nm. A microscope objective with 0.07 NA is used for coupling. (g) Overlay of the scanning electron microscopy image and the output pattern at wavelength 800 nm. (h) Gaussian fit of an intensity profile at the output of the fibre.

efficient propagation of visible light within the multimode inner cladding. Fig. 5.3(h) illustrates an intensity profile across the output pattern of the fibre at wavelength 800 nm (Fig. 5.3(f)). In spite of the leakage from the core to the inner cladding and a triangular shape of the fibre core, the beam profile of the central core has a nearly Gaussian intensity distribution, indicating the single-mode operation in the fibre core at a near infrared wavelength.

A coupling efficiency of over 80% with a maximum of approximately 90% in the wavelength range of 410 – 870 nm is achievable, if the NA of coupling objectives is 0.07 or 0.25 to match the low NA of the central core. However, there is a 20% degradation in the coupling efficiency by using the coupling objective with an NA of 0.65 due to the mode leakage in the inner cladding. It is found that approximately 28% of the output power from the double-clad PCF is guided in the central core at wavelength 800 nm when a coupling objective of NA 0.07 is used, whereas only 10% and 8% are in the core for a coupling objective of NA 0.25 and NA 0.65, respectively. Consequently, the use of a coupling objective with an NA of 0.07 can optimise the coupling efficiency in both the near infrared and the visible wavelength ranges. In particular, the coupling efficiency in the visible wavelength range is approximately twice higher than that obtained with the SMF coupler (see Fig. 3.4). These results confirm that the double-clad PCF can lead to the collection improvement for TPEF and SHG imaging.

### 5.2.2 Degree of polarisation

To demonstrate the feasibility of the double-clad PCF for SHG anisotropy measurement, the investigation of polarisation characteristics of the fibre has been carried out. It is found from our measurement that the degree of polarisation of the output laser beam at wavelength 800 nm (Fig. 5.4(a)) is approximately 0.31. However, the degree of polarisation in the central core (Fig. 5.4(b)) is approximately 0.84, demonstrating that the linear polarisation state is almost preserved in the core of the double-clad PCF at given incident polarisation angles. This result indicates that

a linearly polarised excitation beam can be delivered through the fibre core for SHG anisotropy measurement. It should be noted that the double-clad PCF does not provide a degree of polarisation of approximately 1, as has been demonstrated in an SMF coupler (Section 3.2.3). It may be caused by the depolarisation effect of the large core area and the microstructures in the inner cladding. Further investigation of SHG anisotropy measurement based on the double-clad PCF will be presented in Section 5.3.5.

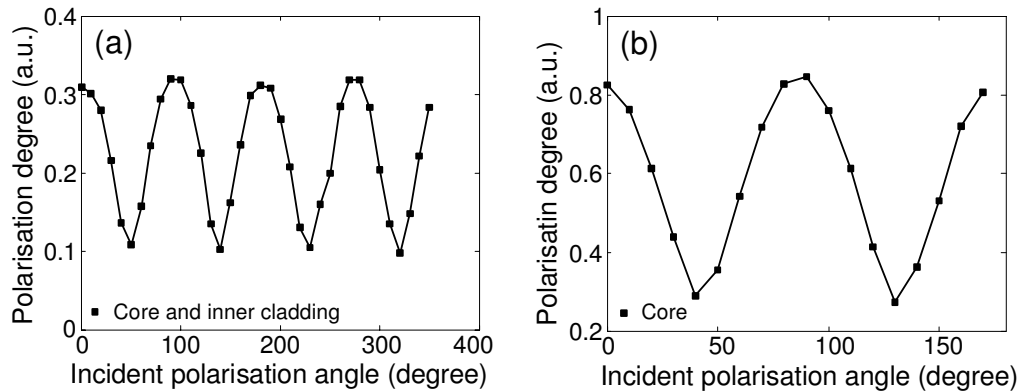


Fig. 5.4: Degree of polarisation of the laser beam delivered by (a) the core/inner cladding region and (b) the central core of the double-clad PCF as a function of the linear polarisation angle of the incident beam at wavelength 800 nm.

## 5.3 A nonlinear optical microscope based on double-clad PCFs

### 5.3.1 Experimental arrangement

To investigate the imaging performance of the double-clad PCF, we construct a nonlinear optical imaging system as shown in Fig. 5.5 [121]. A laser beam generated from a Ti:Sapphire laser (Spectra Physics, Mai Tai) with a repetition rate of 80 MHz and a pulse width of approximately 80 fs is coupled through an iris diaphragm and a microscope objective  $O_1$  (0.65 NA, 40 $\times$ ) into the double-clad PCF with a length

of approximately 1 meter. The size of the iris diaphragm is adjusted to achieve the maximum laser power guided in the central core. The output beam from the fibre is collimated by the objective  $O_2$  of NA 0.07 before being launched into the imaging objective  $O_3$  (0.85 NA,  $40\times$ ). The coupling efficiency of the excitation laser beam to the double-clad PCF is approximately 88%, in which case 38% of the power after the objective  $O_2$  is delivered by the central core. The backward nonlinear signal via the PCF is collected by objective  $O_1$  to match the high NA of the PCF inner cladding. As we have pointed out in Section 5.2.1, the choice of a low NA objective  $O_2$  and a high NA objective  $O_1$  maximises the collection efficiency of the nonlinear signals. A dichroic mirror (DCM) reflects the TPEF and SHG signals, which are further filtered by a bandpass filter (BF) and focused onto a photomultiplier tube (PMT).

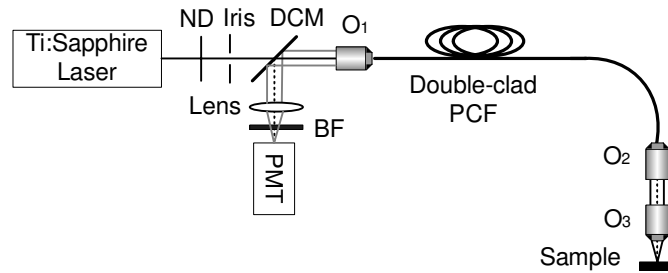


Fig. 5.5: Schematic diagram of the nonlinear optical microscope based on a double-clad PCF.  $O_1$ : 0.65 NA  $40\times$  microscope objective,  $O_2$ : 0.07 NA  $4\times$  microscope objective,  $O_3$ : 0.85 NA  $40\times$  imaging objective, ND: Neutral density filter, BF: Bandpass filter, DCM: Dichroic mirror.

### 5.3.2 Axial resolution

According to microscopic imaging theory, pinhole size has a significant influence on axial resolution in the imaging system [136]. In Section 3.3.3, the capability of 3D spatial resolution of both TPEF and SHG using an SMF coupler has been demonstrated. It has been concluded that SHG axial resolution exhibits a slight improvement compared with TPEF axial resolution. Since the fibre tip is analogous to a conventional confocal pinhole in fibre-optic microscopy and the physical structure of the double-clad PCF is fundamentally different from an SMF, an investigation into

the axial resolution performance of nonlinear optical microscopy using the double-clad PCF is required.

To investigate this property, the axial response of the system is measured by scanning a thin layer of AF-50 dye in the  $z$  direction. The result is shown in Fig. 5.6, where the full width at half maximum (FWHM) of the axial responses of TPEF and SHG at an excitation wavelength of 800 nm is  $2.8 \mu\text{m}$  and  $2.5 \mu\text{m}$ , respectively, obtained by placing a 510/20 nm bandpass filter or a 400/9 nm bandpass filter before the PMT. It reveals a degradation of axial resolution of approximately 33% in the double-clad PCF-based microscope, compared with that in a microscope using an SMF coupler. This may result from the centrally localised light distribution before the imaging objective (see the inset of Fig. 5.6), which effectively decreases the NA of the imaging objective, and the large area of the inner cladding, which effectively increases the pinhole size. Furthermore, in both microscopy using an SMF and a double-clad PCF, a slight enhancement of SHG axial resolution has been shown due to its shorter wavelength [136].

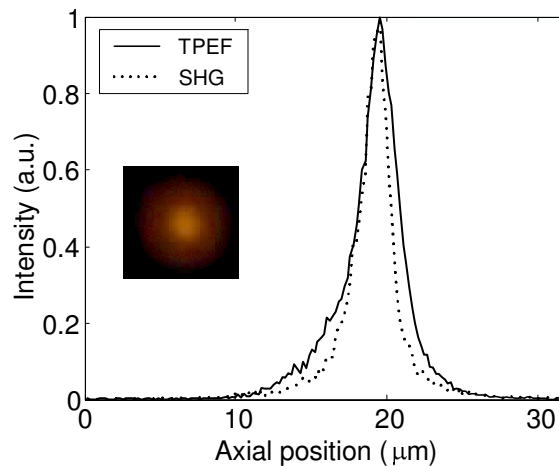


Fig. 5.6: Axial responses of the TPEF and SHG signals from a thin layer of AF-50 dye at an excitation wavelength of 800 nm in a microscope using a double-clad PCF. The inset shows the photograph of the beam profile on the back aperture of the imaging objective. The power on the sample is approximately 1.5 mW.

It should be pointed out that the laser beam from the inner cladding experiences a stronger effect of waveguide dispersion than that from the central core. As a result,

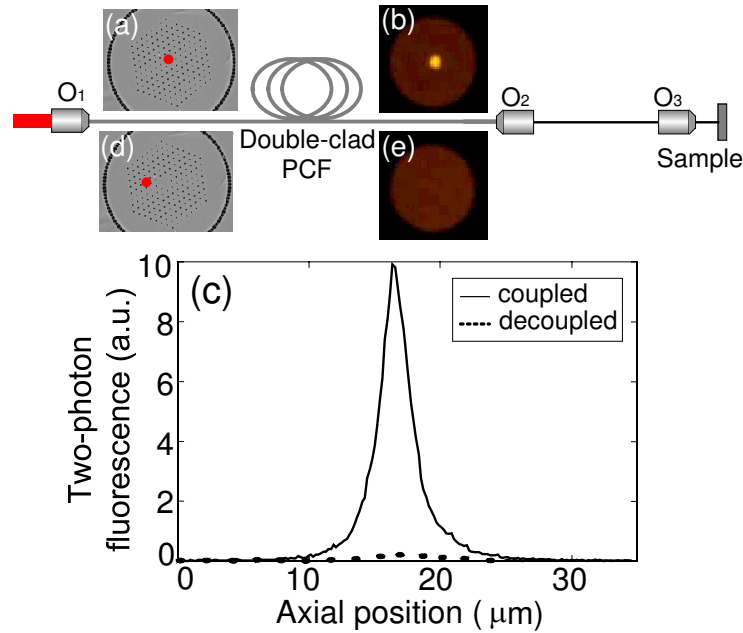


Fig. 5.7: (a)-(b) Schematic diagrams show the laser beam coupled to the core of the double-clad PCF and the output pattern after the fibre. (c) Axial responses for TPEF in the case of the well-coupled illumination in the central core and the decoupled illumination in the inner cladding of the fibre. (d)-(e) Schematic diagrams shows the laser beam decoupled to the fibre core and the output pattern after the fibre.

the ultrashort pulses delivered outside the central core should be broadened to a larger time scale. This feature is confirmed by the experimental investigation of the TPEF axial response depicted in Fig. 5.7. When the excitation beam is well-coupled in the central core (Figs. 5.7(a) and (b)), a centrally localised distribution of excitation beam (the inset of Fig. 5.6) can be observed before the imaging objective. The TPEF axial response to the thin layer of AF-50 in this case is recorded (see the solid curve in Fig. 5.7(c)). However when the excitation beam is decoupled transversely into the inner cladding (Figs. 5.7(d) and (e)), the output power from the fibre is similar, but the peak intensity of the TPEF axial response (see the dashed curve in Fig. 5.7(c)) is decreased by a factor of approximately 39 compared with the well-coupled case. This result indicates that the laser beam delivered outside the central core contributes little to the nonlinear excitation. Furthermore, the fibre core should have the similar dispersion property as the silica material has, enabling the delivery of ultrashort pulses for nonlinear optical processes.



### 5.3.3 Improvement of signal level

As highlighted in Section 2.4.3, the double-clad PCF having large size and NA can lead to a significant improvement in the signal level of the imaging system. To investigate the signal level of the double-clad PCF-based nonlinear microscope, we compare the strength of the axial responses of TPEF and SHG from the double-clad PCF and a standard SMF (Newport, F-SBA). The fused-silica SMF has an operation wavelength of 820 nm, a core/cladding diameter ratio of approximately 4/125 and NA 0.16. The coupling efficiency of the SMF of a 1-m length is approximately 30% at wavelength 800 nm. The FWHM of the axial response with the two types of the fibres is kept the same for a given excitation power. Although an alternative comparison could be performed based on the given pulsewidth on the sample, our treatment is of importance in practical imaging when the excitation power from laser is given.

The TPEF and SHG axial responses of the system using the double-clad PCF and a standard SMF are shown in Figs. 5.8(a)-(d), respectively, where the excitation power before the imaging objective  $O_3$  is varied but the gain of the PMT is identical. The intensity of nonlinear signals detected by the PMT is not normalised. Based on these results, the peak intensity of the axial responses from the two fibres as a function of the power before the imaging objective is shown in Fig. 5.8(e) on a log-log scale. The slope of two demonstrates the quadratic dependence of the TPEF and SHG intensity on the excitation power. It is clearly observed that the detected intensity of the nonlinear signals from the double-clad PCF is approximately 6.8 times stronger than that from the SMF in the case of the same excitation power delivered to the sample. As a result, if one considers that the excitation beams in the central core of the two types of the fibres actually result in the nonlinear process, an enhancement of approximately 40 times in the nonlinear signal intensity detected through the double-clad PCF is achieved.

It should be emphasised that Fig. 5.8 is physically different from previous studies [116, 119, 120], in which no imaging objective was used and the imaging system cannot be used for 3D nonlinear optical imaging. Fig. 5.8(e) is measured from the peak

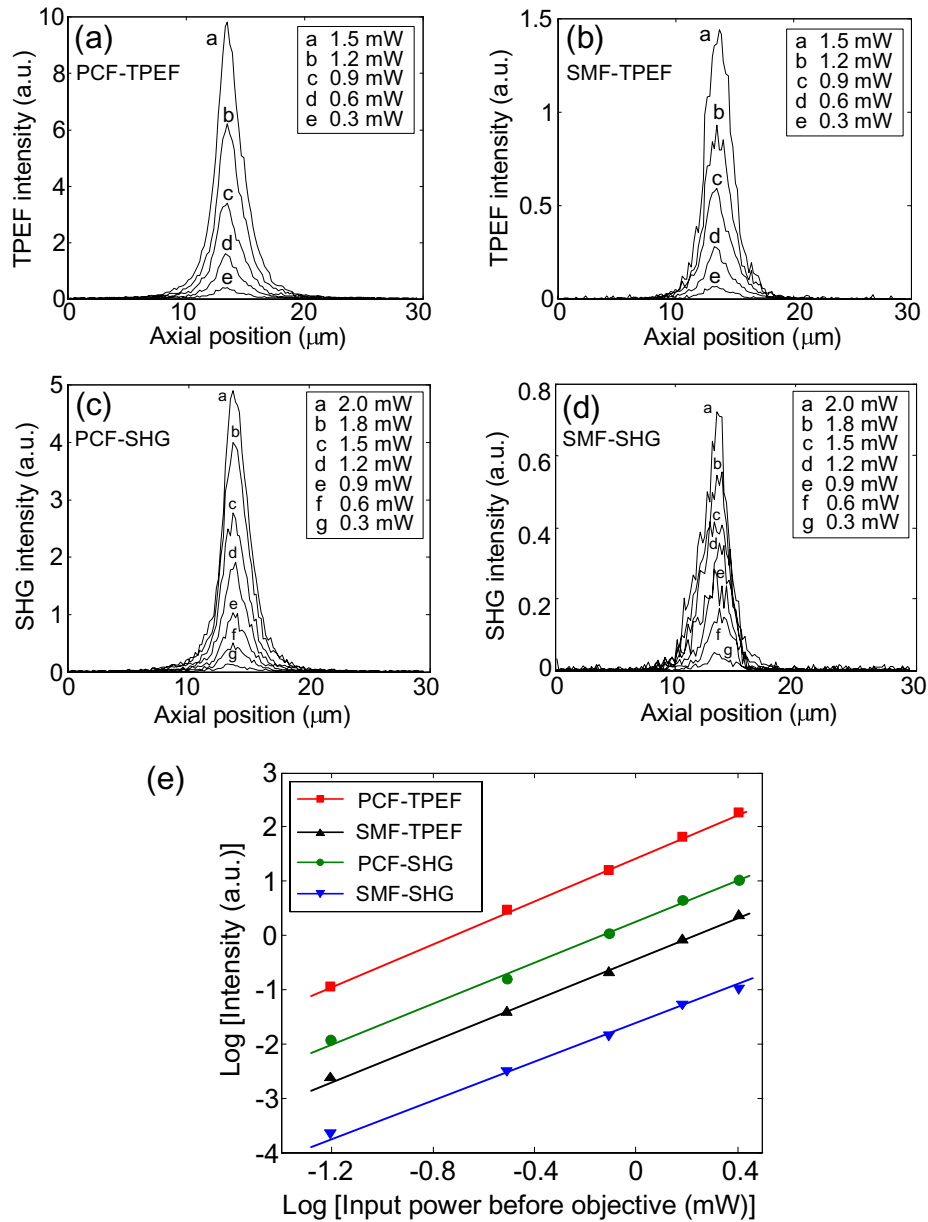


Fig. 5.8: (a)-(d) Sets of TPEF and SHG axial responses in the nonlinear optical microscope using a double-clad PCF and a standard SMF. (e) Detected intensity of TPEF and SHG from the double-clad PCF-based microscope and a standard SMF-based microscope as a function of the power before the imaging objective.

intensity of the axial responses and is thus applicable for imaging a thick sample when an optical sectioning property is critical. This result also reveals that double-clad PCFs can support efficient propagation for the incoherent TPEF signal as well the coherent SHG signal.

To further confirm the enhancement of the 3D imaging efficiency by using double-clad PCFs, SHG optical sections are collected from a scale of black tetra fish with the PCF-based microscope and the SMF-coupler-based microscope, which are shown in Figs. 5.9(a) and (b), respectively. Fig. 5.9(a) is obtained with an illumination power of 3.4 mW from the central core and a PMT voltage of 670 V, while Fig. 5.9(b) is with 15 mW and 815 V, respectively. If a comparison is drawn between Figs. 5.9(a) and (b) by considering the NA and magnitude of the temporal broadening in two cases, the signal level of the PCF-based microscope system is increased by a factor of approximately 65.

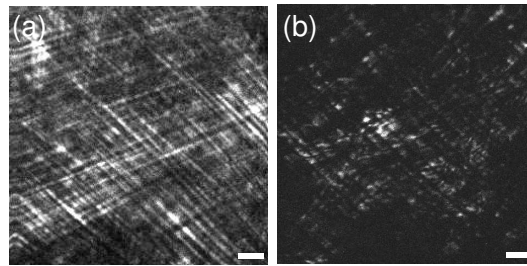


Fig. 5.9: SHG images from a scale of black tetra fish with (a) a PCF-based microscope and (b) an SMF-coupler-based microscope. Scale bars represent  $10 \mu m$ .

### 5.3.4 Nonlinear optical imaging

The 3D imaging capability of the nonlinear optical microscope using a double-clad PCF is demonstrated through a series of imaging experiments. First, a scale of black tetra fish is imaged in order to make a direct comparison with those images obtained with an SMF coupler system (Fig. 3.15 and Fig. 5.9(b)). The result is shown in Fig. 5.10(a), where a series of SHG sections taken at a  $2 \mu m$  depth step into the fish scale are depicted. Second, the feasibility of the system for biomedical study is shown in Fig. 5.10(b), which displays a series of SHG images of rat tail tendon with a  $2 \mu m$  depth

step. The tendon is obtained from an 8-weeks old Sprague-Dawley rat tail, attached to the coverslip directly, and imaged within 2 hours after extraction. The image sections in Fig. 5.10(b) clearly resolve the morphology of mature, well-organised collagen fibrils even at an imaging depth of  $20\ \mu\text{m}$ , showing the pronounced optical sectioning property of the system. The result implies that the efficient PCF-based nonlinear microscope can be a potential tool for direct visualisation of collagen-related diseases. Furthermore, both image sets exhibit high contrast and significantly improved signal level of the system as a result of the efficient signal collection through the double-clad PCF.

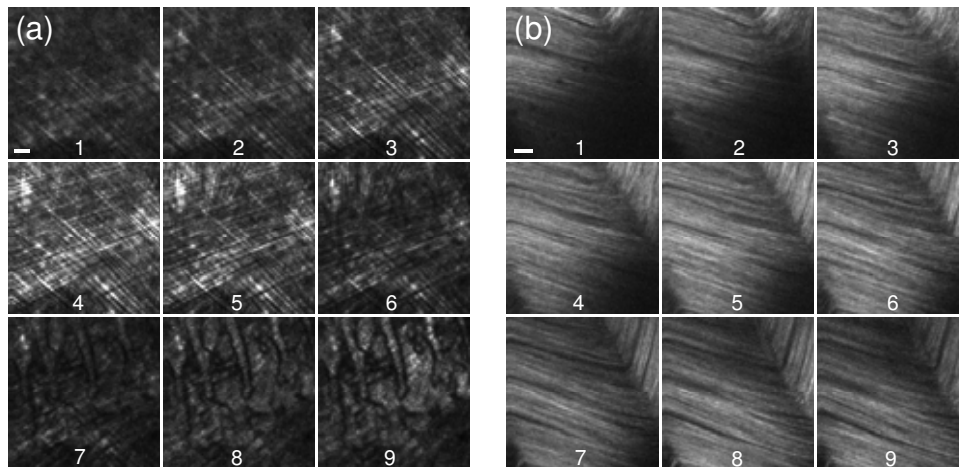


Fig. 5.10: Series of SHG imaging sections from (a) a fish scale and (b) a rat tail tendon in the nonlinear optical microscope using a double-clad PCF. The image section spacing is  $2\ \mu\text{m}$ . The excitation power in the fiber core is approximately 4 mW for (a) and 5 mW for (b). The scale bars represent  $10\ \mu\text{m}$ .

### 5.3.5 SHG polarisation anisotropy

In Section 4.2.2, it has been shown that a degree of polarisation of 0.84 can be preserved in the central core of the double-clad PCF. Under the experimental condition where the linearly polarised light for excitation is delivered by the fibre core, SHG polarisation anisotropy measurements in microscopy using a double-clad PCF are shown in Fig. 5.11. For both fish scale and rat tail tendon, SHG images are obtained in the cases of no analyser before PMT and orthogonal polarisation orientations of the analyser. It is

found that SHG signals from the two well-ordered samples experience depolarisation through the double-clad PCF, because the minimum SHG intensity after the analyser is approximately 0.65 time of the maximum intensity. This result implies that photonic crystal structures in the inner cladding of the fibre result in significant depolarisation effect over the near infrared and the visible wavelength ranges. Therefore, the development of a polarisation-maintained double-clad PCF would benefit the SHG polarisation anisotropy measurement in nonlinear optical microscopy.

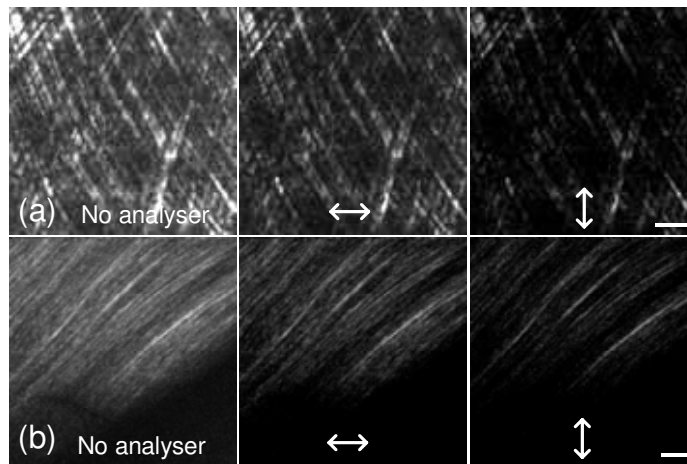


Fig. 5.11: SHG polarisation anisotropy measurements with (a) a fish scale and (b) rat tail tendon in a nonlinear optical microscope using a double-clad PCF. Each set of SHG images is obtained without an analyser or with orthogonal polarisation orientations of the analyser. Scale bars are  $10 \mu m$ .

## 5.4 A nonlinear optical endoscope based on a double-clad PCF and a MEMS mirror

### 5.4.1 Endoscope design

In Section 5.3, the enhancement of the collection efficiency and the 3D high-resolution imaging ability of a double-clad PCF have been demonstrated. However, the geometry presented in Section 5.3 is still based on bulk optical components. This fact limits the

*in vivo* applications of the system in terms of its practicability. To develop a nonlinear optical endoscope, a compact scanning mechanism and a miniaturised objective should be integrated into the imaging system. As a result, we design an ultra-small probe head for nonlinear optical imaging, as shown in Fig. 5.12 [32].

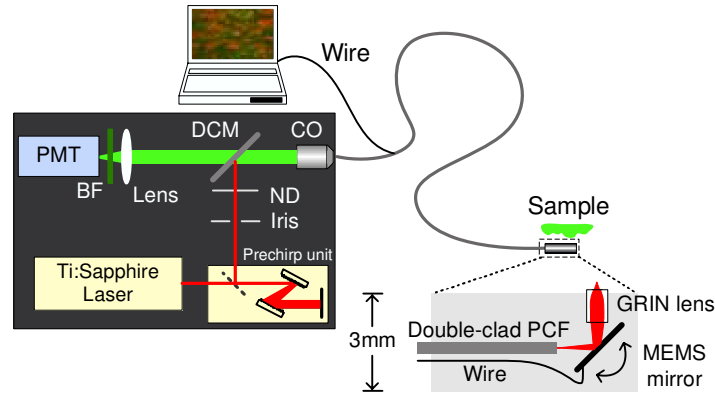


Fig. 5.12: Schematic diagram of the nonlinear optical endoscope based on a double-clad PCF, a MEMS mirror, and a GRIN lens. CO: 0.65 NA 40 $\times$  microscope objective.

A laser beam generated from a Ti:Sapphire laser (Spectra Physics, Mai Tai) with a repetition rate of 80 MHz and a pulsewidth of approximately 80 fs is negatively prechirped by a pair of gratings, which act as a prechirp unit (Newport, 1200 grooves/mm, 28.7 $^\circ$  blaze angle), before coupled through an iris diaphragm, a dichroic mirror (DCM), and a microscope objective CO (0.65 NA, 40 $\times$ ) into the double-clad PCF. This PCF plays a dual role to offer the robust single-mode guidance of the near infrared light in the central core and the efficient propagation of the visible light within the multimode inner cladding. The excitation laser beam coupled from the fibre is reflected and scanned by a MEMS mirror, and then focused onto a sample through a GRIN lens. The backscattering nonlinear signals propagated through fibre are collected by a photomultiplier tube (PMT) via the DCM and a bandpass filter (BF). It should be pointed out that a single GRIN lens is chosen in the design in order to achieve the greatest flexibility and minimise the aberration and the SPM effect occur in the probe. As a consequence, the endoscope head of the nonlinear optical imaging system is approximately 3 mm in diameter, equipped with the MEMS mirror and the GRIN lens.

## 5.4.2 Axial resolution and signal level

Similar to the characterisation we have used in Sections 3.3.3 and 5.3.2, we measure axial responses of the system by scanning a thin layer of AF-50 dye in the  $z$  direction to estimate axial resolution of the endoscope. As we have pointed out in Section 3.4.3, axial resolution and signal level of the system vary as a function of the gap length between the fibre and the back surface of the GRIN lens. To investigate these effects in the system based on a double-clad PCF and a GRIN lens, two 0.2 pitch GRIN lenses (810 nm, 0.5 NA) with diameters of 0.5 mm and 1 mm (GRINTECH) are used to characterise the performance of TPEF axial resolution and signal level, which are shown in Figs. 5.13(a) and (b), respectively.

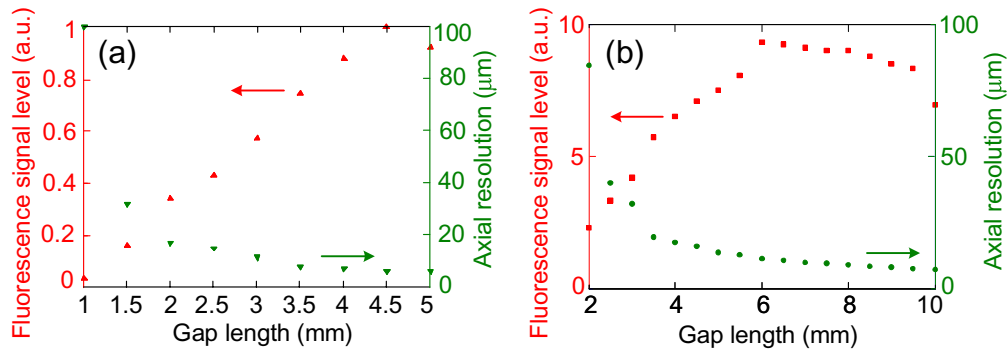


Fig. 5.13: Detected intensity and axial resolution of two-photon fluorescence as a function of the gap length between the double-clad PCF and a GRIN lens: (a) a GRIN lens of 0.5 mm diameter and (b) a GRIN lens of 1 mm diameter. Both GRIN lenses have a pitch of 0.2 at 810 nm.

For both GRIN lenses, the dependence of axial resolution on the gap length exhibits a similar manner as that has been shown in a system using an SMF coupler and a GRIN lens (Fig. 3.18(a)). However, the collected signals through the GRIN lens and the double-clad PCF are more efficient, and therefore do not exhibit significant decrease as the gap length increases. As a result, the system does not show the trade-off feature and simultaneous optimisations of axial resolution and signal level can be obtained by use of double-clad PCFs. In contrast, the optimisations of axial resolution and signal level have to be achieved at different gap lengths in the system based on an SMF coupler and a GRIN lens. This is due to the fact the double-clad PCF has the high

NA and the large core diameter, which are not sensitive to the coupling alignment and aberrations for a given GRIN lens (see Fig. 5.7).

When the gap length is approximately 5 mm to fulfill the back surface of the 0.5 mm-diameter GRIN lens, the optimised axial resolution of TPEF and SHG at an excitation wavelength of 800 nm for the system is approximately 6 mm and 5.4 mm, respectively, depicted in Fig. 5.14(a). In this case, lateral resolution for nonlinear optical imaging is approximately  $1 \mu\text{m}$  and the working distance is approximately  $150 \mu\text{m}$ . The dependence of the peak intensity of TPEF and SHG axial responses on the excitation power on a log-log scale is illustrated in Fig. 5.14(b), demonstrating the quadratic dependence of the nonlinear optical signals and the efficient propagation through the double-clad PCF.

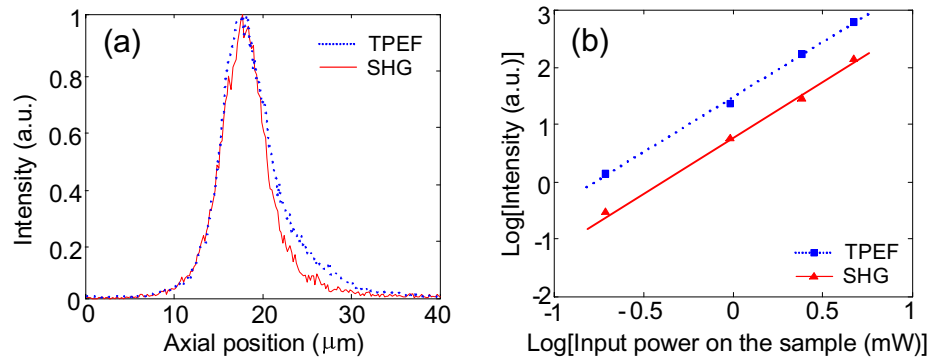


Fig. 5.14: (a) Axial responses of TPEF and SHG in a nonlinear optical microscope using a double-clad PCF and a GRIN lens. (b) Quadratic dependence of TPEF and SHG intensity on the excitation power. The 0.2 pitch GRIN lens has a diameter of 0.5 mm and an NA of 0.5. The excitation wavelength is 800 nm.

To further confirm the high spatial resolution and the enhancement of signal level of the system, a direct comparison is made based on the TPEF images of  $10 \mu\text{m}$  microspheres (Polysciences, Fluoresbrite) obtained from the PCF-GRIN lens-based system and the SMF coupler-GRIN lens-based system (Fig. 5.15). In both geometries, the gap length between the fibre and the GRIN lens is set to obtain the maximum detected signal. After the normalisations of the excitation power and the gain of the PMT, it is found that optimised signal level of the endoscope using a double-clad PCF is approximately 160 times higher than that of the SMF coupler-based endoscope.



Additionally, when the grating pair in the prechirp unit has a diffraction angle of approximately  $15^\circ$  and a distance of approximately 1.2 cm for a 1-meter double-clad PCF, the signal level in the PCF-based system can be further increased by one order of magnitude as a result of the group-velocity dispersion compensation through the fibre.

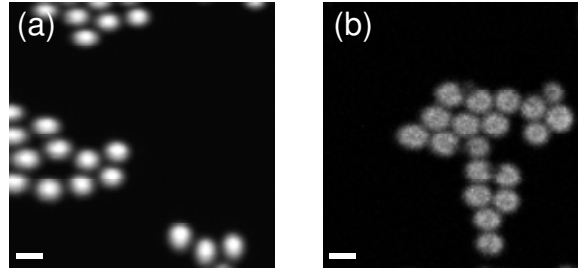


Fig. 5.15: TPEF images obtained from two geometries of fibre-optic nonlinear microscopes: (a) using a double-clad PCF and a GRIN lens (1mm diameter, 0.2 pitch, 0.5 NA) and (b) using an SMF coupler and a GRIN lens (1 mm diameter, 0.25 pitch, 0.46 NA). Scale bars represent  $10 \mu\text{m}$ .

### 5.4.3 Effect of a GRIN lens

To prove the effectiveness of a single GRIN lens for tissue imaging in endoscopy, several imaging experiments using a double-clad PCF, a GRIN lens (0.2 pitch, 0.5 mm diameter, 0.5 NA) and a 2D scanning stage are conducted. Fig. 5.16 is a series of SHG sections of rat tail tendon with a  $5 \mu\text{m}$  depth step. Compared with the SHG images of rat tail tendon obtained with a bulk imaging objective (Fig. 5.10(b)), images acquired with a single GRIN lens still remain high contrast and pronounced optical sectioning. Fig. 5.17 is a series of combined sections of TPEF and SHG from rat esophagus tissue at an excitation wavelength of 800 nm, where Acridine Orange (1%, Sigma) is used to label nucleic acids to give TPEF contrast. Only SHG signals from connective tissue can be observed to exhibit the morphology of the microstructures. *In vitro* SHG images from rat stomach tissue are shown in Fig. 5.18, where the rat stomach tissue is imaged directly after dissection without any stain. These image stacks show that SHG signals originating from collagen are detectable using the double-clad

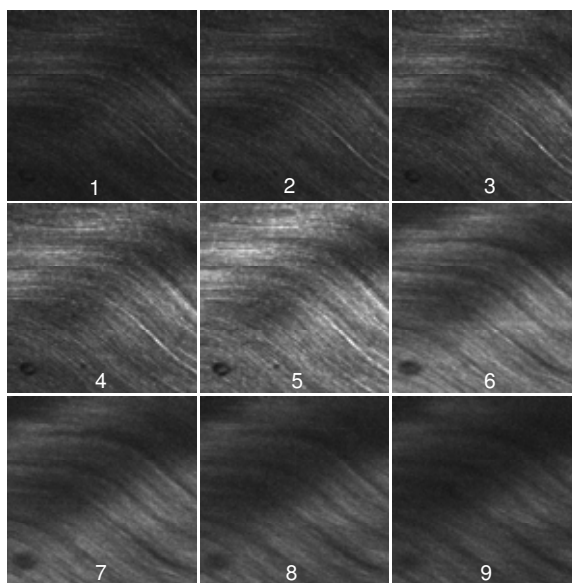


Fig. 5.16: A series of SHG images of rat tail tendon obtained by nonlinear optical microscopy using a double-clad PCF and a GRIN lens. Each section has a lateral dimension of  $150 \mu m \times 150 \mu m$  and is recorded at an axial step of  $5 \mu m$  into the sample.

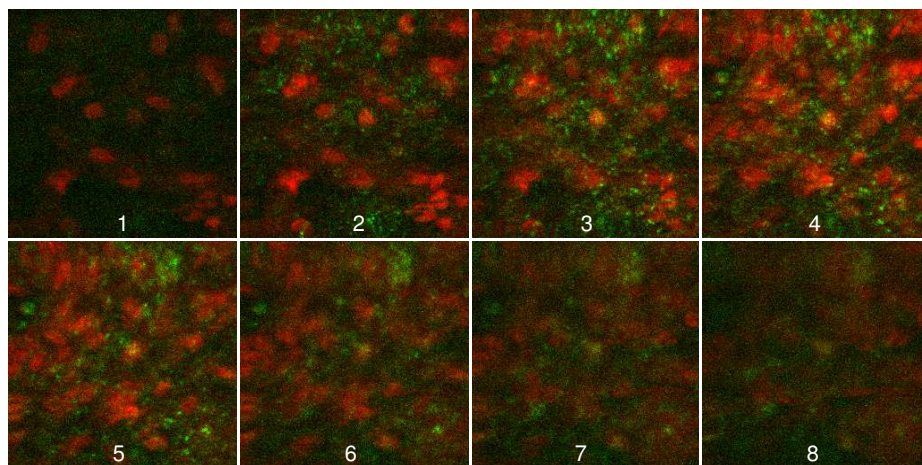


Fig. 5.17: A series of nonlinear optical images of the rat esophagus tissue stained with Acridine Orange in a system using a double-clad PCF and a GRIN lens. TPEF (red) and SHG (green) visualise cell nuclei and connective tissue, respectively. Each section has a lateral dimension of  $100 \mu m \times 100 \mu m$  and is recorded at an axial step of  $5 \mu m$  into the sample. The excitation power on the sample resulting in TPEF and SHG signals is 10 mW and 25 mW, respectively.

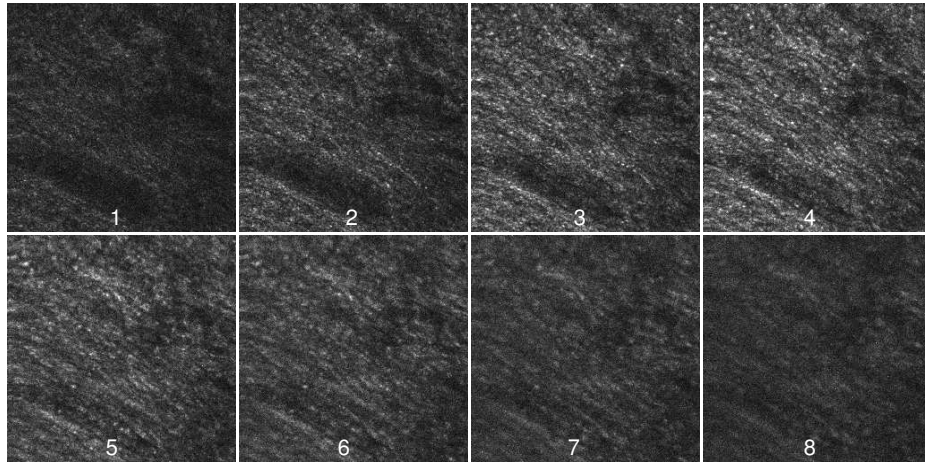


Fig. 5.18: A series of *in vitro* SHG images of connective tissues in rat stomach obtained by nonlinear optical microscopy using a double-clad PCF and a GRIN lens. Each section has a lateral dimension of  $180\ \mu\text{m} \times 180\ \mu\text{m}$  and is recorded at an axial step of  $5\ \mu\text{m}$  into the sample.

PCF and the GRIN lens, demonstrating the potential of this imaging tool in diagnosis of collagen-related diseases.

#### 5.4.4 Feasibility of a MEMS mirror

The nonlinear optical images presented in previous sections are two-dimensionally scanned by a bulk scanning stage. In order to integrate a MEMS mirror into nonlinear optical endoscopy, it is important to investigate the imaging performance of a MEMS mirror under the illumination of femtosecond pulses. The feasibility of a MEMS mirror for nonlinear optical endoscopy is first characterised by the integration of a 1D MEMS mirror, a double-clad PCF, and a GRIN lens. The MEMS mirror we used was designed and fabricated in Prof. H. Xie's group [146] and is shown in Fig. 5.19. The mirror is based on electrothermal bimorph actuation and thus can achieve large rotation angles at low driving voltages. The mirror plate is 1 mm by 1 mm in size, coated with aluminium for broadband high reflectivity. The mirror surface is flat due to a thick single-crystal silicon layer underneath. The radius of curvature of the mirror surface is about 0.5 m. It has a resonance frequency of 165 Hz, exceeding the scanning speed

and angle requirements for most endoscopic applications. The excitation laser beam coupled from the double-clad PCF is reflected and scanned one-dimensionally by the MEMS mirror and focused onto the sample through the GRIN lens. In order to achieve a smooth line scanning, the mirror scans at a frequency of 1 Hz in our experiment.

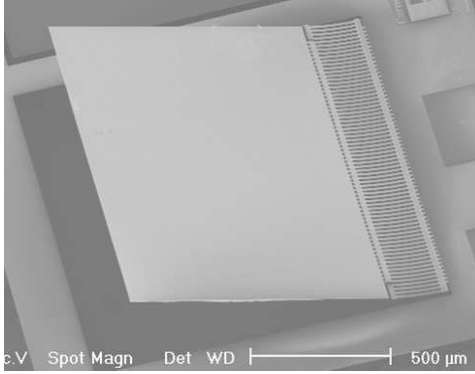


Fig. 5.19: Scanning electron microscopy image of a 1D MEMS mirror used for nonlinear optical endoscopy [146].

Fig. 5.20(a) illustrates a series of SHG line profiles from rat tail tendon with a depth spacing of  $10 \mu m$ . In this case, a  $0.2$  pitch GRIN lens having a diameter of  $1$  mm is used and the field of view on the sample is approximately  $35 \mu m$  that corresponds to an optical scanning angle of approximately  $6$  degrees of the MEMS mirror. Only  $5$  V is needed to obtain a  $6$ -degree rotation. In our experiments, as the laser beam is scanned at the back surface of the GRIN lens, the GRIN lens is underfilled and results in axial resolution of approximately  $10 \mu m$ . The performance of the system (optical sectioning ability and signal level) is consistent with that in a system using a bulk scanning stage presented in Section 5.4.3. Further, a SHG line profile from the rat esophagus tissue is shown in Fig. 5.20(b). The rat esophagus is removed from a euthanized rat, immersed in Hank's balanced salt solution (no phenol red) and imaged directly without any staining. The excitation power on the sample resulting in SHG signals is approximately  $30$  mW. Fig. 5.20(b) confirms that the nonlinear optical endoscope probe based on the double-clad PCF, the GRIN lens and the MEMS mirror enables rat esophagus imaging *in vitro*. Using a MEMS mirror as the scanning unit and a GRIN lens to produce a fast scanning focal spot offers a great potential to develop a compact

nonlinear optical endoscope probe for *in vivo* applications.

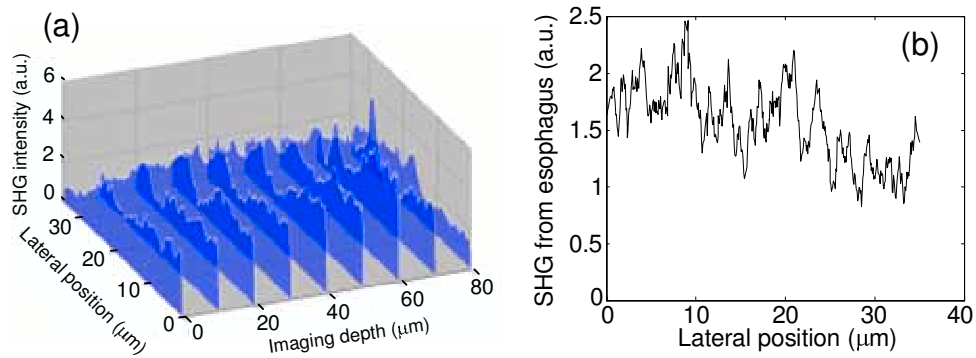


Fig. 5.20: (a) A series of SHG line profiles taken at a  $10\ \mu\text{m}$  step into rat tail tendon and (b) A SHG line profile from unstained rat esophagus tissue obtained with a nonlinear optical endoscope using a double-clad PCF, a 1D MEMS mirror, and a GRIN lens.

### 5.4.5 2D Endoscopic imaging

Since the feasibility of a MEMS mirror for nonlinear optical endoscopy has been demonstrated, it is necessary to integrate a 2D MEMS mirror into the system in order to achieve 3D endoscopic nonlinear optical imaging and realise this practical instrument. Various single-crystal-silicon-based 2D micromirror devices have been reported for biomedical applications [95,99]. Most of these optical scanners require high actuation voltages for large rotation angles due to their use of electrostatic actuation. However, optical scanners needed by endoscopic biomedical imaging applications are required to scan large optical angles with a high scanning speed, but at low driving voltages [147]. The 2D MEMS mirror based on electrothermal actuation can perform large bi-directional 2D optical scans over  $\pm 30^\circ$  at less than 12Vdc [147]. Fig. 5.21 is the scanning electron microscopy image of the 2D MEMS mirror fabricated by Prof. H. Xie's group and used for our nonlinear optical endoscope. The aluminum-coated mirror plate is 0.5 mm by 0.5 mm in size [147]. Furthermore, the small initial tilt angle of the mirror simplifies the endoscope design and packaging.

Line scans can be obtained by applying dc voltages on each actuator individually. We choose two actuators as slow and fast scanning axes for 2D image formation. The

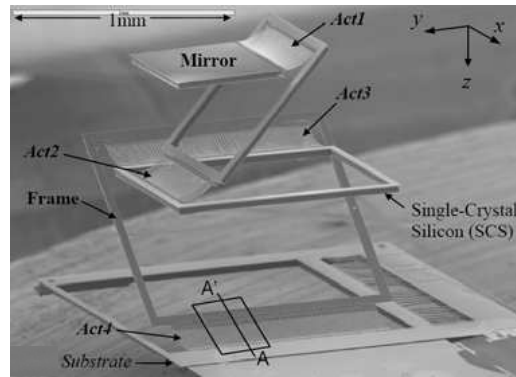


Fig. 5.21: Scanning electron microscopy image of a 2D MEMS mirror in a nonlinear optical endoscope [147].

corresponding optical scanning angle versus actuation-voltage characteristics for the two actuators are shown in Fig. 5.22(a). It can be observed that the optical scanning angles have a linear dependence on the actuation voltage in the range between 2.5 and 7.5 Vdc.

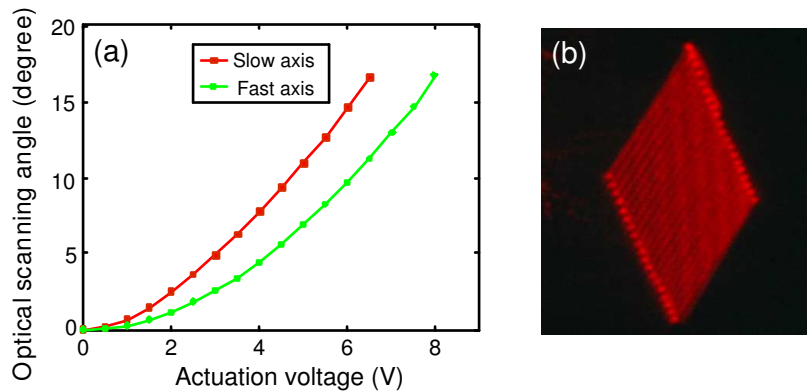


Fig. 5.22: Performance of a 2D MEMS mirror in a nonlinear optical endoscope. (a) Optical scanning angle of slow and fast axes as a function of the applied voltage. (b) A 2D raster scanning pattern generated by the MEMS mirror.

However, the difficulty in driving a MEMS mirror for smooth scanning is that any sudden alteration of the applied voltage on actuators will cause damage or irregular scanning patterns. The problem is solved by the design of a special ramp waveform to increase or decrease the actuation voltage gradually. A 2D raster scanning pattern generated by this MEMS mirror is shown in Fig 5.22(b). Two actuators are synchronised and excited to create their linear angular displacement by applying driving

voltages based on the designed ramp waveform. The 20 parallel lines in the raster scanning pattern cover optical scanning angles of approximately  $10^\circ$  for both fast and slow axes. In the 2D scanning pattern, the deviation of the line scan from its primary axis is caused by thermal coupling between the actuators. Images are reconstructed based on the parallelogram angular area. It should be pointed out that the low driving voltage, the simple structure, and ruggedness to operation make the 2D MEMS mirror suitable for the endoscopic system and safe for clinical applications.

The capability of 2D MEMS mirror for nonlinear optical endoscopic imaging is demonstrated by the TPEF image (Fig. 5.23) with  $10\ \mu\text{m}$  diameter fluorescent microspheres. It shows that the 2D MEMS mirror enables the efficient delivery of the light beam over the broadband wavelength range and the smooth response for image acquisition. In this case, a GRIN lens with a large diameter (Melles Griot, 1.8-mm-diameter, 0.6 NA, 0.23 pitch) is used to produce a field of view up to  $150\ \mu\text{m}$ . The performance of the system is also confirmed by the comparison between this image and the TPEF image (Fig. 5.15(b)) obtained from a system based on an SMF coupler, a GRIN lens and a bulk scanning stage. It also should be pointed out that the signal level of the nonlinear optical endoscope is approximately 120 times higher than the microscope system using an SMF coupler and a bulk scanning mechanism.

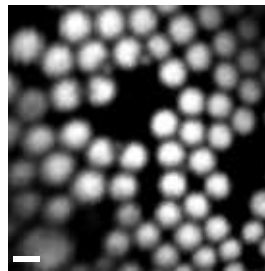


Fig. 5.23: TPEF images of fluorescence microspheres using nonlinear optical endoscopy based on a double-clad PCF, a GRIN lens, and a MEMS mirror. The power resulting in fluorescence excitation is approximately 1.8 mW and the scanning rate of the mirror is 7 lines/second. The scale bar represents  $10\ \mu\text{m}$ .

## 5.5 3D Tissue imaging

There are a number of potential applications for the nonlinear optical endoscope we have developed. Since the majority of cancers are epithelial tissues in origin, we have focused our efforts on imaging of epithelia tissues. All experiments are approved by the University Animal Experimentation Ethics Committee. The excitation power is approximately 40 mW at 800 nm. Based on the GRIN lens (Melles Griot, 1.8-mm-diameter, 0.6 NA, 0.23 pitch) and the MEMS mirror (actuation voltages of 2.5 – 7 V on the fast axis and 3 – 6.9 V on the slow axis, the scanning rate of 7 lines/second), the imaging field of view is approximately  $140 \mu\text{m} \times 100 \mu\text{m}$ .

Epithelial pre-cancers and cancers are associated with morphological and functional alterations of cells, normally assessed by invasive biopsy. Due to the unique features of nonlinear optical imaging, the use of nonlinear optical endoscopy in the normal endoscopic procedure has the following advantages: 1) Combined with the macroscopic imaging capability of an endoscope, nonlinear optical microscopy provides microscopic imaging to identify metaplasia or flat lesions that are not easily resolved by traditional endoscopy. 2) The visualisation of the size and spatial arrangement of nuclei and vascular structures in three dimensions within tissue may reduce or remove the need of tissue excision for histopathologic interpretation. 3) The 3D high-resolution imaging ability enables a more accurate differentiation between normal and malignant tissues to give better diagnosis. Therefore, we explore the potential of our nonlinear optical endoscope in clinical applications by imaging through rat tail tendon, gastrointestinal tract tissue, oral cavity tissue, and cancer tissue, which will be presented in the upcoming subsections.

### 5.5.1 Imaging with rat tail tendon

The ability to obtain 3D SHG images through the system using a 2D MEMS mirror is shown by a series of SHG optical sections from rat tail tendon (Fig. 5.24). The



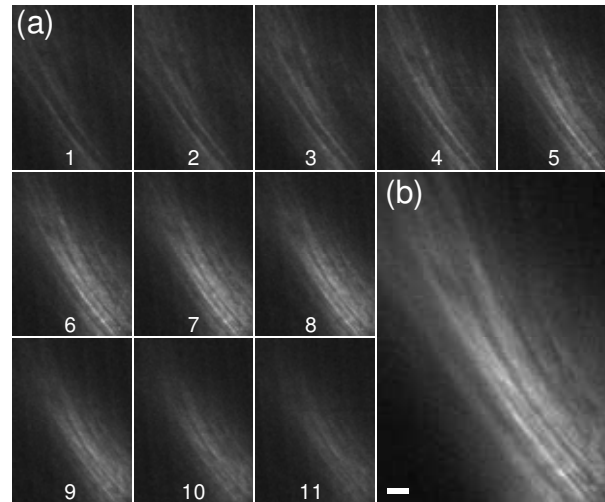


Fig. 5.24: (a) A series of SHG sections of rat tail tendon using a nonlinear optical endoscope based on a double-clad PCF, a MEMS mirror, and a GRIN lens. Imaging spacing is  $10 \mu m$ . The power resulting in the SHG imaging is approximately 30 mW. (b)  $Z$  projection of SHG sections shown in (a). Scale bar is  $10 \mu m$ .

tendon is dissected from a Sprague-Dawley rat tail and imaged directly. It can be seen that in terms of the contrast pattern and axial resolution, the nonlinear optical images produced by the MEMS mirror is consistent with the images shown in Fig. 5.16, which is obtained with a double-clad PCF, a GRIN lens, and a scanning stage.

### 5.5.2 Imaging with gastrointestinal tract tissue

Gastrointestinal malignancies continue to be the second leading cause of cancer-related deaths in Australia. Conventional endoscopy using white light does not detect dysplasia and subtle lesions [148]. Optically based endoscopy offers the potential of detecting the early mucosal changes at the microstructural, biochemical, and molecular levels. Confocal endoscopy has been developed for fluorescence endoscopic imaging using a 488 nm beam from an argon laser [148]. However, a major limitation of epifluorescence microscopy is the difficulty in examining thick tissues. Using nonlinear optical endoscopy, the 3D structure of the sample can be determined with a greater depth up to a few hundred micrometers.

Fig. 5.25(a) is a series of *in vitro* images of rat large intestine tissue. The large intestine is extracted from a Sprague-Dawley rat. To enhance the contrast in endoscopic imaging, luminal epithelial tissue of rat large intestine is stained with 1% Acridine Orange (Sigma) in Ringer's solution. TPEF images are obtained through the thick tissue with a penetration depth of  $80\ \mu\text{m}$ . An observation from these images shows that surface epithelial cells surrounding intestinal crypts (see arrows in frame 3) can clearly be seen. The contrast pattern obtained with the nonlinear optical endoscope is consistent with that based on a commercial laser scanning TPEF microscope (Olympus, Fluoview 300). The structural details in the rat large intestine tissue are well visualised in the 3D reconstruction of the image stack (Fig. 5.25(b)).

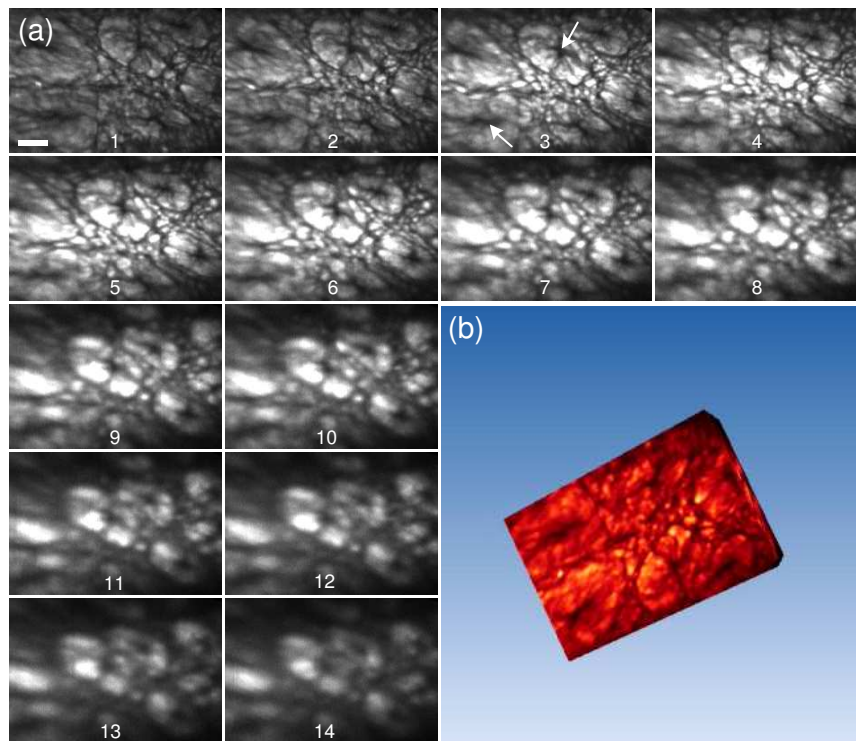


Fig. 5.25: (a) A series of *in vitro* images of rat large intestine tissue obtained by the nonlinear optical endoscope using a double-clad PCF, a MEMS mirror, and a GRIN lens. Each section is recorded at an axial step of  $7.5\ \mu\text{m}$  into the sample. Arrows in frame 3 are pointing to the intestinal crypts. The scale bar is  $20\ \mu\text{m}$ . (b) 3D visualisation of the rat large intestine tissue based on the image stack in (a). Image reconstruction is performed using AMIRA (Mercury Computer Systems).

Under the same experimental condition, rat stomach and esophagus tissues are examined with the nonlinear optical endoscope, shown in Figs. 5.26 and 5.27,

respectively. Epithelia surfaces of both tissues are stained with 1% Acridine Orange in Ringer's solution. 3D TPEF images can be taken into epithelial tissues of rat stomach and esophagus with penetration depths of approximately  $80\ \mu\text{m}$  and  $100\ \mu\text{m}$ , respectively. In particular, the high resolution of the nonlinear optical endoscope enables visualisation of the openings to the gastric pits of the stomach columnar mucosal tissue (arrows in frame 7 of Fig. 5.26(a)). These results demonstrate that the nonlinear optical endoscope that offers the micrometer-scale resolution in deep tissue may differentiate various tissue types and identify early mucosal lesions in the gastrointestinal tract.

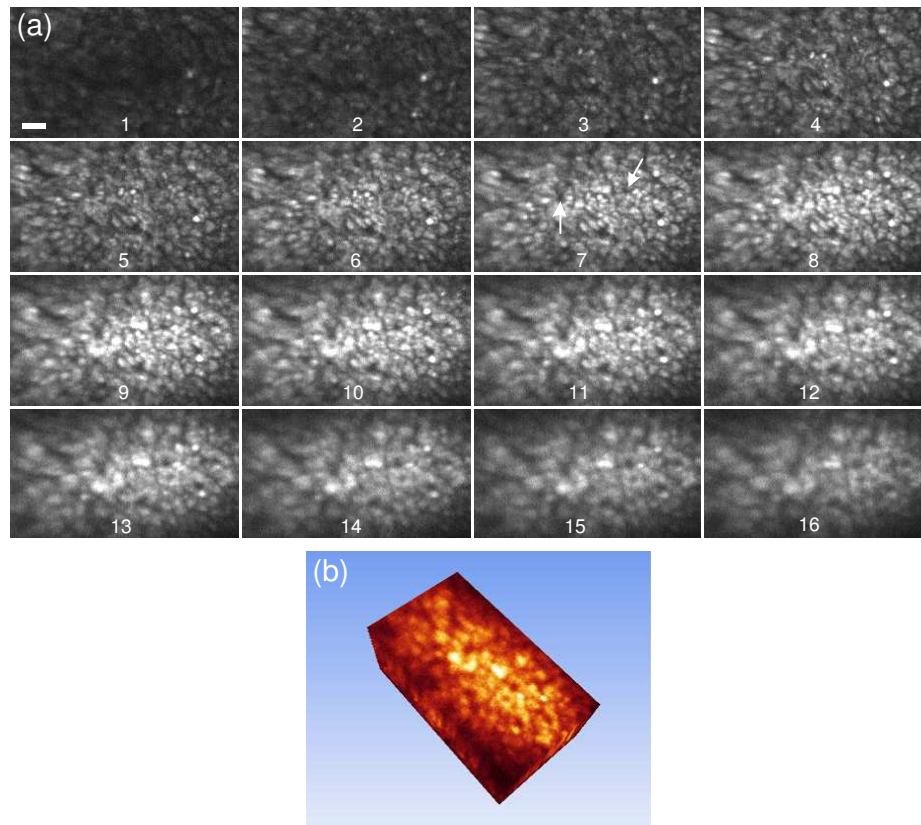


Fig. 5.26: (a) A series of *in vitro* images of the rat stomach tissue obtained by a nonlinear optical endoscope. Each section is recorded at an axial step of  $5\ \mu\text{m}$  into the sample. Arrows in frame 7 are pointing to the gastric pits of the stomach columnar mucosal tissue. The scale bar is  $20\ \mu\text{m}$ . (b) 3D visualisation of the rat stomach based on the image stack in (a).

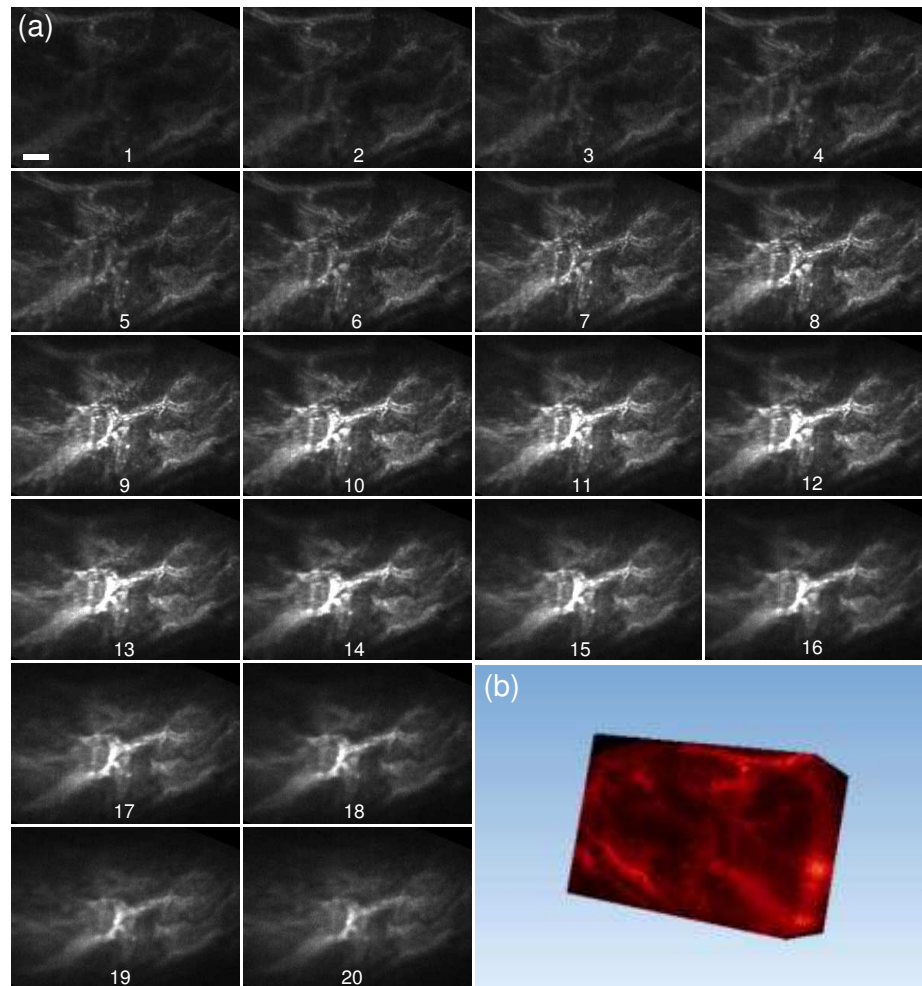


Fig. 5.27: (a) A series of *in vitro* images of the rat esophagus tissue obtained by a nonlinear optical endoscope. Each section is recorded at an axial step of  $5 \mu\text{m}$  into the sample. The scale bar is  $20 \mu\text{m}$ . (b) 3D visualisation of the rat esophagus based on the image stack in (a).

### 5.5.3 Imaging with oral cavity tissue

Diseases in oral cavity is usually characterised by morphological alterations in the lamina propria and submucosa of the oral mucosa. Auto-fluorescence spectroscopy has been used to study oral cavity diseases [149]. However, fluorescence has rarely been reported in this area due to the lack of compact imaging tools. We use the developed nonlinear optical endoscope to characterise the 3D nonlinear optical imaging contrast of several locations in the oral cavity of a pig. The pig head is purchased from a butcher in Victoria Market (Australia). Tissues are extracted and used for imaging within 5

hours after the sacrifice of the pig. All tissues are topically stained with Acridine Orange (1% in Hank's Balanced Salt Solution).

Fig. 5.28 is the TPEF images of the porcine buccal cavity mucosal tissue in three dimensions, showing a penetration depth of approximately  $75 \mu\text{m}$ . Stained stratified squamous epithelial cell nuclei can be seen over the underlying lamina propria region. Image stacks of the porcine oropharynx tissue and the porcine inner lip endothelial tissue are presented in Figs. 5.29 and 5.30, respectively, where stained epithelial nuclei can be seen. 3D TPEF images can be achieved at a depth of approximately  $100 \mu\text{m}$  and  $75 \mu\text{m}$  for the porcine oropharynx tissue and the porcine inner lip endothelial tissue, respectively. Surface squamal cells in porcine inner lip endothelial tissue can be clearly identified over the underlying lamina propria region.

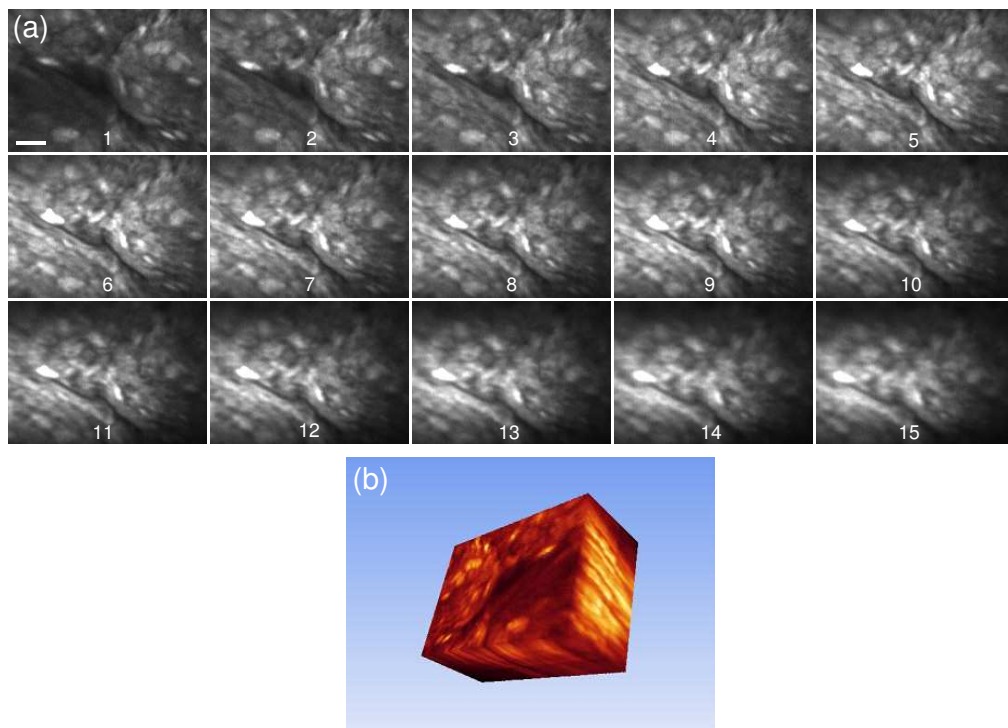


Fig. 5.28: (a) A series of *in vitro* images of the porcine buccal cavity mucosal tissue obtained by a nonlinear optical endoscope. Each section is recorded at an axial step of  $5 \mu\text{m}$  into the sample. The scale bar is  $20 \mu\text{m}$ . (b) 3D visualisation of the porcine buccal cavity mucosal tissue based on the image stack in (a).

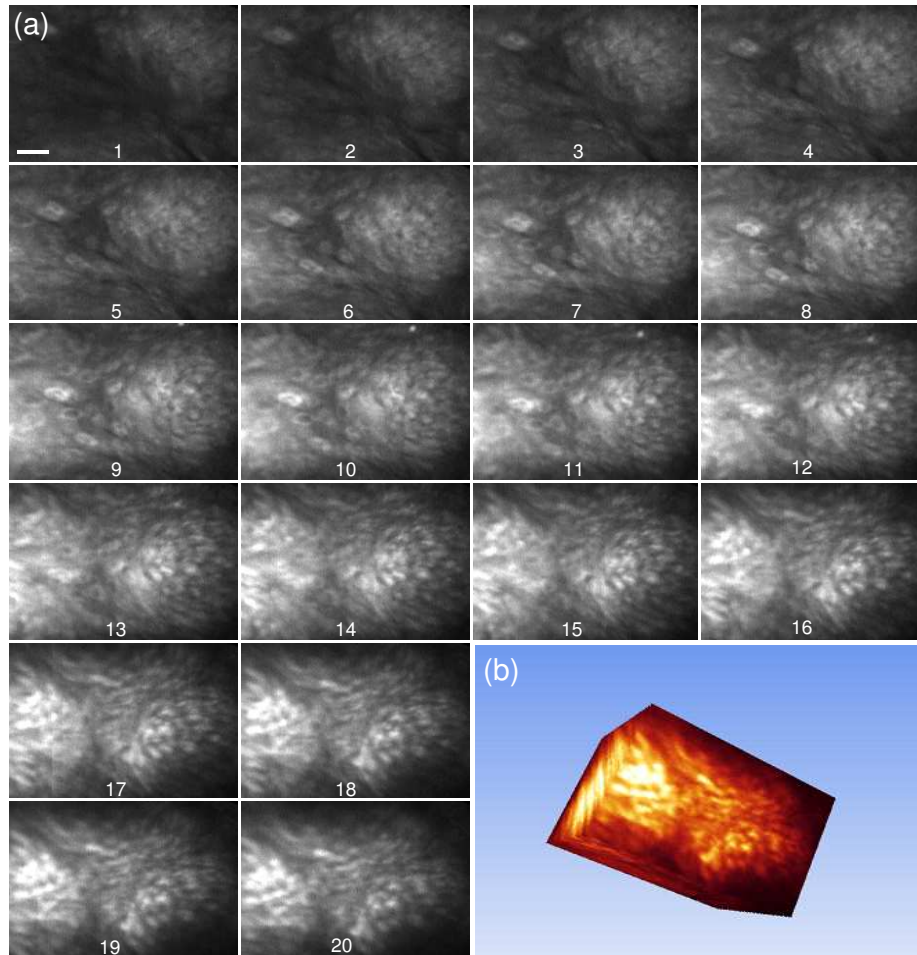


Fig. 5.29: A series of *in vitro* images of the porcine oropharynx tissue obtained by a nonlinear optical endoscope. Each section is recorded at an axial step of  $5 \mu\text{m}$  into the sample. The scale bar is  $20 \mu\text{m}$ . (b) 3D visualisation of the porcine oropharynx tissue based on the image stack in (a).

#### 5.5.4 Imaging with cancer tissue

As we have mentioned in Chapter 1, cancer research using nonlinear optical imaging is an active field. Furthermore, one of the initial motivations of the development of nonlinear optical endoscopy is cancer tissue imaging. To demonstrate the imaging ability of our nonlinear optical endoscope for cancer tissue, we have characterised two types of cancer tissues xenografted in a nude mouse. First, 2008 human ovarian carcinoma cell are xenografted into the hind leg of a nude Balb c mouse, and cultured for one week. This human ovarian cancer tissue is dissected from the nude mouse and

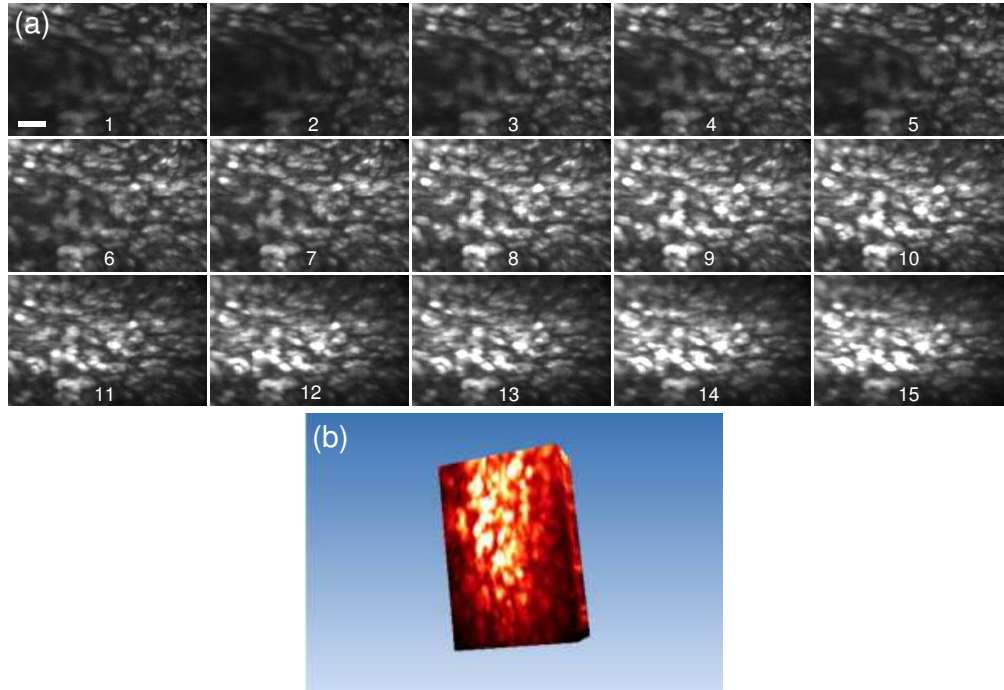


Fig. 5.30: (a) A series of *in vitro* images of the porcine inner lip endothelial tissue obtained by a nonlinear optical endoscope. Each section is recorded at an axial step of  $5 \mu\text{m}$  into the sample. The scale bar is  $20 \mu\text{m}$ . (b) 3D visualisation of the porcine inner lip endothelial tissue in (a).

stained with 1% Acridine Orange. The 3D TPEF images have been shown in Fig. 5.31 with a penetration depth of approximately  $90 \mu\text{m}$ . Second, images of human u-87 MG glioblastoma cells (a kind of human breast cancer cells) xenografted into a nude mouse are presented in Fig. 5.32 with a penetration depth of approximately  $75 \mu\text{m}$ . In both cases, the distribution of cell nuclei in the cancer tissue is extremely dense. Therefore the contrast patterns are very different from that collected from the normal tissue of gastrointestinal tract and oral cavity. Beyond the morphological identification, specific labels and methods such as fluorescence proteins and fluorescence lifetime measurement could be combined with the nonlinear optical endoscope to study cancer tissue imaging in multi-dimensions.

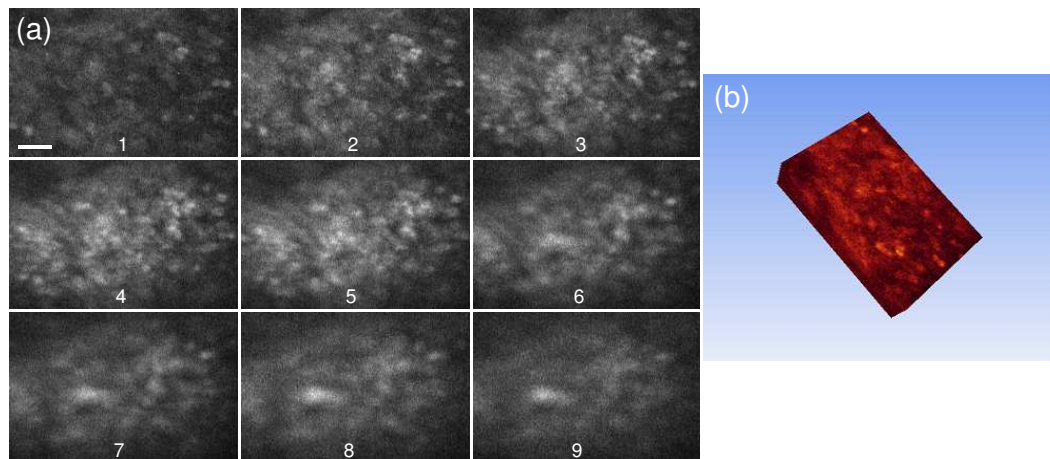


Fig. 5.31: (a) A series of *in vitro* images of the 2008 human ovarian carcinoma cell obtained by a nonlinear optical endoscope. Each section is recorded at an axial step of  $10 \mu\text{m}$  into the sample. The scale bar is  $20 \mu\text{m}$ . (b) 3D visualisation of the human ovarian cancer tissue.

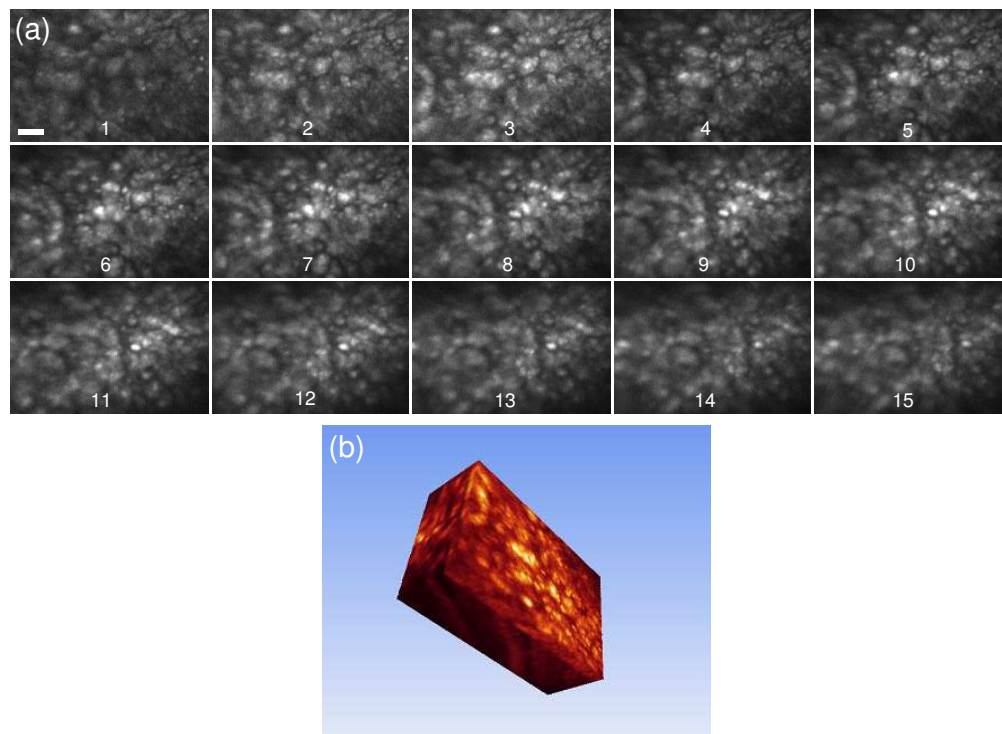


Fig. 5.32: (a) A series of *in vitro* images of the humanu-87 MG glioblastoma tissue obtained by a nonlinear optical endoscope. Each section is recorded at an axial step of  $5 \mu\text{m}$  into the sample. The scale bar is  $20 \mu\text{m}$ . (b) 3D visualisation of the breast cancer tissue.



## 5.6 Chapter conclusions

This chapter has demonstrated experimentally the concept of nonlinear optical endoscopy using a double-clad PCF, a MEMS mirror, and a GRIN lens. A double-clad PCF, custom-manufactured by Crystal Fibre A/S, has been proposed to modify the originally active double-clad PCF. This double-clad PCF plays a dual role to offer the robust single-mode guidance of near infrared light in the central core and the efficient propagation of visible light within the multimode inner cladding. The double-clad PCF exhibits a degree of polarisation of approximately 0.84 in the core as well as a delivery efficiency of up to 90% through the core and the inner cladding.

Both TPEF and SHG signals can be simultaneously collected in a microscope using the double-clad PCF with axial resolution of  $2.8 \mu\text{m}$  and  $2.5 \mu\text{m}$ , respectively. More importantly, signal levels of nonlinear optical microscopy using a double-clad PCF has been significantly improved by approximately two orders of magnitude (40 times) in comparison with those in an SMF-based microscope. This feature is confirmed by 3D high-resolution nonlinear optical images obtained from a fish scale and rat tail tendon. Investigations into the SHG polarisation measurement in a double-clad PCF-based microscope show that the microstructures in the inner cladding of the PCF result in a depolarisation effect of the nonlinear optical signals.

A nonlinear optical endoscope has been constructed by use of a double-clad PCF to improve the detection efficiency, a MEMS mirror to steer the light at the fibre tip, and a GRIN lens to produce a focus spot. Combined with a double-clad PCF, a nonlinear optical microscope based on a GRIN lens can achieve simultaneous optimisations of signal level and axial resolution. This effect overcomes the trade-off issue between signal level and axial resolution in nonlinear optical microscopy using an SMF and a GRIN lens. As a result, the signal level in the system using a double-clad PCF and a GRIN lens is enhanced by approximately 160 times compared with that in the SMF-GRIN lens-based microscope.

MEMS mirrors based on electrothermal bimorph actuation have been demonstrated

their effectiveness in nonlinear optical imaging. The nonlinear optical endoscope using a double-clad PCF, a MEMS mirror, and a GRIN lens exhibits a consistent contrast pattern with an SMF-scanning stage-based system, confirmed by images of fluorescence microspheres. In particular, axial resolution of the nonlinear optical endoscope is approximately  $10\ \mu\text{m}$  and signal level is enhanced by approximately 120 times.

Potential applications of the nonlinear optical endoscope in biomedicine have been demonstrated by series of nonlinear optical imaging performed with rat tail tendon, gastrointestinal tract tissue, oral cavity tissue, and cancer tissue. 3D high-resolution images have been demonstrated with an imaging depth of up to  $100\ \mu\text{m}$ . This technology will enable visualisations of functional and morphological changes of tissue at the microscopic level rather than direct observations with a traditional instrument at the macroscopic level. It is a complement for conventional multi-photon microscopy and optical coherent tomography. Furthermore, it can complement other endoscopic imaging and enable optical biopsy for early cancer detection.

# Chapter 6

## Nonlinear optical microscopy using a double-clad photonic crystal fibre coupler

### 6.1 Introduction

We have demonstrated that the double-clad photonic crystal fibre (PCF) is ideally suitable for nonlinear optical endoscopy due to its dual function of single-mode and multimode delivery through the central core and the inner cladding region with a high NA, respectively, within a single piece of fibre. The signal level of the nonlinear optical endoscopy based on the double-clad PCF is approximately two orders of magnitude higher than that using a standard single-mode fibre. Although the dual function of the double-clad fibre enables miniature and flexible endoscope probes, a further compact imaging system could be achieved by use of a multiport fibre coupler to gain self-alignment and replace bulk optics for an all-fibre microscopy system, as the geometry that has been shown in Chapter 3. However, there has been no report on the fabrication of a double-clad PCF coupler as well as its applications.

Recent theoretical study and fabrication of PCF couplers have been reported for a number of PCF structures [150–153]. The side-polished method has been used to produce a single-mode PCF coupler with a tunable splitting ratio [152]. By removing a part of the cladding region of each PCF, two PCFs were mated close enough to achieve evanescent field coupling through the sides of the PCFs. In addition, the fused biconical taper method has been successful in generating single-mode and multimode air-silica PCF couplers according to the principle of mode expansion [151, 153]. In particular, the multiport multimode air-clad holey fibre coupler can deliver optical power of up to 35 W at wavelength 850 nm [153]. Compared with the polishing method [152], the fused biconical taper method can protect the complicated structures of PCFs with a more maneuverable fabrication process [151, 153].

The difficulty in fabricating a double-clad PCF coupler is to achieve mode coupling through two cladding regions and preserve the single-mode and multimode guidance in the core and inner cladding regions, respectively. In particular, for applications in nonlinear optical microscopy, one arm of the double-clad PCF coupler should permit the single-mode propagation of a near infrared laser beam in the core, while the other arm can facilitate the multimode collection of the visible nonlinear optical signals. In this chapter, a three-port double-clad PCF coupler is fabricated by the fused tapered method, showing the single-mode and multimode separation at different wavelengths. A compact nonlinear optical microscope is implemented by this PCF coupler and a GRIN lens, demonstrating high-resolution three-dimensional (3D) two-photon excited fluorescence (TPEF) and second harmonic generation (SHG) images.

The structure of the chapter is as follows. The coupler by use of double-clad PCFs for nonlinear optical microscopy is fabricated and characterised in Section 6.2. A particular attention is given to the splitting ratio and the mode propagation of the PCF coupler. The splitting ratio of a double-clad PCF coupler can be designed specifically to optimise the detection efficiency for nonlinear optical imaging in the future research. In conjunction with a GRIN lens, the fabricated double-clad PCF coupler is used to construct a miniaturised nonlinear optical microscope in Section 6.3. Section 6.4

presents the axial and 3D imaging performance of TPEF and SHG in the compact all-fibre microscope, followed by the chapter conclusions in Section 6.5.

## 6.2 A double-clad PCF coupler

### 6.2.1 Fabrication process

As pointed out in Section 6.1, the fused taper method facilitates the coupling of single-mode and multimode PCFs. Consequently, it is adopted to make a double-clad PCF coupler. The geometry and optical properties of the double-clad PCF we used for fabricating a coupler has been presented in Section 5.2. Fig. 6.1 illustrates the fabrication process of the double-clad PCF coupler proposed for nonlinear optical microscopy. Two lengths of the double-clad PCFs are first twisted, heated by a hydrogen flame with a flame size of approximately 10 mm, and then drawn gradually in the fused region. The temperature and the size of the flame can be controlled by adjustment of the gas-flow rate. The fabrication of the PCF coupler was conducted in Fovice in Korea.

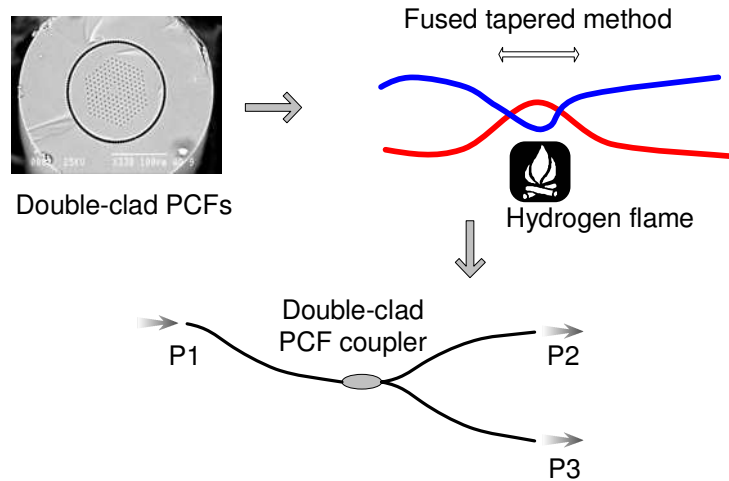


Fig. 6.1: Schematic diagram of the fabrication process of the double-clad PCF coupler.

Acrylate coating is removed only in the fusion region. As the fibres are elongated

and the fibre diameter is reduced, mode coupling occurs if the confined mode field in a PCF is extended to its neighboring double-clad PCF. Further, it is important to control the pulling length in the fused region, as it determines the splitting ratio of the coupler as well as the mode coupling condition in the core and cladding regions. In the case of the short pulling length, where the rings of air holes in two fibres are very close or partially collapsed, the multimode in the inner cladding is coupled to the neighboring fibre. Light propagated in the outer cladding leaks out quickly beyond the fusion region where the acrylate coating is still remained. The length that yields 1% coupling is defined as the coupling-starting pulling length. In the fabrication system various coupling-starting pulling lengths for the coupler are obtained, at which one arm of the coupler is terminated to form a  $1 \times 2$  PCF coupler.

## 6.2.2 Propagation property

Like the single-mode fibre coupler and the double-clad PCF we have used in Chapters 3 and 5, it is of significance to characterise the propagation property of the fibre-optic devices under various operation conditions before it is applied to nonlinear optical microscopy. For a double-clad PCF coupler of the coupling-starting pulling length of approximately 6.1 mm, its coupling efficiency is measured from ports 2 and 3 (see Fig. 6.1), while a laser beam in the wavelength range 532 – 870 nm is coupled to port 1. The light sources at different wavelengths are obtained in the same way that has been described in Section 3.2.1.

As shown in Fig. 6.2, the coupling efficiencies at ports 2 and 3 are approximately 2.2% and 77.5%, respectively, with a splitting ratio of 97/3 between ports 3 and 2 over the visible and near infrared wavelength range. Under this condition, the coupler reveals a low insertion loss of 1.1 dB between ports 1 and 3, while the insertion loss is as high as 16.6 dB between ports 1 and 2. The coupling efficiency of this coupler is different from that of a single-mode fibre coupler (see Figs. 3.2 and 3.3), which exhibits a lower coupling efficiency at port 3 in the visible wavelength region.

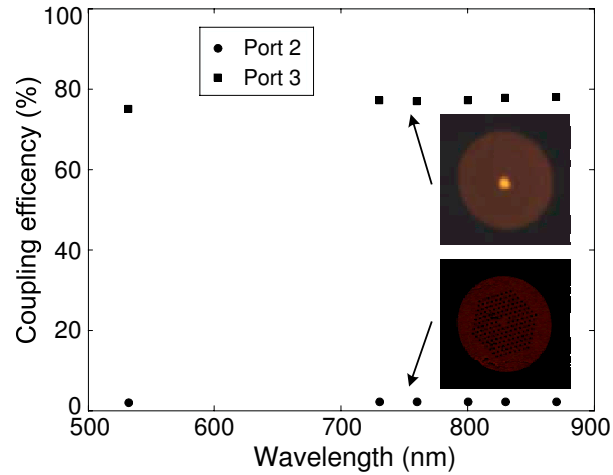


Fig. 6.2: Coupling efficiency at output ports 2 and 3 of the double-clad PCF fibre coupler having a coupling-starting pulling length of 6.1 mm as a function of the illumination wavelength at input port 1. Insets, digital camera photographs of output patterns of the double-clad PCF coupler at wavelength 800 nm.

It has been shown in Section 5.3.2 that a single-mode laser beam in the central core of the double-clad PCF makes a significant contribution to the excitation of nonlinear optical signals. Therefore it is essential to confirm the single-mode delivery feature of the double-clad PCF coupler. To this end, output patterns at ports 2 and 3 of the same coupler are recorded by a camera and are shown in the insets of Fig. 6.2 when port 1 is illuminated at wavelength 800 nm. It can be seen that the arm (port 3) guiding the most power of the laser beam still maintains the single-mode propagation in the central core, whereas only the multimode propagation is observed from the other arm (port 2) in the near infrared wavelength range. This result, together with the splitting ratio shown in Fig. 6.2, implies that using port 3 for the delivery of the pulsed excitation beam and port 2 for the visible signal collection facilitates the feature of the efficient single-mode propagation in the core and the multimode collection through the inner cladding. This unique feature, which cannot be obtained from a single-mode fibre coupler, may prove advantageous for compact all-fibre nonlinear optical microscopy.

It should be pointed out that a double-clad PCF coupler having a longer coupling-starting pulling length shows a higher splitting ratio, which is demonstrated in Fig. 6.3. This coupler has coupling efficiencies of approximately 20% and 6.5% at

ports 3 and 2, respectively, with a splitting ratio of 74/26 between them in the near infrared wavelength range. Compared with the coupler having a shorter coupling-starting pulling length (Fig. 6.2), this coupler exhibits a higher excess loss of 5.8 dB. Furthermore, the measurement of the output patterns shows that the multimode guidance of the laser beam at a near infrared wavelength is observed at both ports (insets of Fig. 6.3). As a result, this coupler leads to an inefficient performance of a nonlinear optical microscope if it is used to deliver the laser beam for excitation. This outcome might be due to the complete collapse of air holes surrounding the fibre core in the fused region.

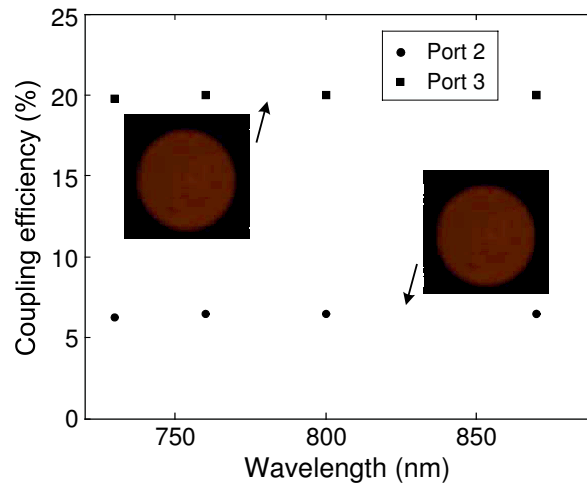


Fig. 6.3: Coupling efficiency at output ports 2 and 3 of the double-clad PCF fiber coupler having a longer coupling-starting pulling length as a function of the illumination wavelength at input port 1. Insets, digital camera photographs of output patterns of the double-clad PCF coupler at wavelength 800 nm.

### 6.2.3 Splitting ratio optimisation

The splitting ratio of a PCF coupler plays an important role in the efficiency of the excitation delivery and the signal collection. In particular, the nonlinear dependence of emitted signals on the excitation power in the nonlinear optical processes gives rise to a nonlinear dependence of the splitting ratio on the detected signals by the PCF coupler. Therefore, the splitting ratio of the PCF coupler can be specifically designed to maximise the detected strength of nonlinear signals.



Let us consider a three-port fibre coupler with a splitting ratio of  $x/(1-x)$  if the loss at the junction and the wavelength dependence is neglected, as shown in Fig. 6.4(a). Here  $x$  and  $(1-x)$  are the coupling ratios in the excitation and signal arms, respectively. The coupling efficiency between two ports of the coupler is linearly dependent on the coupling ratios  $x$  and  $(1-x)$ . For an  $n$ -photon excitation process, if the splitting ratio is consistent at excitation and emission wavelengths, the detected fluorescence intensity can be given by

$$I_f \propto I_i^n x^n (1-x) . \quad (6.1)$$

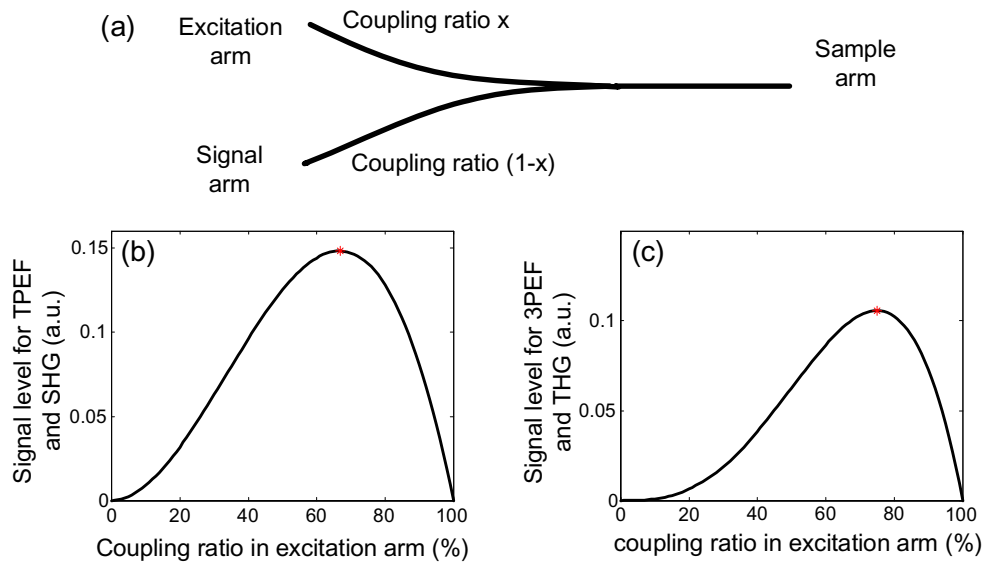


Fig. 6.4: (a) Scheme diagram of a three-port coupler with a splitting ratio of  $x/(1-x)$ . (b)-(c) Detected nonlinear signal intensity as a function of coupling ratio in the excitation arm in two- and three-photon processes, respectively.

Fig. 6.4(b) depicts the detected nonlinear signal intensity as a function of the coupling ratio in the excitation arm in the case of TPEF or SHG processes. It can be observed that the optimised splitting ratio between the excitation arm and the signal arm is 67/33. In the case of three-photon excited fluorescence (3PEF) or third harmonic generation (THG) processes shown in Fig. 6.4(c), the optimised splitting ratio between the excitation arm and the signal arm is 75/25.

Indeed, the PCF coupler that has been integrated to the nonlinear imaging or sensor system should be fabricated according to the above design to maximise the detection

efficiency. However, it was difficult to control the splitting ratio as well as the mode profiles in the fabrication process.

### 6.3 Experimental arrangement

We construct an all-fibre nonlinear optical microscope based on the double-clad PCF coupler (shown in Fig. 6.2) and a GRIN lens, which is depicted in Fig. 6.5. A turnkey Ti:Sapphire (Spectra Physics, Mai Tai) of the wavelength range between 730 nm and 870 nm provides short pulses with a pulse width of 80 fs and a repetition rate of 80 MHz. The laser beam is prechirped by double passing a pair of gratings (Newport, 1200 grooves/mm,  $28.7^\circ$  blaze angle) before they are coupled to port 3 of the fibre coupler with a  $4\times/0.12$  NA objective, CO. For a double-clad PCF fibre with a length of 1 meter, negative prechirping of approximately  $-32200 \text{ fs}^2$  is required to compensate for the group velocity dispersion in the fused silica material. Such a dispersion compensation arrangement leads to an improvement of the nonlinear optical signal level by a factor of approximately 11 for a given average power ( $<10 \text{ mW}$ ).

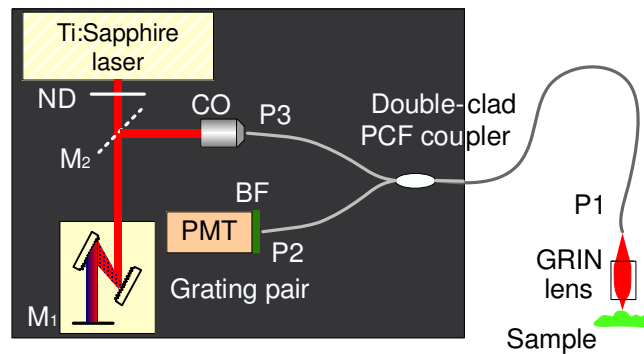


Fig. 6.5: Schematic diagram of the nonlinear optical microscope with a three-port double-clad PCF coupler and a GRIN lens. Mirror  $M_2$  (shown dashed) is located on a different plane from Mirror  $M_1$ . ND: neutral density filter, BF: bandpass filter, CO: coupling objective.

The output laser beam at port 1 is focused through a 1-mm-diameter, 0.2-pitch, 0.5-NA GRIN lens (GRINTECH) onto a sample. The excited nonlinear optical signals from the sample are collected via the detection arm (port 2) of the coupler attached

to a PMT (photomultiplier tube). Therefore, the double-clad PCF coupler acts as a beam splitter to separate the nonlinear optical signals from the excitation laser beam delivered by the fibre core. Furthermore, a coupling objective with a low NA (0.07 or 0.12) can be used to maximise the excitation power delivered in the fibre core without the combination of an iris diaphragm and a high NA coupling objective (see Fig. 5.5), which collects the backward signals through a single piece of double-clad PCF. In this case, the delivered power in the fibre core can be 50 mW for nonlinear excitation.

## 6.4 System performance

### 6.4.1 Axial resolution

To characterise the depth discrimination of the fibre-optic nonlinear optical microscope using a double-clad PCF coupler, we measure the TPEF axial response to a thin layer of AF-50 dye. According to the previous study shown in Fig. 5.13, axial resolution and signal level of the system are dependent on the gap length between the fibre and the back surface of the GRIN lens. As a result, a gap length of approximately 8 mm is chosen to optimise the signal level of the system. A typical TPEF axial response to

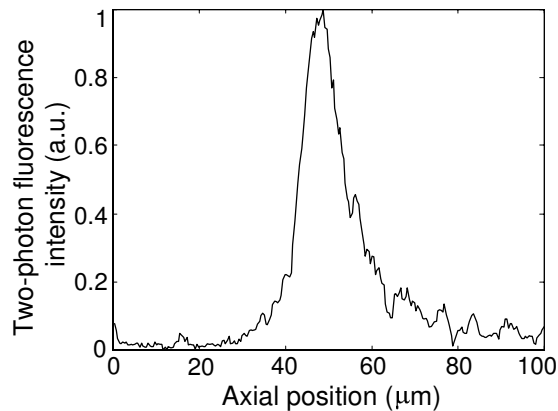


Fig. 6.6: TPEF axial response to a thin layer of AF-50 dye in a nonlinear optical microscope using a double-clad PCF coupler and a GRIN lens. The excitation wavelength is 800 nm.

the thin layer is presented in Fig. 6.6, revealing the axial resolution of approximately  $10\ \mu\text{m}$  in the nonlinear optical microscope. This value is consistent with the result we have obtained with a double-clad PCF and the same GRIN lens (Fig. 5.13(b)). A slight improvement of axial resolution can be achieved when the back aperture of the GRIN lens is overfilled. However, it results in an approximately 25% degradation of the signal level of the system.

### 6.4.2 Nonlinear optical imaging

The optical sectioning ability of the new system is further demonstrated by sets of TPEF images of  $10\ \mu\text{m}$  diameter microspheres and SHG images of KTP crystal powder, which are displayed in Figs. 6.7(a) and (b), respectively. It can be seen that the

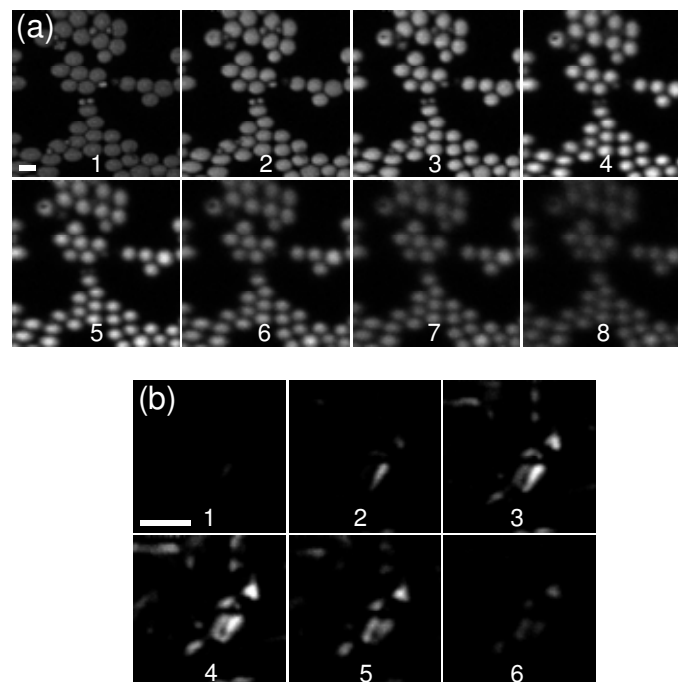


Fig. 6.7: (a) TPEF image sections of  $10\ \mu\text{m}$  diameter fluorescent microspheres and (b) SHG image sections of KTP crystal powder. Each set of images has an axial depth of  $5\ \mu\text{m}$  into the sample. The excitation wavelength is  $800\ \text{nm}$  and a  $400/9\ \text{nm}$  bandpass filter is placed before the PMT when SHG images are acquired. The excitation power is approximately  $10\ \text{mW}$  on the sample. Scale bars represent  $10\ \mu\text{m}$ .

system can collect high-resolution 3D images so that defects in the microspheres are well visualised. The results also imply that the miniature microscope could be used as a probe for the simultaneous detection of TPEF and SHG signals in tumour tissue. Furthermore, compared with the images obtained with a single-mode fibre coupler and a GRIN lens shown in Fig. 3.20, the signal level of the images obtained with the new system is improved by a factor of approximately 5 due to the simultaneous optimisations of signal level and axial resolution in a nonlinear optical microscope using a double-clad PCF and a GRIN lens.

## 6.5 Chapter conclusions

A  $1 \times 2$  double-clad PCF coupler has been designed and fabricated using the fused tapered method (Fovice, Korea), showing a low excess loss of approximately 1 dB and a splitting ratio of 97/3 over the entire visible and near infrared wavelength range. In addition to the property of splitting the laser power, the double-clad feature of the coupler facilitates the separation of a near infrared single-mode beam in the core from a visible multimode beam in the inner cladding region, which is ideal for nonlinear optical microscopy imaging. Investigations into the coupler fabrication show that the parameters of a double-clad PCF coupler such as the splitting ratio, the excess loss, and the mode propagation, rely on the coupling-starting pulling length of the coupler. Furthermore, it has been theoretically explored that the splitting ratio of a PCF coupler can be specifically designed to optimise the detection efficiency of a nonlinear optical microscope.

A compact nonlinear optical microscope has been constructed with the double-clad PCF coupler and a GRIN lens, giving rise to the axial resolution of approximately  $10 \mu\text{m}$ . 3D TPEF and SHG images demonstrate potential applications of the coupler to all-fibre nonlinear optical microscopy and endoscopy. Since double-clad PCFs are extensively used in laser sources, the effectiveness of the double-clad PCF coupler may result in future interest in this area. Such an instrument can therefore be useful for

side pumped double-clad microstructure fibre lasers and amplifiers to leave the fibre ends free for splicing to other fibres as well as enable compact devices [154].

# Chapter 7

## Conclusion

### 7.1 Thesis conclusions

The main research work in this thesis provides a detailed and comprehensive insight into the development and the imaging performance of fibre-optic nonlinear optical microscopy and endoscopy that is a novel modality in the field of optical imaging. Four major areas of research have been explored both experimentally and theoretically and concentrated in the following key areas.

1. Design, construction and characterisation of a fibre-optic nonlinear optical microscope using a single-mode fibre (SMF) coupler and a gradient index (GRIN) lens. It is the first demonstration of fibre-optic nonlinear optical microscopy, which uses multiple imaging modalities including two-photon excited fluorescence (TPEF) and second harmonic generation (SHG).
2. Theoretical analysis of the three-dimensional (3D) coherent transfer function (CTF) for a SHG microscope using an SMF.
3. Introduction of a new type of the double-clad photonic crystal fibre (PCF) for efficient nonlinear optical microscopy and formation of a fibre-optic nonlinear

optical endoscope with a microelectromechanical system (MEMS) mirror and a GRIN lens. The signal level of the endoscope is thus enhanced by two orders of magnitude.

4. Design, creation and application of a double-clad PCF coupler for compact nonlinear optical microscopy.

An investigation into the feasibility of applying an SMF coupler to both TPEF and SHG microscopy for excitation delivery and signal collection has been conducted through a series of comprehensive characterisation experiments. It has been found that the coupling efficiency for both pulsed and continuous wave illumination beams delivered by the SMF coupler is 20 – 41% in the wavelength range of 400 – 870 nm. The fibre coupler has an equal splitting ratio at a near infrared wavelength, whereas it acts as a low-pass spectral filter in the visible wavelength range with a splitting ratio between 99.6/0.4 and 99.7/0.3. In particular, the degree of polarisation of approximately 1 is obtained at an angular interval of approximately 90 degrees of the incident polarisation angle over the broad wavelength range, exhibiting an ideal feature desirable in SHG microscopy.

A nonlinear optical microscope using TPEF and SHG has been constructed with an SMF coupler. The fibre coupler enables the delivery of ultrashort-pulsed laser at a near infrared wavelength as well as the efficient collection of simultaneous TPEF and SHG signals in the visible wavelength range. The performance of axial resolution of the system has shown that the shorter wavelength of SHG emission results in an improvement in axial resolution compared with that of TPEF under the same excitation condition. More importantly, a complete characterisation of the SHG polarisation anisotropy through the SMF coupler has been undertaken with various well-defined samples. It has been demonstrated that polarised SHG signals can be excited and collected through the fibre coupler to analyse the molecular orientations of structural proteins. This feature, together with the TPEF imaging capability, can provide the complementary information of the molecular distributions and organisations in the



sample.

An integration of a GRIN lens results in a further compact fibre-optic nonlinear optical microscope. It has been found that the axial resolution and signal level of the system based on an SMF and a GRIN lens are significantly dependent on the gap length between them. The collected nonlinear signal intensity exhibits a peak as the gap between the fibre coupler end and the GRIN lens enlarges to increase the effective numerical aperture (NA) of a GRIN lens. The optimised axial resolution of the system is approximately  $11.6 \mu\text{m}$  for a GRIN lens of an NA of 0.46. The imaging performance in such a system can be adjusted by setting the fibre-GRIN lens spacing. However, the high resolution comes at the expense of signal level.

The performance of fibre-optic SHG microscopy using an SMF has been analysed through the formalisation of the 3D CTF, which gives a complete description of the coherent imaging system. The ability of the system to resolve the high spatial frequency information has been investigated for a range of fibre parameters. It has been shown that the performance of fibre-optic SHG microscopy behaves as confocal SHG microscopy, when the NA of the fibre is much larger than the convergence angle of the illumination on the fibre aperture. In particular, the axial resolution performance has also been investigated by calculating the modulus squared of the Fourier transform of the axial cross section of the 3D CTF at  $l = 0$ . Both experimental and theoretical results reveal that the optical sectioning effect in fibre-optic SHG microscopy is enhanced by approximately 7% compared with that in fibre-optic TPEF microscopy. In addition, the effect of fibre parameters on the detected signal intensity has been qualitatively analysed.

Low signal level in an SMF-based nonlinear optical microscope is a bottle-neck issue, which makes it impossible to image tissue samples under *in vitro* and *in vivo* conditions. In order to break the limit of the signal level in miniature nonlinear optical microscopy, a double-clad PCF has been introduced to play a dual function, with which the single-mode guidance of a near infrared beam in the central core and the efficient propagation of a visible beam within the multimode inner cladding have been realised.

A coupling efficiency of up to 90% in the wavelength range between 410 nm and 800 nm is achievable. The effect of a double-clad PCF on the signal level enhancement in a nonlinear optical microscope has been demonstrated through the comparison with a nonlinear optical microscope using an SMF. It has been shown that the signal level has increased by a factor of approximately 40 as a consequence of the large collection area and the high NA of the double-clad PCF. Furthermore, the performance of a double-clad PCF for 3D high-resolution nonlinear optical imaging has been succeeded in terms of the ability to generate TPEF and SHG optical sections. SHG polarisation anisotropy measurement with a double-clad PCF has shown that the degree of polarisation of 0.84 can be preserved in the central core at wavelength 800 nm, whereas the microstructures in the inner cladding results in a depolarisation effect for the backward SHG signals.

This new knowledge above has led to the design and construction of a nonlinear optical endoscope using the double-clad PCF, a MEMS mirror and a GRIN lens. The combination of a double-clad PCF and a GRIN lens leads to the simultaneous optimisations of axial resolution and signal level in fibre-optic nonlinear optical microscopy. This feature results in the axial resolution of approximately 6  $\mu\text{m}$  for nonlinear optical imaging as well as the signal level enhancement of 160 times compared with the system based on an SMF coupler and a GRIN lens.

The performance of this new nonlinear optical endoscope is further enhanced by the adoption of a MEMS mirror based on electrothermal bimorph actuation. The nonlinear optical microscope has been characterised by a series of comprehensive tissue imaging experiments. It has been shown that the axial resolution of the nonlinear optical endoscope is approximately 10  $\mu\text{m}$  and that the signal level is enhanced by approximately 120 times compared with an SMF-scanning stage-based system. The potential applications of the nonlinear optical endoscope to biomedical imaging have been demonstrated by 3D visualisations of nonlinear optical imaging in various gastrointestinal tissue, oral cavity tissue, and cancer tissue. These experimental results give the first demonstration of 3D high-resolution tissue imaging through a miniature nonlinear optical microscope.

The design of the fibre-optic nonlinear optical endoscope has been further simplified by a  $1 \times 2$  double-clad PCF coupler, which combines the advantages of an SMF coupler and a double-clad PCF to demonstrate a concept of all-fibre nonlinear optical microscopy/endoscopy. The ability of the double-clad PCF coupler to transmit light over the entire visible and near infrared wavelength ranges has been demonstrated by a low excess loss of approximately 1 dB and a splitting ratio of 97/3. The ability of the double-clad PCF coupler to form a nonlinear optical microscope has also been demonstrated by the separation of the near infrared single-mode beam in the core from the visible multimode beam in the inner cladding region. Further, 3D TPEF and SHG images through the double-clad PCF coupler and the GRIN lens have been achieved.

In conclusion, the research work conducted in this thesis has demonstrated a new horizon for nonlinear optical endoscopy. Imaging modalities of both TPEF and SHG have been demonstrated in fibre-optic nonlinear optical microscopy and endoscopy based on a double-clad PCF, a MEMS mirror, and a GRIN lens. The signal level of fibre-optic nonlinear optical endoscopy has been significantly enhanced by two orders of magnitude. As a result, 3D nonlinear optical endoscopic imaging through tissue has become possible. Taking advantages of compact size and high resolution, fibre-optic nonlinear optical endoscopy developed in this thesis can produce an imaging tool with new functionalities, high resolution, and multiple imaging mechanisms, which significantly complement conventional optical imaging modalities such as optical coherent tomography for *in vivo* imaging in biomedical applications.

## 7.2 Future work

The research investigation described in this thesis can be further extended to include the following key areas to provide the additional functionality and enhancement of fibre-optic nonlinear optical microscopy and endoscopy.

### 7.2.1 Engineering of a double-clad PCF

As we have pointed out in Chapter 2, one important feature of PCFs is that the dispersion property of the fibre can be controlled by the 2D photonic crystal structures running along the fibre length. By modifying the profile of the photonic crystal structures, both the magnitude and the sign of the dispersion can be tailored to suit specific applications [78, 82, 107]. Therefore, the dispersion engineering of the double-clad PCF can shift the zero-dispersion wavelength of the fibre to the operation spectral window of a femtosecond Ti:Sapphire laser. Furthermore, supercontinuum generation spanning the visible and the near infrared wavelength range may also be feasible using a Ti:Sapphire laser [108–110, 112]. At the same time, a careful design of the fibre structures should maintain the high NA of the inner cladding. Fig. 7.1 shows the schematic diagram of the new-designed double-clad PCF and its schematic profile of refractive index. The effective refractive indices in the core and inner cladding can be obtained by the arrangement of air holes, which may be ordered in different patterns and shapes. Values of the air-hole diameter and the hole-to-hole spacing in the inner cladding ( $d, \Lambda$ ) and in the outer cladding ( $d', \Lambda'$ ) can be adjusted to generate the refractive index profile required by the engineered double-clad PCF.

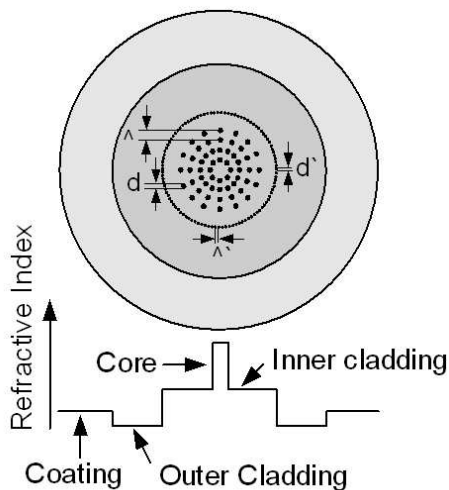


Fig. 7.1: Schematic transverse cross-section of an engineered double-clad PCF. The profile of effective refractive index is shown at the bottom of the figure.

This technology can provide new opportunities for PCF devices and have a significant impact on their applications to nonlinear optical endoscopy. Thus the engineered double-clad PCF can combine the advantages of dispersion management and high detection efficiency to provide next generation nonlinear optical endoscopy that enables multispectral channels for the simultaneous excitation of multiple image modalities and the efficient collection for multicolour images.

### **7.2.2 *In vivo* tissue imaging**

A nonlinear optical endoscope can be mechanically integrated into a home-built probe and perform *in vivo* imaging with intact animals. Such a nonlinear optical endoscope can be used in internal organs, such as colon, esophagus, stomach, oral cavity, and cervix. Since different biological species are responsible for different nonlinear optical processes, it is possible to achieve multicolor imaging, for example, two-photon fluorescence from elastin, three-photon fluorescence from tryptophan, second harmonic generation from collagen, and third harmonic generation from lipid bodies. It is expected that nonlinear optical endoscopy will enable the simultaneous detection of multiple nonlinear optical imaging modalities, which represents the versatile biological information carried by different emission wavelengths. The *in vivo* tissue imaging capability may add to a new dimension for optical biopsy and early cancer detection.

# Bibliography

- [1] D. J. Stephens and V. J. Allan. Light microscopy techniques for live cell imaging. *Science*, **300**:82–86, 2003.
- [2] R. Yuste. Fluorescence microscopy today. *Nat. Methods*, **2**:902–904, 2005.
- [3] M. Minsky. Memoir on inventing the confocal scanning microscope. *Scanning*, **10**:128–138, 1988.
- [4] J. Conchello and J. W. Lichtman. Optical sectioning microscopy. *Nat. Methods*, **2**:920–931, 2005.
- [5] W. Denk, J. H. Strickler, and W. W. Webb. Two-photon laser scanning fluorescence microscopy. *Science*, **248**:73–75, 1990.
- [6] R. M. Williams, W. R. Zipfel, and W. W. Webb. Multiphoton microscopy in biological research. *Current Opinion in Chemical Biology*, **5**:603–608, 2001.
- [7] W. R. Zipfel, R. M. Williams, and W. W. Webb. Nonlinear magic: multiphoton microscopy in the biosciences. *Nat. Biotech.*, **21**:1369–1377, 2003.
- [8] F. Helmchen and W. Denk. Deep tissue two-photon microscopy. *Nat. Methods*, **2**:932–940, 2005.
- [9] E. B. Brown, R. B. Campbell, Y. Tsuzuki, L. Xu, P. Carmeliet, D. Fukumura, and R. K. Jain. *In vivo* measurement of gene expression, angiogenesis and physiological function in tumors using multiphoton laser scanning microscopy. *Nat. Medicine*, **7**:864–868, 2001.

- [10] R. K. Jain, L. L. Munn, and D. Fukumura. Dissecting tumor pathophysiology using intravital microscopy. *Nat. Rev. Cancer*, **2**:266–275, 2002.
- [11] J. Condeelis and J. E. Segall. Intravital imaging of cell movement in tumors. *Nat. Rev. Cancer*, **3**:921–930, 2003.
- [12] S. A. Boppart, T. F. Deutsch, and D. W. Rattner. Optical imaging technology in minimally invasive surgery. *Surg. Endosc.*, **13**:718–722, 1999.
- [13] H. Furihata. New technologies in endoscopic surgery. *Min. Invas. Ther. & Allied. Technol.*, **10**:199–203, 2001.
- [14] M. George. Optical methods and sensors for in situ histology in surgery and endoscopy. *Min. Invas. Ther. & Allied. Technol.*, **13**:95–104, 2004.
- [15] C. Xu, W. Zipfel, J. B. Shear, R. M. Williams, and W. W. Webb. Multiphoton fluorescence excitation: New spectral windows for biological nonlinear microscopy. *Proc. Natl. Acad. Sci. USA*, **93**:10763–10768, 1996.
- [16] P. J. Campagnola, M. Wei, A. Lewis, and L. M. Loew. High-resolution nonlinear optical imaging of live cells by second harmonic generation. *Biophys. J.*, **77**:3341–3349, 1999.
- [17] P. J. Campagnola, A. C. Millard, M. Terasaki, P. E. Hoppe, C. J. Malone, and W. A. Mohler. Three-dimensional high-resolution second-harmonic generation imaging of endogenous structural proteins in biological tissues. *Biophys. J.*, **81**:493–508, 2002.
- [18] P. J. Campagnola and L. M. Loew. Second harmonic imaging microscopy for visualizing biomolecular arrays in cells, tissues and organisms. *Nat. Biotech.*, **21**:1356–1360, 2003.
- [19] Y. R. Shen. *The Principles of Nonlinear Optics*. J. Wiley, New York, 1984.
- [20] J. X. Cheng and X. S. Xie. Coherent anti-stokes Raman scattering microscopy: Instrumentation, theory, and applications. *J. Phys. Chem. B*, **108**:827–840, 2004.

- [21] A. T. Yeh, N. Nassif, A. Zoumi, and B. J. Tromberg. Selective corneal imaging using combined second-harmonic generation and two-photon excited fluorescence. *Opt. Lett.*, **27**:2082–2084, 2002.
- [22] A. Zoumi, A. Yeh, and B. J. Tromberg. Imaging cells and extracellular matrix *in vivo* by using second-harmonic generation and two-photon excited fluorescence. *Proc. Natl. Acad. Sci. USA*, **99**:11014–11019, 2002.
- [23] W. E. Zipfel, R. M. Williams, R. Christie, A. Y. Nikitin, B. T. Hyman, and W. W. Webb. Live tissue intrinsic emission microscopy using multiphoton-excited native fluorescence and second harmonic generation. *Proc. Natl. Acad. Sci. USA*, **100**:7075–7080, 2003.
- [24] A. Zoumi, X. Lu, G. S. Kassab, B. J. Tromberg. Imaging coronary artery microstructure using second-harmonic and two-photon fluorescence microscopy. *Biophys. J.*, **87**:2778–2786, 2004.
- [25] F. Helmchen, M. S. Fee, D. W. Tank, W. Denk. A miniature head-mounted two-photon microscope: High-resolution brain imaging in freely moving animals. *Neuron*, **31**:903–912, 2001.
- [26] D. Bird and M. Gu. Compact two-photon fluorescence microscope based on a single-mode fiber coupler. *Opt. Lett.*, **27**:1031–1033, 2002.
- [27] D. Bird and M. Gu. Two-photon fluorescence endoscopy with a micro-optic scanning head. *Opt. Lett.*, **28**:1552–1554, 2003.
- [28] J. C. Jung and M. J. Schnitzer. Multiphoton endoscopy. *Opt. Lett.*, **28**:902–904, 2003.
- [29] W. Göbel, J. N. D. Kerr, A. Nimmerjahn, and F. Helmchen. Miniaturized two-photon microscope based on a flexible coherent fiber bundle and a gradient-index lens objective. *Opt. Lett.*, **29**:2521–2523, 2004.
- [30] M. T. Myaing, D. J. MacDonald, and X. Li. Fiber-optic scanning two-photon fluorescence endoscope. *Opt. Lett.*, **31**:1076–1078, 2006.



- [31] G. P. Agrawal. *Nonlinear Fiber Optics*. Academic, San Diego, 1989.
- [32] L. Fu, A. Jain, H. Xie, C. Cranfield, and M. Gu. Nonlinear optical endoscopy based on a double-clad photonic crystal fiber and a MEMS mirror. *Opt. Express*, **14**:1027–1032, 2006.
- [33] M. V. Irvani. Fibre-optic scanning differential interference contrast optical microscope. *Electron. Lett.*, **22**:103–105, 1986.
- [34] S. Kimura and T. Wilson. Confocal scanning optical microscope using single-mode fiber for signal detection. *Appl. Opt.*, **30**:2143–2150, 1991.
- [35] T. Dabbs and M. Glass. Fibre-optic confocal microscope: FOCON. *Appl. Opt.*, **31**:3030–3035, 1992.
- [36] A. R. Rouse, A. Kano, J. A. Udovich, A. M. Kroto, A. F. Gmitro. Design and demonstration of a miniature catheter for a confocal microendoscope. *Appl. Opt.*, **43**:5763–5771, 2004.
- [37] A. D. Mehta, J. C. Jung, B. A. Flusberg, and M. J. Schnitzer. Fiber optic *in vivo* imaging in the mammalian nervous system. *Current Opinion in Neurobiology*, **14**:1–12, 2004.
- [38] B. A. Flusberg, E. D. Cocker, W. Piyawattanametha, J. C. Jung, E. L. M. Cheung, and M. J. Schnitzer. Fiber-optic fluorescence imaging. *Nat. Methods*, **2**:941–950, 2005.
- [39] W. Kaiser, C. G. B. Garrett. Two-photon excitation in  $\text{CaF}_2:\text{Eu}^{3+}$ . *Phys. Rev. Lett.*, **7**:229–231, 1961.
- [40] S. Singh and L. T. Brandley. Three-photon absorption in naphthalene crystals by laser excitation. *Phys. Rev. Lett.*, **12**:612–614, 1964.
- [41] S. Maiti, J. B. Shear, R. M. Williams, W. R. Zipfel, and W. W. Webb. Measuring serotonin distribution in live cells with three-photon excitation. *Science*, **275**:530–532, 1997.

- [42] R. M. Williams, J. B. Shear, W. R. Zipfel, S. Maiti, and W. W. Webb. Mucosal mast cell secretion processes imaged using three-photon microscopy of 5-hydroxytryptamine autofluorescence. *Biophys. J.*, **76**:1835–1846, 1999.
- [43] S. W. Hell, K. Bahlmann, M. Schrader, A. Soini, H. Malak, I. Gryczynski, and J. R. Lakowicz. Three-photon excitation in fluorescence microscopy. *J. Biomed. Opt.*, **1**:71–74, 1996.
- [44] X. Gan and M. Gu. Fluorescence microscopic imaging through tissue-like turbid media. *J. Appl. Phy.*, **87**:3214–3221, 2000.
- [45] M. Gu, X. Gan, A. Kisteman, and M. G. Xu. Comparison of penetration depth between two-photon excitation in imaging through turbid tissue media. *Appl. Phys. Lett.*, **77**:1551–1553, 2000.
- [46] X. Deng, X. Gan, and M. Gu. Multiphoton fluorescence microscopic imaging through double-layer turbid tissue media. *J. Appl. Phy.*, **91**:4659–4665, 2002.
- [47] P. Theer, M. T. Hasan, and W. Denk. Two-photon imaging to a depth of 1000  $\mu\text{m}$  in living brains by use of a Ti:Al<sub>2</sub>O<sub>3</sub> regenerative amplifier. *Opt. Lett.*, **28**:1022–1024, 2003.
- [48] M. Stroh, J. P. Zimmer, D. G. Duda, T. S. Levchenko, K. S. Cohen, E. B. Brown, D. T. Scadden, V. P. Torchilin, M. G. Bawendi, D. Fukumura, and R. K. Jain. Quantum dots spectrally distinguish multiple species within the tumor milieu *in vivo*. *Nat. Medicine*, **11**:678–682, 2005.
- [49] H. Wang, T. B. Huff, D. A. Zweifel, W. He, P. S. Low, A. Wei, and J. X. Cheng. *In vitro* and *in vivo* two-photon luminescence imaging of single gold nanorods. *Proc. Natl. Acad. Sci. USA*, **102**:15752–15756, 2005.
- [50] P. A. Franken, A. E. Hill, C. W. Peters, and G. Weinreich. Generation of optical harmonics. *Phys. Rev. Lett.*, **7**:118–120, 1961.
- [51] R. W. Terhune, P. D. Maker, and C. M. Savage. Optical harmonic generation in calcite. *Phys. Rev. Lett.*, **8**:404–406, 1962.

- [52] R. Hellwarth and P. Christensen. Nonlinear optical microscopic examination of structure in polycrystalline ZnSe. *Opt. Communication*, **12**:318–322, 1974.
- [53] I. Freund and M. Deutsch. Second-harmonic microscopy of biological tissue. *Opt. Lett.*, **11**:94–96, 1986.
- [54] Y. Guo, P. P. Ho, H. Savage, D. Harris, P. Sacks, S. Schantz, F. Liu, N. Zhadin, and R. R. Alfano. Optical harmonic generation from animal tissue by the use of picosecond and femtosecond laser pulses. *Opt. Lett.*, **22**:1323–1325, 1997.
- [55] R. Gauderon, P. B. Lukins, and C. J. R. Sheppard. Three-dimensional second-harmonic generation imaging with femtosecond laser pulses. *Opt. Lett.*, **23**:1209–1211, 1998.
- [56] L. Moreaux, O. Sandre, S. Charpak, M. Blanchard-Desce, and J. Mertz. Coherent scattering in multi-harmonic light microscopy. *Biophys. J.*, **80**:1568–1574, 2001.
- [57] D. A. Dombeck, K. A. Kasischke, H. D. Vishwasrao, M. Ingelsson, B. T. Hyman, and W. W. Webb. Uniform polarity microtubule assemblies imaged in native brain tissue by second-harmonic generation microscopy. *Proc. Natl. Acad. Sci. USA*, **100**:7081–7086, 2003.
- [58] Y. Barad, H. Eizenberg, M. Horowitz, and Y. Silberberg. Nonlinear scanning laser microscopy by third-harmonic generation. *Appl. Phys. Lett.*, **70**:922–924, 1997.
- [59] J. A. Squier, M. Muller, G. J. Brakenhoff, and K. R. Wilson. Third harmonic generation microscopy. *Opt. Express*, **3**:315–324, 1998.
- [60] D. Yelin and Y. Silberberg. Laser scanning third-harmonic-generation microscopy in biology. *Opt. Express*, **5**:169–175, 1999.
- [61] S. Chu, I. Chen, T. Liu, P. C. Chen, and C. Sun. Multimodal nonlinear spectral microscopy based on a femtosecond Cr:Forsterite laser. *Opt. Lett.*, **26**:1909–1911, 2001.

- [62] P. Stoller, K. M. Reiser, P. M. Celliers, and A. M. Rubenchik. Polarization-modulated second harmonic generation in collagen. *Biophys. J.*, **82**:3330–3342, 2002.
- [63] P. Stoller, B. M. Kim, A. M. Rubenchik, K. M. Reiser, and L. B. D. Silva. Polarization-dependent optical second-harmonic imaging of a rat-tail tendon. *J. Biomed. Opt.*, **7**:205–214, 2002.
- [64] T. Yasui, Y. Tohno, and T. Araki. Determination of collagen fiber orientation in human tissue by use of polarization measurement of molecular second-harmonic-generation light. *Appl. Opt.*, **43**:2861–2867, 2004.
- [65] S. W. Chu, S. Y. Chen, G. W. Chern, T. H. Tsai, Y. C. Chen, B. L. Lin, and C. K. Sun. Studies of  $\chi^{(2)}/\chi^{(3)}$  tensors in submicron-scaled bio-tissues by polarization harmonics optical microscopy. *Biophys. J.*, **86**:3914–3922, 2004.
- [66] X. Deng, E. D. Williams, E. W. Thompson, X. Gan, and M. Gu. Second-harmonic generation from biological tissues: Effect of excitation wavelength. *Scanning*, **24**:175–178, 2002.
- [67] S. Fine and W. P. Hansen. Optical second harmonic generation in biological systems. *Appl. Opt.*, **10**:2350–2353, 1971.
- [68] L. Moreaux, O. Sandre, and J. Mertz. Membrane imaging by second-harmonic generation microscopy. *J. Opt. Soc. Am. B*, **17**:1685–1694, 2000.
- [69] L. Moreaux, T. Pons, V. Dambrin, M. Blanchard-Desce, and J. Mertz. Electro-optic response of second-harmonic generation membrane potential sensors. *Opt. Lett.*, **28**:625–627, 2003.
- [70] A. C. Millard, L. Jin, A. Lewis, and L. M. Loew. Direct measurement of the voltage sensitivity of second-harmonic generation from a membrane dye in patch-clamped cells. *Opt. Lett.*, **28**:1221–1223, 2003.

- [71] A. C. Millard, L. Jin, M. Wei, J. P. Wuskell, A. Lewis, and L. M. Loew. Sensitivity of second harmonic generation from styryl dyes to transmembrane potential. *Biophys. J.*, **86**:1169–1176, 2004.
- [72] C. Sun, S. Chu, S. Chen, T. Tsai, T. Liu, C. Lin, H. Tsai. Higher harmonic generation microscopy for developmental biology. *Journal of Structural Biology*, **147**:19–30, 2004.
- [73] R. M. Williams, W. R. Zipfel, and W. W. Webb. Interpreting second-harmonic generation images of collagen I fibrils. *Biophys. J.*, **88**:1377–1386, 2005.
- [74] E. Brown, T. McKee, E. diTomaso, A. Pluen, B. Seed, Y. Boucher, and R. K. Jain. Dynamic imaging of collagen and its modulation in tumors *in vivo* using second-harmonic generation. *Nat. Medicine*, **9**:796–800, 2003.
- [75] P. D. Maker and R. W. Terhune. Study of optical effects due to an induced polarization third order in the electric field strength. *Phys. Rev.*, **137**:A801–A818, 1965.
- [76] M. Duncan, J. Reintjes, T. J. Manuccia. Scanning coherent anti-stokes Raman microscope. *Opt. Lett.*, **7**:350–352, 1982.
- [77] C. L. Evans, E. O. Potma, M. Puoris’haag, D. Cote, C. P. Lin, and X. S. Xie. Chemical imaging of tissue *in vivo* with video-rate coherent anti-stokes Raman scattering microscopy. *Proc. Natl. Acad. Sci. USA*, **102**:16807–16812, 2005.
- [78] H. Kano and H. Hamaguchi. *In vivo* multi-nonlinear optical imaging of a living cell using a supercontinuum light source generated from a photonic crystal fibre. *Opt. Express*, **14**:2798–2804, 2006.
- [79] B. E. A. Saleh and M. C. Teich. *Fundamentals of Photonics*. John Wiley, New York, 1991.
- [80] J. C. Knight and P. S. J. Russell. New ways to guide light. *Science*, **296**:276–277, 2002.

- [81] J. C. Knight. Photonic crystal fibers. *Nature*, **424**:847–851, 2003.
- [82] P. Russell. Photonic crystal fibers. *Science*, **299**:358–362, 2003.
- [83] A. Bjarklev, J. Broeng and A. S. Bjarklev. *Photonic Crystal Fibers*. Kluwer Academic Publishers, Norwell, 2003.
- [84] F. Helmchen, D. W. Tank, W. Denk. Enhanced two-photon excitation through optical fiber by single-mode propagation in a large core. *Appl. Opt.*, **41**:2930–2934, 2002.
- [85] R. Wolleschensky, T. Feurer, R. Sauerbrey, U. Simon. Characterization and optimization of a laser-scanning microscope in the femtosecond regime. *Appl. Phys. B*, **67**:87–94, 1998.
- [86] R. Wolleschensky, M. E. Dickinson, and S. E. Fraser. Group-velocity dispersion and fiber delivery in multiphoton laser scanning microscopy. In *Confocal and Two-photon Microscopy: Foundations, Applications and Advances*, chapter 8, pages 171–190. Wiley-Liss, New York, 2002.
- [87] S. W. Clark, F. O. Ilday, and F. W. Wise. Fiber delivery of femtosecond pulses from a Ti:sapphire laser. *Opt. Lett.*, **26**:1320–1322, 2001.
- [88] D. Bird and M. Gu. Fibre-optic two-photon scanning fluorescence microscopy. *J. Microscopy*, **208**:35–48, 2002.
- [89] D. Bird and M. Gu. Resolution improvement in two-photon fluorescence microscopy with a single-mode fiber. *Appl. Opt.*, **41**:1852–1857, 2002.
- [90] T. Schreiber, T. V. Andersen, D. Schimpf, J. Limpert, and A. Tunnermann. Supercontinuum generation by femtosecond single and dual wavelength pumping in photonic crystal fibers with two zero dispersion wavelengths. *Opt. Express*, **13**:9556–9569, 2005.
- [91] F. Legare, C. L. Evans, F. Ganikhanov, and X. S. Xie. Towards CARS endoscopy. *Opt. Express*, **14**:4427–4432, 2006.

- [92] K. B. Sung, C. Liang, M. Descour, T. Collier, M. Follen, A. Malpica, and R. Richards-Kortum. Near real time *in vivo* fibre optic confocal microscopy: sub-cellular structure resolved. *J. Microscopy*, **207**:137–145, 2002.
- [93] P. M. Lane, A. L. P. Dlugan, R. Richards-Kortum, and C. E. MacAulay. Fibre-optic confocal microscopy using a spatial light modulator. *Opt. Lett.*, **25**:1780–1782, 2000.
- [94] D. Kim, K. H. Kim, S. Yazdanfar and P. T. C. So. Optical biopsy in high-speed handheld miniaturized multifocal multiphoton microscopy. In *Multiphoton Microscopy in the Biomedical Sciences V*, volume **5700**, pages 14–22. Proc. SPIE, 2005.
- [95] A. Jain, A. Kopa, Y. Pan, G. K. Fedder and H. Xie. A two-axis electrothermal micromirror for endoscopic optical coherence tomography. *IEEE J. Quant. Elect.*, **10**:636–642, 2004.
- [96] H. Xie, Y. Pan, and G. K. Fedder. Endoscopic optical coherence tomographic imaging with a CMOS-MEMS micromirror. *Sensors and Actuators*, **103**:237–241, 2003.
- [97] P. Tran, D. Mukai, M. Brenner, and Z. Chen. *In vivo* endoscopic optical coherence tomography by use of a rotational microelectromechanical system probe. *Opt. Lett.*, **29**:1236–1238, 2004.
- [98] P. Herz, Y. Chen, A. Aguirre, K. Schneider, P. Hsiung, J. Fujimoto, K. Madden, J. Schmitt, J. Goodnow, and C. Petersen. Micromotor endoscope catheter for *in vivo*, ultrahigh-resolution optical coherence tomography. *Opt. Lett.*, **29**:2261–2263, 2004.
- [99] D. Aguirre, P. R. Herz, Y. Chen, J. G. Fujimoto, W. Piyawattanametha, L. Fan, S. Hsu, M. Fujino, M. C. Wu, and D. Kopf. Ultrahigh resolution OCT imaging with a two-dimensional mems scanning endoscope. In *Advanced Biomedical and Clinical Diagnostic Systems III*, volume **5692**, pages 277–282. Proc. SPIE, 2005.

- [100] W. Piyawattanametha, R. P. J. Barretto, T. Ko, B. A. Flusberg, E. D. Cocker, H. Ra, D. Lee, O. Solgaard, M. J. Schnitzer. Fast-scanning two-photon fluorescence imaging based on a microelectromechanical systems two-dimensional scanning mirror. *Opt. Lett.*, **31**:2018–2020, 2006.
- [101] H. Choi, S. Chen, D. Kim, P. T. C. So, M. L. Culpepper. Design of a non-linear endomicroscope biopsy probe. In *Biomedical Optics Topical Meeting*. Fort Lauderdale, 2006.
- [102] J. Knittel, L. Schnieder, G. Buess, B. Messerschmidt, T. Possner. Endoscope-compatible confocal microscope using a gradient index-lens system. *Opt. Communication*, **188**:267–273, 2001.
- [103] J. C. Jung, A. D. Mehta, E. Aksay, R. Stepnoski, and M. J. Schnitzer. *In vivo* mammalian brain imaging using one- and two-photon fluorescence microendoscopy. *J. Neurophysiol.*, **92**:3121–3133, 2004.
- [104] K. Sung, C. Liang, M. Descour, T. Collier, M. Follen, and R. Richards-Kortum. Fiber-optic confocal reflectance microscope with miniature objective for *in vivo* imaging of human tissues. *IEEE transactions on Biomedical Engineering*, **49**:1168–1172, 2002.
- [105] W. A. Reed, M. F. Yan, and M. J. Schnitzer. Gradient-index fiber-optic microprobes for minimally invasive *in vivo* low-coherence interferometry. *Opt. Lett.*, **27**:1794–1796, 2002.
- [106] G. Kong, J. Kim, H. Choi, J. E. Im, B. Park, U. Paek, B. H. Lee. Lensed photonic crystal fiber obtained by use of an arc discharge. *Opt. Lett.*, **31**:894–896, 2006.
- [107] W. H. Reeves, D. V. Skryabin, F. Biancalana, J.C. Knight, P. St. J. Russell, F. G. Omenetto, A. Efimov, and A. J. Taylor. Transformation and control of ultrashort pulses in dispersion-engineered photonic crystal fibres. *Nature*, **424**:511–515, 2003.



- [108] J. M. Dudley, L. Provino, N. Grossard, J. Maillotte, R. S. Windeler, B. J. Eggleton, S. Coen. Supercontinuum generation in air-silica microstructured fibers with nanosecond and femtosecond pulse pumping. *J. Opt. Soc. Am. B*, **19**:765–771, 2002.
- [109] W. J. Wadsworth, A. Ortigosa-Blanch, J. C. Knight, T. A. Birks, T. M. Man, and P. S. J. Russell. Supercontinuum generation in photonic crystal fibers and optical fiber tapers: a novel light source. *J. Opt. Soc. Am. B*, **19**:2148–2155, 2002.
- [110] T. Hori, N. Nishizawa, and T. Goto. Experimental and numerical analysis of widely broadened supercontinuum generation in highly nonlinear dispersion-shifted fiber with a femtosecond pulse. *J. Opt. Soc. Am. B*, **21**:1969–1980, 2004.
- [111] D. G. Ouzounov, K. D. Moll, M. A. Foster, W. R. Zipfel, W. W. Webb, and A. L. Gaeta. Delivery of nanojoule femtosecond pulses through large-core microstructured fibers. *Opt. Lett.*, **27**:1513–1515, 2002.
- [112] G. Humbert, J. C. Knight, G. Bouwmans, P. S. J. Russell, D. P. Williams, P. J. Roberts, and B. J. Mangan. Hollow core photonic crystal fibers for beam delivery. *Opt. Express*, **12**:1477–1484, 2004.
- [113] W. Göbel, A. Nimmerjahn, and F. Helmchen. Distortion-free delivery of nanojoule femtosecond pulses from a Ti:sapphire laser through a hollow-core photonic crystal fiber. *Opt. Lett.*, **29**:1285–1287, 2004.
- [114] S. P. Tai, M. C. Chan, T. H. Tsai, S. H. Guol, L. J. Chen, and C. K. Sun. Two-photon fluorescence microscope with a hollow-core photonic crystal fiber. *Opt. Express*, **12**:6122–6128, 2004.
- [115] B. A. Flusberg, J. C. Jung, E. D. Cocker, E. P. Anderson, and M. J. Schnitzer. *In vivo* brain imaging using a portable 3.9 gram two-photon fluorescence microendoscope. *Opt. Lett.*, **30**:2272–2274, 2005.

- [116] D. Yelin, B. E. Bouma, S. H. Yun, and G. J. Tearney. Double-clad fiber for endoscopy. *Opt. Lett.*, **29**:2408–2410, 2004.
- [117] J. Limpert, T. Schreiber, S. Nolte, H. Zellmer, A. Tunnermann, R. Iliew, F. Lederer, J. Broeng, G. Vienne, A. Petersson, and C. Jakobsen. High-power air-clad large-mode-area photonic crystal fiber laser. *Opt. Express*, **11**:818–823, 2003.
- [118] J. Limpert, A. Liem, M. Reich, T. Schreiber, S. Nolte, H. Zellmer, A. Tunnermann, J. Broeng, A. Petersson, and C. Jakobsen. Low-nonlinearity single-transverse-mode ytterbium-doped photonic crystal fiber amplifier. *Opt. Express*, **12**:1313–1319, 2004.
- [119] M. T. Myaing, J. Y. Ye, T. B. Norris, T. Thomas, J. R. Baker, W. J. Wadsworth, G. Bouwmans, J. C. Knight, and P. St. J. Russell. Enhanced two-photon biosensing with double-clad photonic crystal fibers. *Opt. Lett.*, **28**:1224–1226, 2003.
- [120] J. Y. Ye, M. T. Myaing, T. P. Thomas, I. Majoros, A. Koltzhar, J. R. Baker, W. J. Wadsworth, G. Bouwmans, J. C. Knight, P. St. J. Russell, and T. B. Norris. Development of a double-clad photonic crystal fiber based scanning microscope. In *Multiphoton Microscopy in the Biomedical Sciences V*, volume **5700**, pages 23–27. Proc. SPIE, 2005.
- [121] L. Fu, X. Gan, and M. Gu. Nonlinear optical microscopy based on double-clad photonic crystal fibers. *Opt. Express*, **13**:5528–5534, 2005.
- [122] N. Nishizawa, Y. Chen, P. Hsiung, E. P. Ippen, and J. G. Fujimoto. Real-time, ultrahigh-resolution, optical coherence tomography with an all-fiber, femtosecond fiber laser continuum at 1.5  $\mu\text{m}$ . *Opt. Lett.*, **29**:2846–2848, 2004.
- [123] K. Shi, P. Li, S. Yin, and Z. Liu. Chromatic confocal microscopy using supercontinuum light. *Opt. Express*, **12**:2096–2101, 2004.

- [124] G. McConnell and E. Riis. Two-photon laser scanning fluorescence microscopy using photonic crystal fibre. *J. Biomed. Opt.*, **9**:922–927, 2004.
- [125] G. McConnell and E. Riis. Photonic crystal fibre enables short-wavelength two-photon laser scanning fluorescence microscopy with fura-2. *Phys. Med. Biol.*, **49**:4757–4763, 2004.
- [126] J. A. Palero, V. O. Boer, J. C. Vijvergerg, H. C. Gerritsen, and H. J. C. M. Sterenborg. Short-wavelength two-photon excitation fluorescence microscopy of tryptophan with a photonic crystal fiber based light source. *Opt. Express*, **13**:5363–5368, 2005.
- [127] K. Isobe, W. Watanabe, S. Matsunaga, T. Higashi, K. Fukui, and K. Itoh. Multi-spectral two-photon excited fluorescence microscopy using supercontinuum light source. *Jpn. J. Appl. Phys.*, **44**:L167–L169, 2005.
- [128] M. J. Levene, D. A. Dombeck, K. A. Kasischke, R. P. Molloy, and W. W. Webb. *In vivo* multiphoton microscopy of deep brain tissue. *J. Neurophysiol.*, **91**:1908–1912, 2004.
- [129] L. Fu, X. Gan, and M. Gu. Use of a single-mode fiber coupler for second-harmonic-generation microscopy. *Opt. Lett.*, **30**:385–387, 2005.
- [130] L. Fu and M. Gu. A double-clad photonic crystal fiber coupler for compact nonlinear optical microscopy imaging. *Opt. Lett.*, **31**:1471–1473, 2006.
- [131] Y. Namihira. Polarisation beam-splitting and combining characteristics of fused taper single-mode fibre couplers. *Electron. Lett.*, **22**:715–716, 1986.
- [132] L. Fu, X. Gan, D. Bird, and M. Gu. Polarisation characteristics of a  $1 \times 2$  fiber coupler under femtosecond pulsed and continuous wave illumination. *Optics and Laser Technology*, **37**:494–497, 2005.
- [133] M. Born and E. Wolf. *Principles of Optics*. Pergamon, New York, 1980.

- [134] D. Bird and M. Gu. Compensation for depolarisation by a fibre coil in the presence of self-phase modulation. *Optics and Laser Technology*, **35**:381–383, 2003.
- [135] L. Fu, X. Gan, and M. Gu. Characterization of the GRIN lens-fiber spacing toward applications in two-photon fluorescence endoscopy. *Appl. Opt.*, **44**:7270–7274, 2005.
- [136] M. Gu. *Principles of Three-Dimensional Imaging in Confocal Microscopes*. World Scientific, Singapore, 1996.
- [137] C. Xu and W. W. Webb. Measurement of two-photon excitation of cross sections of molecular fluorophores with data from 690 to 1050 nm. *J. Opt. Soc. Am. B*, **13**:481–491, 1996.
- [138] M. Gu and C. J. R. Sheppard. Signal level of the fiber-optical confocal scanning microscope. *J. Mod. Opt.*, **38**:1621–1630, 1991.
- [139] C. J. R. Sheppard and M. Gu. The significance of 3D transfer functions in confocal scanning microscopy. *J. Microscopy*, **164**:377–390, 1991.
- [140] M. Gu, C. J. R. Sheppard, and X. Gan. Image formation in a fiber-optical confocal scanning microscope. *J. Opt. Soc. Am. A*, **8**:1755–1761, 1991.
- [141] M. Gu and D. Bird. Three-dimensional optical-transfer-function analysis of fiber-optical two-photon fluorescence microscopy. *J. Opt. Soc. Am. A*, **20**:941–947, 2003.
- [142] M. Gu and C. J. R. Sheppard. Comparison of three-dimensional imaging properties between two-photon and single-photon fluorescence microscopy. *J. Microscopy*, **177**:128–137, 1995.
- [143] M. Gu, X. Gan, and C. J. R. Sheppard. Three-dimensional coherent transfer functions in fiber-optical confocal scanning microscopes. *J. Opt. Soc. Am. A*, **8**:1019–1025, 1991.

- [144] M. Gu and L. Fu. Three-dimensional image formation in fiber-optical second harmonic generation microscopy. *Opt. Express*, **14**:1175–1181, 2006.
- [145] S. Yazdanfar, L. H. Laiho, and P. T. C. So. Interferometric second harmonic generation microscopy. *Opt. Express*, **12**:2739–2745, 2004.
- [146] H. Xie, A. Jain, T. Xie, Y. Pan, and G. K. Fedder. A single-crystal silicon-based micromirror with large scanning angle for biomedical applications. In *Conference on Lasers and Electro Optics 2003*. Baltimore, 2003.
- [147] A. Jain and H. Xie. An electrothermal SCS micromirror for large bi-directional 2D scanning. In *13<sup>th</sup> International Conference on Solid-state Sensor, Actuators and Microsystems*, pages 988–991. Korea, 2005.
- [148] R. S. Dacosta, B. C. Wilson, and N. E. Marcon. New optical technologies for earlier endoscopic diagnosis of premalignant gastrointestinal lesions. *Journal of Gastroenterology and Hepatology*, **17**:S85–S104, 2002.
- [149] H. M. Chen, C. Y. Wang, C. T. Chen, H. Yang, Y. S. Kuo, W. H. Lan, M. Y. Kuo, and C. P. Chiang. Auto-fluorescence spectra of oral submucous fibrosis. *J. Oral Pathol. Med.*, **32**:337–343, 2003.
- [150] J. R. Salgueiro and Y. S. Kivshar. Nonlinear dual-core photonic crystal fiber couplers. *Opt. Lett.*, **30**:1858–1860, 2005.
- [151] B. H. Lee, J. B. Eom, J. Kim, D. S. Moon, U. Paek, and G. Yang. Photonic crystal fiber coupler. *Opt. Lett.*, **27**:812–814, 2002.
- [152] H. Kim, J. Kim, U. Paek, B. Lee, and K. T. Kim. Tunable photonic crystal fiber coupler based on a side-polishing technique. *Opt. Lett.*, **29**:1194–1196, 2004.
- [153] Y. Kim, Y. Jeong, K. Oh, J. Kobelke, K. Schuster, and J. Kirchhof. Multiport  $n \times n$  multimode air-clad holey fiber coupler for high-power combiner and splitter. *Opt. Lett.*, **30**:2697–2699, 2005.

- [154] J. J. Larsen and G. Vienne. Side pumping of double-clad photonic crystal fibers. *Opt. Lett.*, **29**:436–438, 2004.

# Publications of the Author

## Journal Publications

Ling Fu, Xiaosong Gan, and Min Gu. Use of a single-mode fiber coupler for second-harmonic-generation microscopy. *Opt. Lett.*, **30**:385–387, 2005.

Ling Fu, Xiaosong Gan, Damian Bird, and Min Gu. Polarisation characteristics of a  $1 \times 2$  fiber coupler under femtosecond pulsed and continuous wave illumination. *Optics and Laser Technology*, **37**:494–497, 2005.

Ling Fu, Xiaosong Gan, and Min Gu. Nonlinear optical microscopy based on double-clad photonic crystal fibers. *Opt. Express*, **13**:5528–5534, 2005.

Ling Fu, Xiaosong Gan, and Min Gu. Characterization of the GRIN lens-fiber spacing toward applications in two-photon fluorescence endoscopy. *Appl. Opt.*, **44**:7270–7274, 2005.

Ling Fu, Ankur Jain, Huikai Xie, Charles Cranfield, and Min Gu. Nonlinear optical endoscopy based on a double-clad photonic crystal fiber and a MEMS mirror. *Opt. Express*, **14**:1027–1032, 2006.

Min Gu and Ling Fu. Three-dimensional image formation in fiber-optical second-harmonic-generation microscopy. *Opt. Express*, **14**:1175–1181, 2006.

Ling Fu and Min Gu. A double-clad photonic crystal fiber coupler for compact

nonlinear optical microscopy imaging. *Opt. Lett.*, **31**:1471–1473, 2006.

Ling Fu and Min Gu. Fibre-optic nonlinear optical endoscopy (under preparation).

Ling Fu, Ankur Jain, Huikai Xie, Charles Cranfield, and Min Gu. Three-dimensional nonlinear optical endoscopy for normal and malignant tissue imaging (under preparation).

## Conferences

Ling Fu, Xiaosong Gan, and Min Gu. Second harmonic generation microscopy based on a single-mode fiber coupler. *Australian Conference on Optics, Lasers and Spectroscopy*, Melbourne, Australia, December 1 – 4, 2003.

Ling Fu, Xiaosong Gan, and Min Gu. Use of a single-mode fiber coupler for second harmonic generation microscopy. *Focus on Microscopy 2004*, Philadelphia, USA, April 4 – 7, 2004.

Ling Fu, Xiaosong Gan, and Min Gu. A fiber-optic second harmonic generation microscope. *17th Australian Optical Society Conference*, Canberra, Australia, July 5 – 8, 2004.

Ling Fu, Xiaosong Gan, and Min Gu. Characterization of fiber-optic second harmonic generation microscopy. *8th International Conference on Optics within Life Sciences*, Melbourne, Australia, November 28 – December 1, 2004.

Min Gu, Ling Fu, and Xiaosong Gan. A nonlinear optical microscopy using double-clad photonic crystal fibers. *Focus on Microscopy 2005*, Jena, Germany, March 20 – 23, 2005.

Min Gu, Ling Fu, and Xiaosong Gan. Nonlinear optical microscopy based on double-clad photonic crystal fibers. *17th International Conference on Photonics in Europe*, Munich, Germany, June 12 – 17, 2005.



Ling Fu, Ankur Jain, Huikai Xie, Charles Cranfield, and Min Gu. Integration of a double-clad photonic crystal fiber, a GRIN lens and a MEMS mirror for nonlinear optical endoscopy. *Biomedical Topical Meeting of Optical Society of America*, Fort Lauderdale, USA, March 19 – 22, 2006.

Ling Fu and Min Gu. Use of a double-clad photonic crystal fibre coupler for compact nonlinear optical microscopy. *Focus on Microscopy 2006*, Perth, Australia, April 9 – 12, 2006.

Min Gu and Ling Fu. Nonlinear optical endoscopy: Coming of age. *World Congress on Medical Physics and Biomedical Engineering 2006*, Seoul, Korea, August 28 – September 1, 2006.

Min Gu and Ling Fu. Fibre-optic nonlinear optical endoscopy: Coming of age. *5th International Conference on Optics-photonics Design and Fabrication*, Nara, Japan, December 6 – 8, 2006.